SANDIA REPORT
SAND2024-07526
Printed June 2024

PE1 Site Characterization: Data Documentation on Geologic and Hydrologic Lab Testing

Jennifer E. Wilson[1], Jason E. Heath[1], Kristopher L. Kuhlman[1], Guangping Xu[1], Miles A. Bodmer[1], Scott T. Broome[1], Johnny Jaramillo[1], Perry Barrow[1], Mark A. Rodriguez[1], James J.M. Griego[1], Nichole R. Valdez[1], Justin Reppart[2], Devon Smith[2], Jennifer Larotonda[2], Margaret Townsend[2].

[1]Sandia National Laboratories, Albuquerque, New Mexico
[2]Mission Support and Test Services, LLC Nevada National Security Sites, Nevada

Prepared by
Sandia National Laboratories
Albuquerque, New Mexico
87185 and Livermore,
California 94550

Issued by Sandia National Laboratories, operated for the United States Department of Energy by National Technology & Engineering Solutions of Sandia, LLC.

Available to DOE and DOE contractors from
U.S. Department of Energy
Office of Scientific and Technical Information
P.O. Box 62
Oak Ridge, TN 37831

Telephone: (865) 576-8401
Facsimile: (865) 576-5728
E-Mail: reports@osti.gov
Online ordering: http://www.osti.gov/scitech

Available to the public from
U.S. Department of Commerce
National Technical Information Service
5301 Shawnee Rd
Alexandria, VA 22312

Telephone: (800) 553-6847
Facsimile: (703) 605-6900
E-Mail: orders@ntis.gov
Online order: https://classic.ntis.gov/help/order-methods/

ABSTRACT

This data documentation report describes geologic and hydrologic laboratory analysis and data collected in support of site characterization of the Physical Experiment 1 (PE1) testbed, Aqueduct Mesa, Nevada. The documentation includes a summary of laboratory tests performed, discussion of sample selection for assessing heterogeneity of various testbed properties, methods, and results per data type.

ACKNOWLEDGEMENTS

This Low Yield Nuclear Monitoring (LYNM) research was funded by the National Nuclear Security Administration, Defense Nuclear Nonproliferation Research and Development (NNSA DNN R&D). The authors acknowledge important interdisciplinary collaboration with scientists and engineers from LANL, LLNL, NNSS, PNNL, and SNL.

Sandia National Laboratories is a multimission laboratory managed and operated by National Technology & Engineering Solutions of Sandia, LLC, a wholly owned subsidiary of Honeywell International Inc., for the U.S. Department of Energy's National Nuclear Security Administration under contract DE-NA0003525.

CONTENTS

LIST OF FIGURES

LIST OF TABLES

This page left blank

ACRONYMS AND TERMS

Acronym/Term	Definition
BSE	back-scattered electrons
CT	computed tomography
DI	deionized water
EDS	energy dispersive spectra
MSA	multivariate statistical analysis
MICP	mercury intrusion capillary pressure
NNSS	Nevada National Security Site
PCA	principal component analysis
PE1	Physical Experiment 1
SNL	Sandia National Laboratories
VNT	vitric nonwelded tuff
UZNT	upper zeolitic nonwelded tuff
XRD	X-ray diffraction
XRF	X-ray fluorescence

This page left blank

1. INTRODUCTION

This data documentation report describes geologic and hydrologic laboratory analysis and data collected in support of site characterization of the Physical Experiment 1 (PE1) testbed, which is located at Aqueduct Mesa within the Nevada National Security Site (NNSS; Figure 1). PE1 is a series of multi-physics experiments consisting of several planned underground chemical explosions and monitoring by a suite of subsurface and surface instruments (Myers et al., 2024). The information provided herein is meant to facilitate detailed interpretation of data in companion scientific studies (Bodmer et al., 2024; Kibikas et al.; Wilson et al., 2024).

The geologic and hydrologic data documentation includes the following:

- a master list of laboratory tests and data products;
- discussion of sample selection for assessing heterogeneity of PE1 testbed properties; and
- methods; and
- summary of results.

Data types for geology are to support identification of lithologies, secondary mineral alteration, and their variability both within and among the various geologic units of the PE1 testbed. Lithology and secondary mineral alteration are major controls on pore structure and hence physical properties of the geologic units, including hydrologic and geomechanical properties.

Data types for hydrology characterize in situ water content from samples preserved in the field against dry-out and fluid flow properties to support numerical modeling of multiphase fluid flow and gas transport of the PE1 testbed.

Rock samples for the various hydrologic and geologic laboratory testing were typically collected in groups at the same locations. Such correlative sampling generates data sets that can be used together in companion scientific studies to interpret geologic, hydrologic, and geomechanical properties and characterize coupled processes.

This page left blank

2. SUMMARY OF LABORATORY ANALYSIS AND DATA PRODCUTS

PE1 site characterization includes a variety of laboratory testing that fits within the larger PE1 experimental plan and modeling efforts (Myers et al., 2024; Bodmer et al., 2024). Table 1 presents the master list and high-level details of the variety of geologic and hydrologic laboratory testing on PE1 rock samples and the associated data products, which are represented in tables and figures in the remainder of this report.

As the PE1 testbed is located near a geologic transition zone between vitric and zeolitic units, the rock composition and pore structure can vary greatly within and between sub-geologic units, which may affect fluid flow, tracer transport, and geomechanics. Thus, laboratory geologic testing focuses on petrography with spatial mapping of composition, X-ray diffraction, and X-ray computed tomography (CT). Samples were selected to characterize mapped geologic units at the PE1 testbed (Figure 1). These data support understanding of geologic controls on heterogeneity and to potentially support calibration of petrophysical logging as needed.

Hydrologic laboratory testing focuses on the following: multiphase fluid flow properties and further understanding of pore size distribution via mercury intrusion capillary pressure (MICP) measurements; water content as based on "hand" samples preserved in the field during mining operations, with supplemental thermogravimetric analysis (TGA); and porosity, permeability, bulk density, and grain density. The MICP data enable assessment of capillary heterogeneity for the various sampled geologic units, and the MICP data are used in this report to predict absolute and relative permeability. Water content is measured on preserved samples to characterize in situ conditions that inform geophysical framework modeling and geomechanical testing on core samples that correspond to the hand samples. Gravimetric and volumetric water content measurements include heating to 60°C, which may measure water that is available for flow, whereas thermogravimetric analysis (TGA) is used to inform on sorbed and structural water of solid phases.

Petrographic data includes photomicrographs and geologic descriptions via optical petrography, including 300-point counting per thin section for all phases, 100-point counting per thin section for pore types, as well as scanning electron microscopy (SEM) with energy dispersive spectroscopy (EDS) on 18 thin sections. Spatial X-ray fluorescence has been performed on a subset of the petrographic thin sections. Gravimetric water content (namely mass wetness) has been measured on nine preserved grab/hand samples and three preserved core segments. Volumetric measurements via three-dimensional (3D) scanning are taken on all 12 samples to convert mass wetness to volume wetness but note that one of these samples was also scanned via X-ray CT and used to estimate the sample's volume to yield volume wetness as quality control check. The 12 preserved samples were subsequently sub-cored for measurements of porosity, permeability, dry bulk density, and grain density. Porosity and volume were used to estimated water saturation.

Table 1. Summary list of PE1 Site Characterization geologic and hydrologic laboratory testing and analyses.

Category	Laboratory test or analysis	Data products	Sample Quantity
Geologic	Petrography	Composition and porosity via point counts in Table 4, based on optical petrography; thin section inventory images (Figure 5); representative photomicrographs at different scales with petrographic observations (Figures 6–23); scanning electron microcopy-energy dispersive spectroscopy (SEM-EDS) photomicrographs, maps, and petrographic descriptions for high resolution data (Figures 24–30)	18
	X-ray diffraction (XRD)	Mineral quantification in Tables 5 and 6, including bulk and fine fractions, precent amorphous phase(s), and percent expandability	18
	Spatial X-ray fluorescence (XRF)	Scored spatial XRF maps for polished thin sections or billets, based on principal component analysis (PCA), with representative spectra per scored phase; data as images summarized in power point files (Figures 31–35); data files for additional post-processing on X-ray spectral images PCA images	6
	X-ray computed tomography	Image stacks for scans on entire billets used in XRF at 21 or 23-μm voxel resolution, with higher resolution sub-volume scans at 5.8 or 5.9-μm resolution (Figures 36–39)	2
Hydrologic	Mercury intrusion capillary pressure (MICP)	MICP summary (Tables 7 and 8) and multi-worksheet spreadsheets per sample with raw and transformed data, including conformance-closure corrections, conversion to the air-water system, calculation of saturation, Swanson permeability, porosity, bulk density, grain density, and extrusion data; plots of pore size and capillary pressure (Figures 40–49); a photograph of the given sample (Table 7); image results of curve fitting (Figures 50–57)	8
	Thermogravimetric analysis (TGA)	Summary of mass change versus temperature (Table 9); raw data text files and plots of temperature vs residual weight (Figures 58–59)	19
	In situ water content	Mass wetness based on sample weight before and after for preserved "hand" samples (Table 10); sample volume for volumetric water content (Figures 60–61)	12
	Porosity, perm., bulk and grain density	Helium pycnometry porosity and air permeability measurements made on sub-cores of grab samples; dry bulk density and grain density (Table 11)	12

3. SAMPLE SELECTION, METHODS, AND RESULTS PER DATA TYPE

3.1. Sample Selection

Laboratory geologic analysis discussed herein characterizes ten mapped Vitric Nonwelded Tuff (VNT) subunits and the Upper Zeolitic Nonwelded Tuff (UZNT) lithology (Figure 1). Hydrologic laboratory testing characterizes a subset of the lithofacies of the 10 units. VNT generally means vitric non-welded tuff, but at the PE1 testbed, these samples can include samples from a transition zone where variation in the water table resulted in corresponding variance in the degree of diagenetic alteration, mineral/glass dissolution, and precipitation of secondary minerals and mineraloid or amorphous phases. UZNT corresponds to zeolitized units. The guiding principle for geologic laboratory analysis is to collect samples for measuring and assessing the heterogeneity of the PE1 testbed geologic properties. Multiple samples have been collected from within the UZNT and a given VNT subunit as well as among units to help characterize inter- and intra-sub-unit heterogeneity.

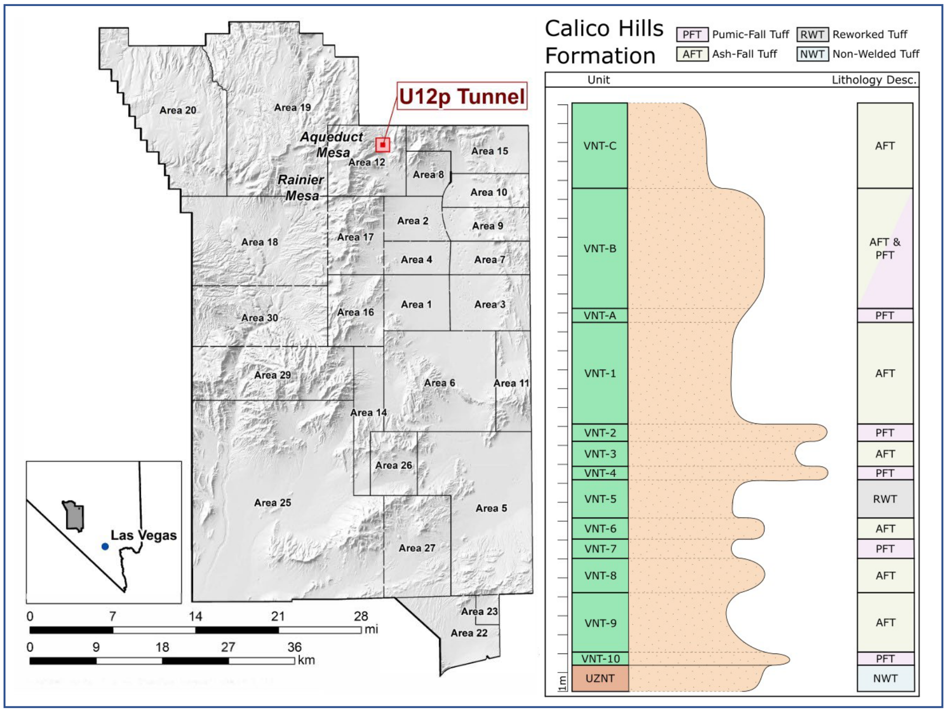

Figure 1. (left) Map of the NNSS with red box covering Aqueduct Mesa, U12p Tunnel (a.k.a., P-Tunnel). (right) Stratigraphic column of Aqueduct Mesa in the vicinity of the PE1 testbed.

Sample IDs reported herein correspond to coreholes or drifts that uniquely locate them. For coreholes, this includes the corehole identifier (GI-2, GI-3, GI-4, DA-1, AC-1) and the drilling depth (Table 2). The majority of samples come from subhorizontal coreholes GI-4, GI-3, and GI-2, which were drilled prior to drift excavation. Photographs and cross sections from drifts 1190, 1280, and 1490—which correspond, respectively to coreholes GI-4, GI-3, and GI-2—are provided here as a general reference (see Figure 2, Figure 3, and Figure 4). For drifts, this includes the drift identifier (1190, 1280, and 1490) and the Northing, Easting, and elevation values.

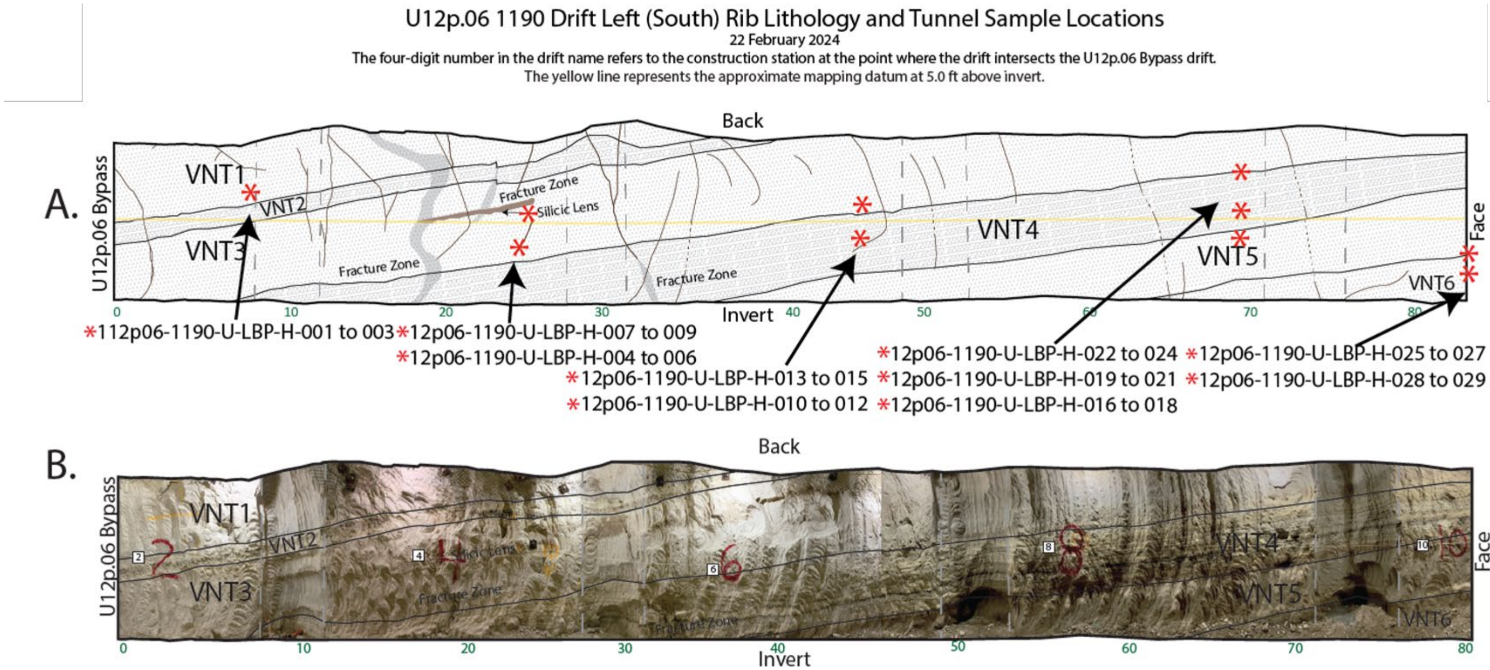

U12p.06 1190 Drift Left (South) Rib Lithology and Tunnel Sample Locations

22 February 2024

The four-digit number in the drift name refers to the construction station at the point where the drift intersects the U12p.06 Bypass drift.

The yellow line represents the approximate mapping datum at 5.0 ft above invert.

Figure 2. A. Digitized rib map showing model sublayers along drift U12p.06 1190. Keyway locations are indicated by vertical gray dashed lines. Nominally horizontal yellow line is the geologists' mapping reference. No vertical exaggeration. B. Digitized rib map showing model sublayers overlaid on a photo mosaic. This flattened view results in some distortion, giving unrealistic bedding dips (particularly around keyway locations and near the face) and subtle bedding offsets. Distance from U12p.06 bypass drift indicated n green (feet), which roughly correspond to sample locations in this report for the corehole GI-4 (the corehole was generally down the center of the drift).

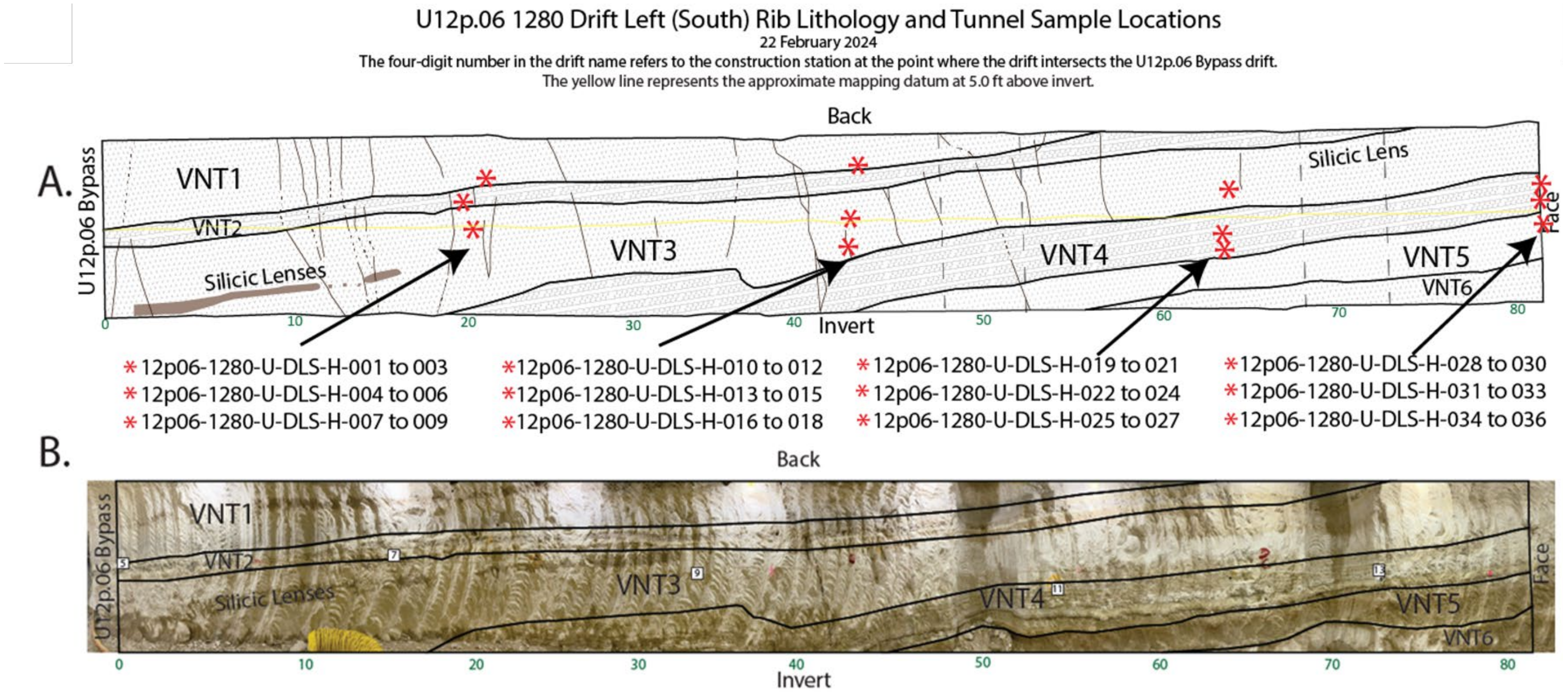

Figure 3. A. Digitized rib map showing model sublayers along drift U12p.06 1280. Keyway locations are indicated by vertical gray dashed lines. Nominally horizontal yellow line is the geologists' mapping reference. No vertical exaggeration. B. Digitized rib map showing model sublayers overlaid on a photo mosaic. This flattened view results in some distortion, giving unrealistic bedding dips (particularly around keyway locations and near the face) and subtle bedding offsets. Distance from U12p.06 bypass drift indicated n green (feet), which roughly correspond to sample locations in this report for the corehole GI-4 (the corehole was generally down the center of the drift).

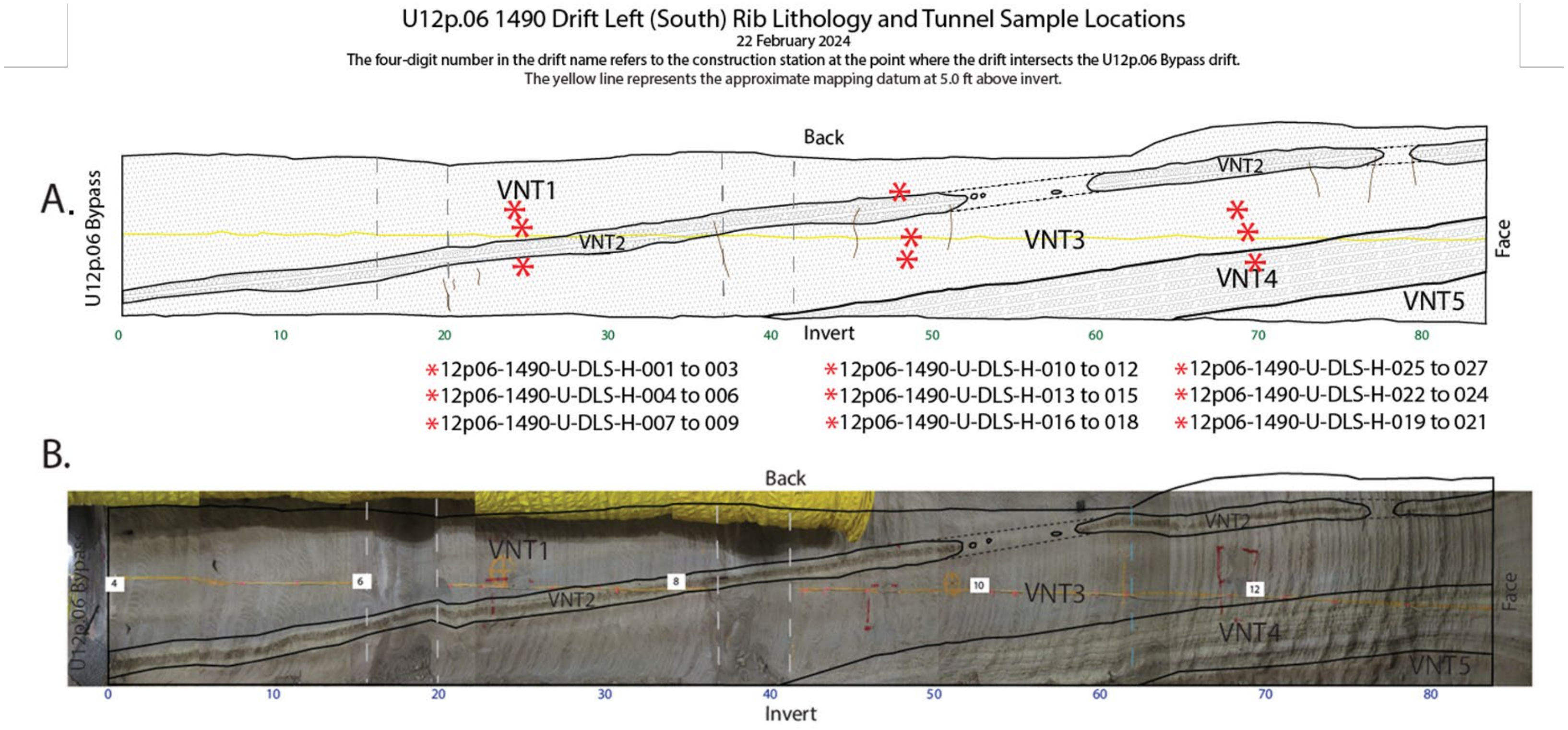

Figure 4. A. Digitized rib map showing model sublayers along drift U12p.06 1490. Keyway locations are indicated by vertical gray dashed lines. Nominally horizontal yellow line is the geologists' mapping reference. No vertical exaggeration. B. Digitized rib map showing model sublayers overlaid on a photo mosaic. This flattened view results in some distortion, giving unrealistic bedding dips (particularly around keyway locations and near the face) and subtle bedding offsets. Distance from U12p.06 bypass drift indicated n green (feet), which roughly correspond to sample locations in this report for the corehole GI-4 (the corehole was generally down the center of the drift).

Table 2 gives a master test matrix with the following: geologic and hydrologic testing types; sample locations along the given corehole to a tenth of a ft and/or via coordinates in Northing, Easting, and elevation values (SP NAD27) for grab samples; the naming nomenclature in this report; and the lithologic unit from which the sample was taken. For this report, each of the ten mapped VNT subunits and UZNT lithology were subsampled at least once and up to three times, and these subsamples were used for thin section petrography, XRF, and XRD. Sample selection was based on VNT subunit divisions and textural descriptions within a subunit to ensure selected samples capture heterogeneity within and among each subunit.

Table 2. Test matrix with geologic unit, sample ID, and testing types denoted by specific locations for samples, namely drilling depth to a tenth of a foot for core and SP NAD27 coordinates and elevation for grab samples.

Lith. Unit	Sample ID	Petrography	Spatial XRF	X-ray CT	XRD	TGA	MICP	Water Content	Porosity, permeability, grain- & bulk- density
		Specific location for sample by drilling depth (ft), which may apply to multiple testing types; blank and gray means no sampling for the specific test in the given column						SP NAD 27 coordinates for sample location	
VNT-1	GI-2-6	6.4			6.4				
VNT-2	GI-3-2	2.3			2.3				
	GI-4-8	8.3			8.3				
VNT-3	GI-4-18	18.4			18.4		18.5		
	GI-4-35	35.1			35.1		35.3		
	PE1-U12p06-1280-13							N905939.5, E647958.0, 5521.8 ft elevation	
	PE1-U12p06-1190-4							N905814.6, E647948.2, 5520.6 ft elevation	
	PE1-U12p06-1190-13							N905814.8, E647926.6, 5522.6 elevation	
VNT-4	GI-4-44	44.5					44.5		
	GI-4-54	54.2			54.1		54.5		
	GI-4-49	49.5			49.5				
	GI-3-51	51.2			51.2				
	PE1-U12p06-1490-25							N906133.6, E647972.0, 5520.0 ft elevation	
	PE1-U12p06-1280-22							N905950.3, E647942.4, 5521.2 ft elevation	
	PE1-U12p06-1280-31							N905962.2, E647929.2, 5522.4 ft elevation	

Lith. Unit	Sample ID	Petrography	Spatial XRF	X-ray CT	XRD	TGA	MICP	Water Content	Porosity, permeability, grain- & bulk- density
		Specific location for sample by drilling depth (ft), which may apply to multiple testing types; blank and gray means no sampling for the specific test in the given column						SP NAD 27 coordinates for sample location	
VNT-5	GI-2-65	65.6			65.6				
	GI-4-72	73.2					73.3		
	PE1-U12p06-1280-34							N905962.3, E647928.8, 5521.1 ft elevation	
	PE1-U12p06-1190-16							N905814.6, E647905.4, 5519.4 elevation	
	PE1-U12p06-1190-25							N905814.7, E647891.5, 5518.2 ft elevation	
VNT-6	DA-1-17	17.2			17.2		17.1		
VNT-7	DA-1-19	19.3			19.2				
VNT-8	DA-1-25	25.6			25.7				
VNT-9	DA-1-35	35.7			35.8				
VNT-10	DA-1-36	36.7			36.8		36.7		
UZNT	AC-1-65	65.8			65.9				
	AC-1-71	71.7			71.8				
	AC-1-111	111.4			111.5		111.4		
	PE1-U12p06-AC-1-92.5-92.9							92.7	
	PE1-U12p06-AC-1-120.3-120.8							120.4	
	PE1-U12p06-AC-1-151.5-152.0							151.6	

3.2. Geologic Laboratory Data

3.2.1. Petrography

Rock samples for preparation of epoxied polished thin sections and billets were obtained by trimming selected samples from core with a Buehler IsoMet 1000 Precision Saw using deionized water (DI) water as lubricant. The trimmed rock samples were shipped to Wagner Petrographics for standard petrographic thin sections at 27 mm × 46 mm area and 30 µm thickness, with corresponding polished billets for each thin section. The rock samples were impregnated with low viscosity fluorescent red-dye epoxy resin under high vacuum to accentuate pores. The polished epoxied billets have approximately the same area of the standard thin sections, but are thicker (e.g., approximately 10 mm) to allow for study of three-dimensional pore structure (e.g., via X-ray CT or laser scanning confocal microscopy on the fluorescent epoxy) that is closely linked with two-dimensional (2D) analysis on the top surface of the polished billet (e.g., via SEM-EDS or spatial XRF). Optical petrography on all thin sections was performed with a Zeiss LSM 900 using plane polarized and cross-polarized transmitted light as well as reflected light. At least two plane polarized transmitted light images at low (50×) and high (200×) total magnification were taken for each thin section, and a photomosaic of each thin section was obtained at 50× total magnification using the Zen Imaging System for the Zeiss LSM 900.

Petrographic observation and quantitative analysis includes the following: texture, e.g., using grain-size and sorting comparators; a 300-point count for abundances of framework grains, non-framework components, and total porosity; types and abundances of framework and non-framework components; porosity types, including a 100-point count specifically on pore types (e.g., if visible, intergranular, intragranular, etc.); diagenesis, including diagenetic history, secondary minerals, mechanical diagenesis and degree of compaction, authigenic minerals, and porosity and mineral textures (e.g., pore-filling, replacement, dissolution, etc.).

Scanning electron microscopy with elemental mapping by energy or wavelength dispersive spectroscopy was performed for all of the thin sections to support the petrographic observations and interpretations with higher resolution observations. Table 3 summarizes the MSTS field mapping unit, which vary from ash- and pumice-fall tuffs—which may be reworked and with silicic zones—to zeolite-rich tuffs. Thin sections and billets were prepared from all of these units (Figure 5 and Table 4). The geologic unit variability for framework (i.e., pumice, phenocrysts), matrix, and porosity types varies greatly among the 10 VNT units and the UZNT (Table 4), and the distribution or arrangement of these phases, including what solid phases line pores and will be exposed to directly to fluids, also varies greatly as shown in the petrographic images (Figure 6 through Figure 23). Note that thin section sample preparation may potentially have altered the morphology of water-sensitive phases (e.g., opal, zeolite, and swelling clays). Imaging of preserved samples via environmental SEM in humid environments with a cryo focused ion beam –scanning electron microscopy could be used to further characterization potentially representative morphology of water-sensitive pore-lining phases.

Table 3. Geologic unit naming and descriptions.

Former Unit Names	Lithologic Unit Name of PE1 Field Mapping	Description
MC-4	VNT-1	Ash-fall tuff, mostly vitric
	VNT-2	Pumice-fall tuff, vitric with zeolite and silica at base
	VNT-3	Ash-fall tuff, vitric with silicic zones
	VNT-4	Pumice-fall tuff, vitric to zeolitic with silicic zones
	VNT-5	Ash-fall/reworked tuff, vitric to zeolitic
	VNT-6	Ash-fall tuff, vitric to zeolitic
	VNT-7	Pumice-fall tuff, mostly zeolitic
	VNT-8	Ash-fall tuff, mostly vitric with zeolitic zones
	VNT-9	Ash-fall tuff, mostly vitric with zeolitic zones
	VNT-10	Pumice-fall tuff, mostly vitric with zeolitic zones
MC-3	UZNT	Zeolitic tuff

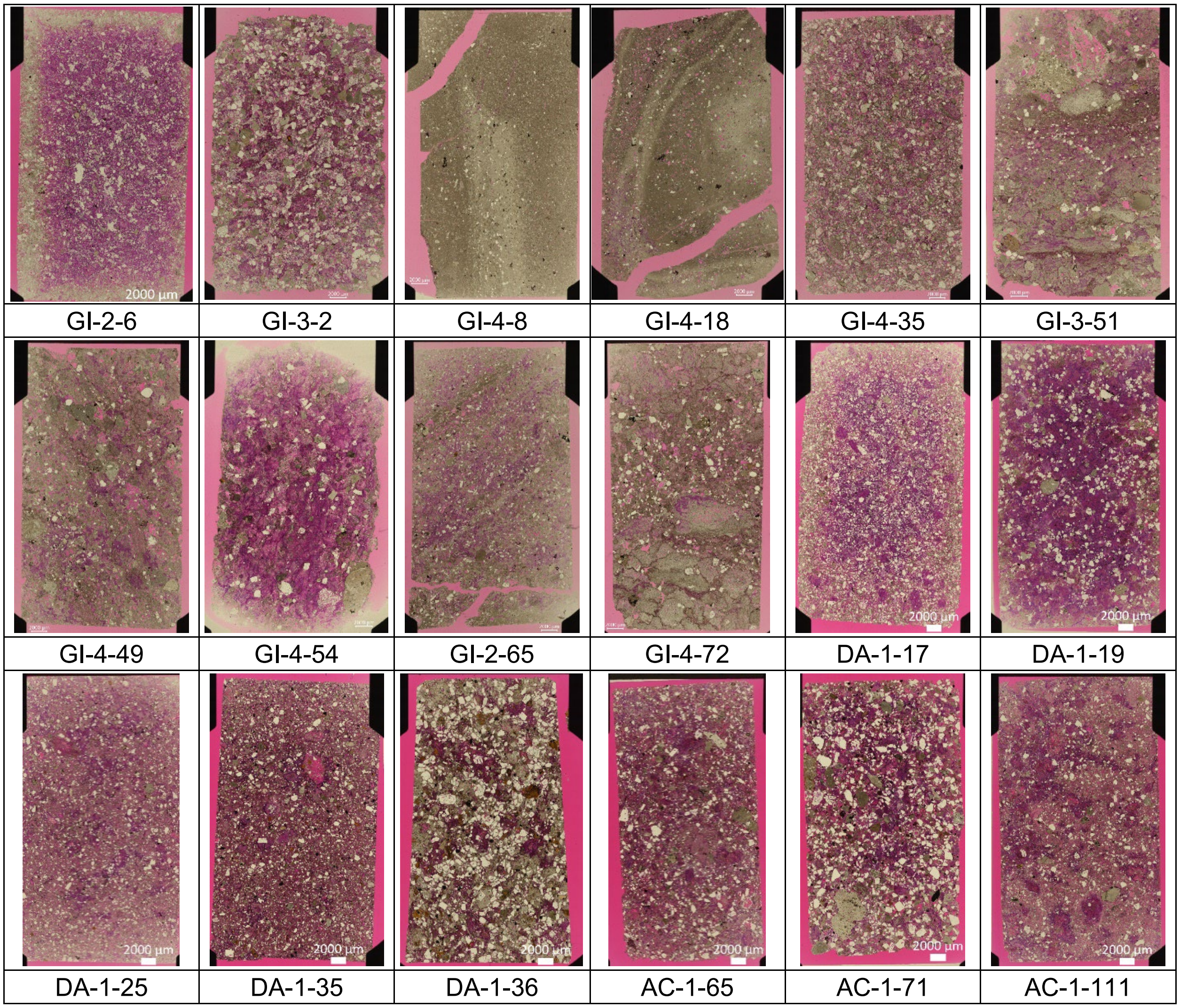

GI-2-6
GI-3-2
GI-4-8
GI-4-18
GI-4-35
GI-3-51
GI-4-49
GI-4-54
GI-2-65
GI-4-72
DA-1-17
DA-1-19
DA-1-25
DA-1-35
DA-1-36
AC-1-65
AC-1-71
AC-1-111

Figure 5. Inventory of thin sections via photomosaic imaging in transmitted plane light on Zeiss LSM 900. Corresponding epoxied billets were made for each of these thin sections (billets not shown). Each image is a mosaic of 5× plane polarized transmitted light sub-images taken over the entire given thin section. The standard thin sections are 27 mm × 46 mm × 30 µm.

Table 4. Composition and porosity type percentages from optical petrography point counts.

Sample ID	Lith. Unit	Matrix (%)	Pumice (%)	Phenocrysts (%)	Lithics Fragments (%)	Total Porosity (%)	Interstitial Porosity (%)	Intragranular Porosity (%)
GI-2-6	VNT-1	51.8	38.1	6.2	3.8	36.3	27.9	8.4
GI-3-2	VNT-2	20.3	56.9	10.1	12.7	32.4	12.7	19.7
GI-4-8	VNT-2	73.2	20.3	5.5	1.0	9.4	6.0	3.4
GI-4-18	VNT-3	70.5	20.0	7.6	2.0	17.6	10.5	7.1
GI-4-35	VNT-3	33.1	58.1	1.9	6.9	23.5	14.0	9.5
GI-3-51	VNT-4	34.3	43.2	5.5	17.0	27.1	13.3	13.9
GI-4-49	VNT-4	28.8	54.8	5.8	10.7	27.0	7.5	19.4
GI-4-54	VNT-4	22.3	63.8	6.4	7.4	35.2	9.5	25.8
GI-2-65	VNT-5	45.8	45.4	6.7	2.0	25.4	10.1	15.3
GI-4-72	VNT-5	30.9	56.1	7.2	5.8	31.6	14.7	16.9
DA-1-17	VNT-6	48.8	36.7	11.9	2.6	31.5	24.2	7.3
DA-1-19	VNT-7	18.5	56.2	18.3	7.0	24.4	8.6	15.8
DA-1-25	VNT-8	53.8	29.2	13.6	3.3	30.2	18.6	11.6
DA-1-35	VNT-9	51.5	14.1	20.3	14.1	23.9	19.3	4.6
DA-1-36	VNT-10	36.3	17.3	41.8	4.6	16.0	9.2	6.9
AC-1-65	UZNT	42.8	29.5	19.4	8.3	28.9	18.2	10.8
AC-1-71	UZNT	28.8	26.1	31.4	13.7	20.6	10.8	9.8
AC-1-111	UZNT	43.6	36.2	15.3	4.9	31.9	17.9	14.0

Note: Lith. = lithologic

VNT-1 Unit
Thin Section Sample: U12p.06 GI-2-6

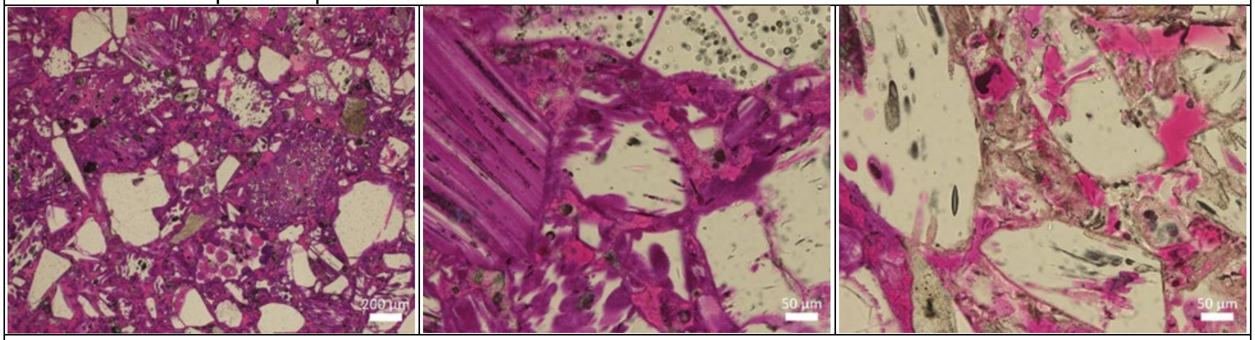

- Vitric pumice and glass shards with no anisotropy; fine-grained zeolite is more common as matrix and vesicle fill at upper, left, and lower edges of thin section
- Fine to medium grain sizes with abundant pumice within full range of grain sizes
- Finer-grained ash and fragments commonly found between larger components, but interstitial porosity still remains (very little post-depositional compaction)
- Dominant pore-lining phases: volcanic glass with lesser zeolite and rare clay

Figure 6. Plane light photomicrographs for thin section U12p.06 GI-2-6 with petrographic observations.

VNT-2
Sample: U12p.06 GI-3-2

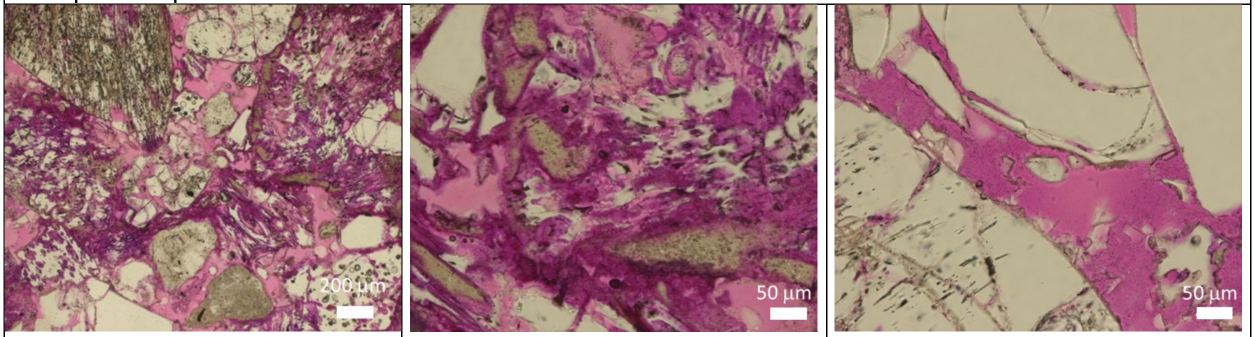

- Vitric pumice and glass shards with no anisotropies or zonation in texture
- Medium to coarse grain sizes, with pumice dominating sample (consistent with pumice fall tuff)
- Dominant pore-lining phases: volcanic glass and smectite

Figure 7. Plane light photomicrographs for thin section U12p.06 GI-3-2 with petrographic observations.

VNT-2
Sample: U12p.06 GI-4-8

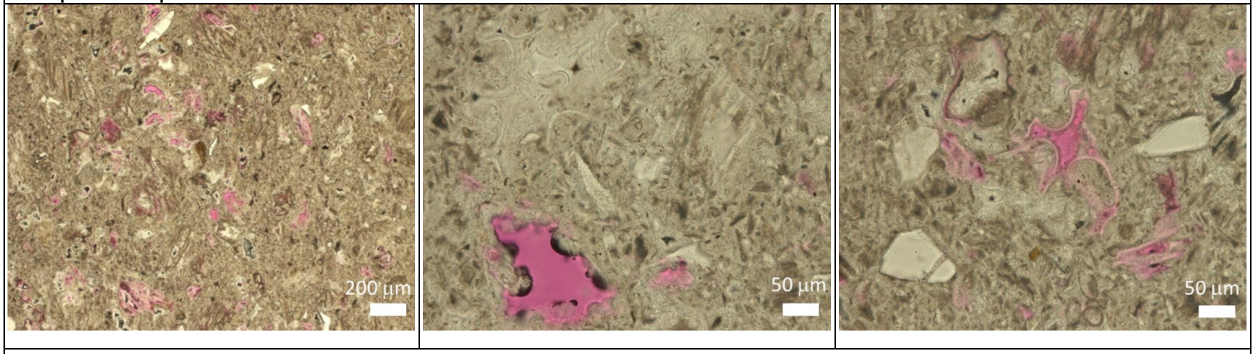

- Zeolitized and variably opal-cemented pumice and matrix, creating low porosity, competent tuff that contains natural fractures
- Overall finer grain sizes and matrix-dominated
- Dominant pore-lining phases: zeolite and opal

Figure 8. Plane light photomicrographs for thin section U12p.06 GI-4-8 with petrographic observations.

VNT-3
Sample: U12p.06 GI-4-18

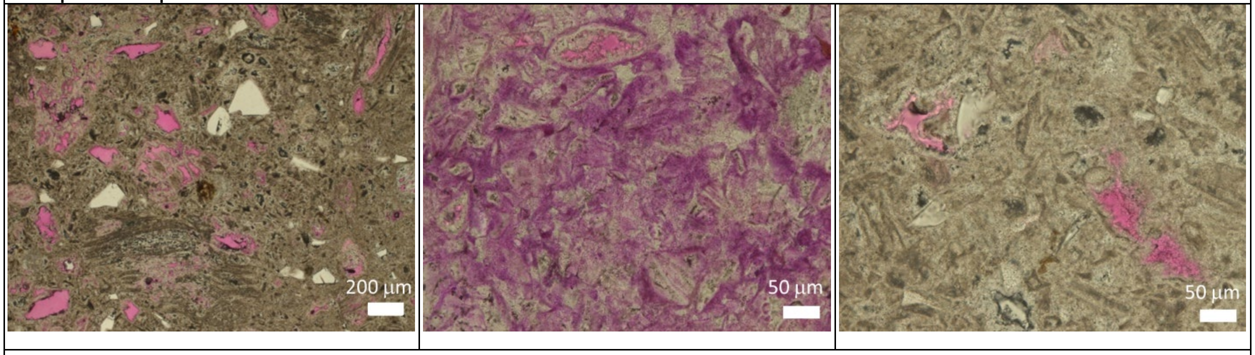

- Highly heterogeneous and anisotropic distributions of glassy, zeolitized, and zeolitized/opal-cemented pumice and matrix (curved bands), creating variable porosity across sample as well as fractures in the more cemented/zeolitized portions.
- Fine-medium grain sizes, matrix-dominated overall
- Dominant pore-lining phases: zeolite, opal, and volcanic glass

Figure 9. Plane light photomicrographs for thin section U12p.06 GI-4-18 with petrographic observations.

VNT-3
Sample: U12p.06 GI-4-35

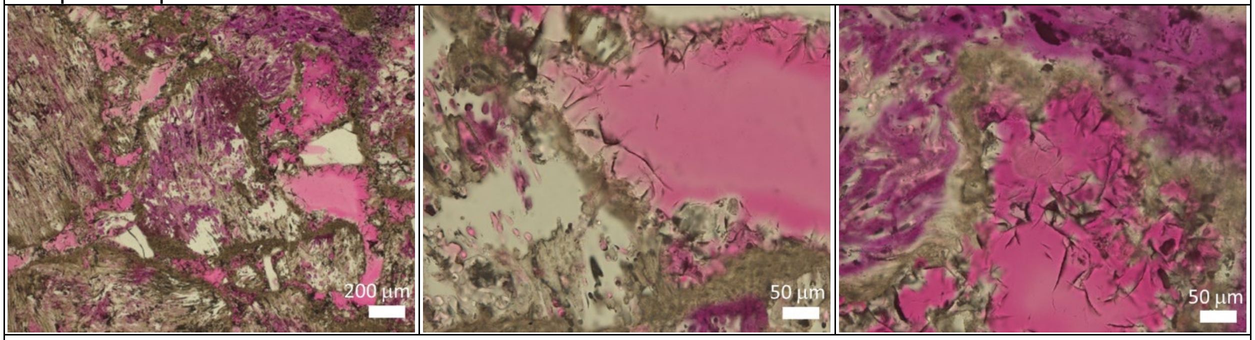

- Incipiently zeolitized pumice and matrix glass with widespread incipient alteration rims and needle-like clay growths into pore spaces; no anisotropies or zonation in texture across sample
- Medium-coarse grain sizes, less matrix-dominated for an ash-fall tuff
- Dominant pore-lining phases: volcanic glass and smectite

Figure 10. Plane light photomicrographs for thin section U12p.06 GI-4-35 with petrographic observations.

VNT-4
Sample: U12p.06 GI-3-51

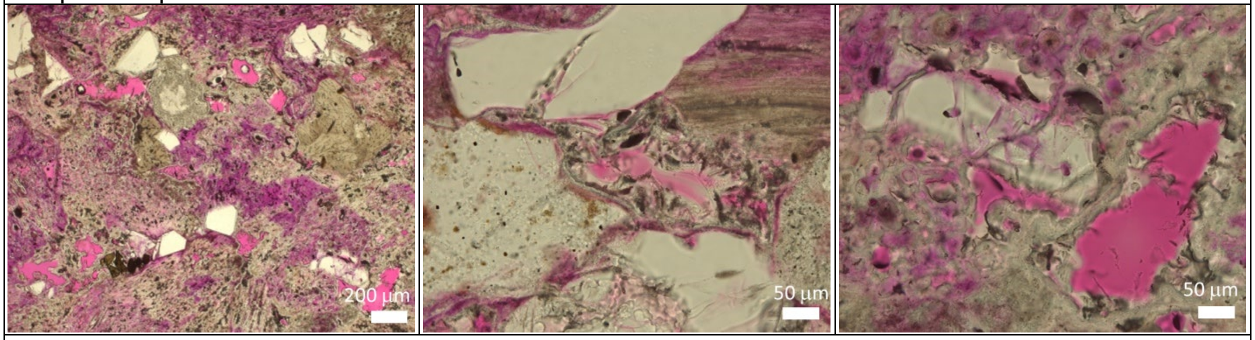

- Largely zeolitized and opal-cemented matrix with variably zeolitized pumice and some zones of only incipiently zeolitized or clay-altered matrix; large voids common in between larger components and in cores of relict pumice
- Heterogeneous, poorly sorted, and layered components with pumice-rich zone at bottom and top of sample; matrix-dominated in middle
- Dominant pore-lining phases: zeolite with lesser opal and smectite

Figure 11. Plane light photomicrographs for thin section U12p.06 GI-3-51 with petrographic observations.

VNT-4
Sample: U12p.06 GI-4-49

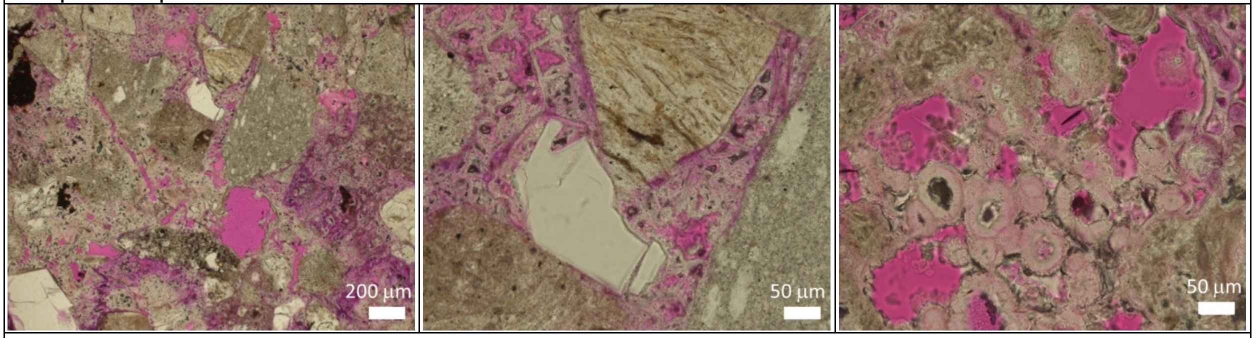

- Incipiently to moderately zeolitized pumice and matrix with a weak alignment of pumice diagonal to thin section; zeolitization is zoned within individual pumice clasts and many relict shards and pumice are outlined with zeolite and contain voids at their cores
- Heterogeneous, poorly sorted components dominated by pumice
- Dominant pore-lining phases: zeolite and volcanic glass

Figure 12. Plane light photomicrographs for thin section U12p.06 GI-4-49 with petrographic observations.

VNT-4
Sample: U12p.06 GI-4-54

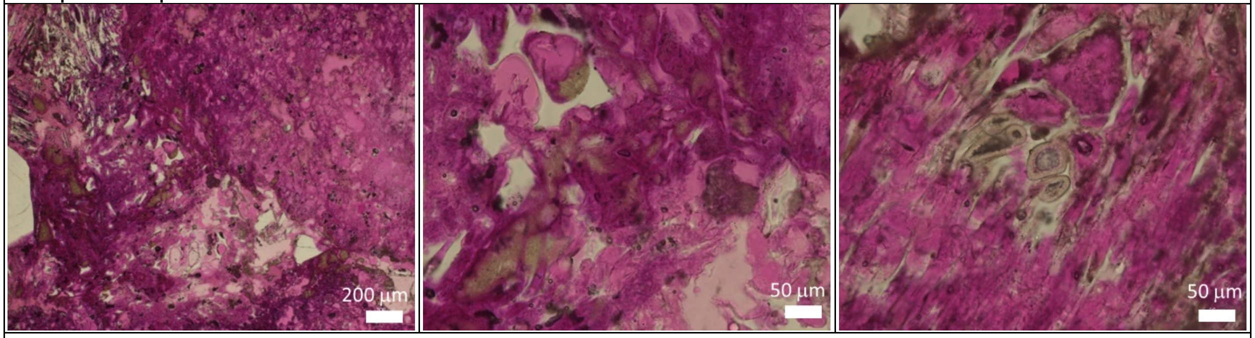

- Vitric pumice and matrix with isolated zeolitization and alteration to clay within pumice vesicles and lining exterior of some pumice; matrix contains minimal pockets of clay-sized material; slight anisotropy defined by elongate pumice
- Medium to large grain sizes, dominated by pumice
- Dominant pore-lining phases: volcanic glass with lesser zeolite and smectite

Figure 13. Plane light photomicrographs for thin section U12p.06 GI-4-54 with petrographic observations.

VNT-5
Sample: U12p.06 GI-2-65

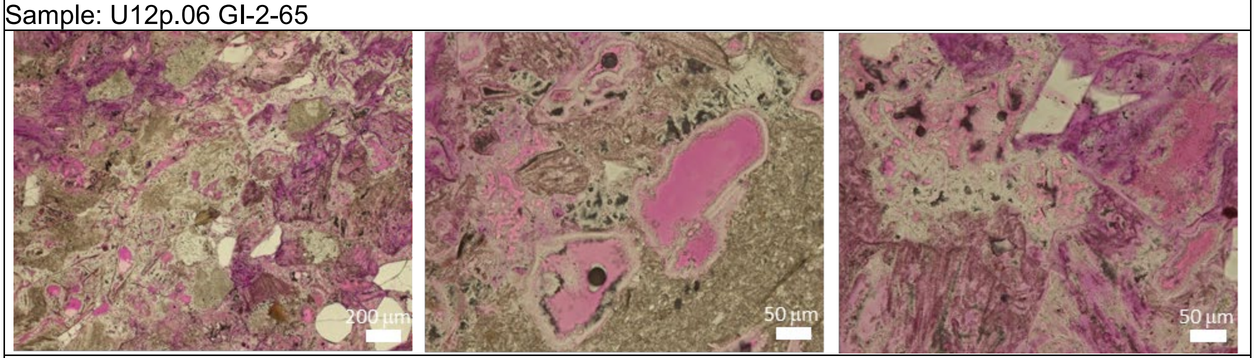

- Alternating bands of 1) glassy to incipiently zeolitized pumice and matrix glass and 2) zeolitized pumice and matrix glass and 3) reworked matrix (low porosity).
- Incipiently zeolitized pumice still retains some vesicular texture
- Zeolitized pumice commonly has cores removed interpreted to be due to vapor-phase removal during alteration; zeolitized matrix commonly consists of euhedral clinoptilolite crystals, with some portions solid
- Where glass is only incipiently zeolitized, pink epoxy shows through glass (pink does not always indicate porosity)
- Fine to medium grain sizes with roughly equal amounts of pumice and matrix
- Dominant pore-lining phases: zeolite with lesser volcanic glass

Figure 14. Plane light photomicrographs for thin section U12p.06 GI-2-65 with petrographic observations.

VNT-5
Sample: U12p.06 GI-4-72

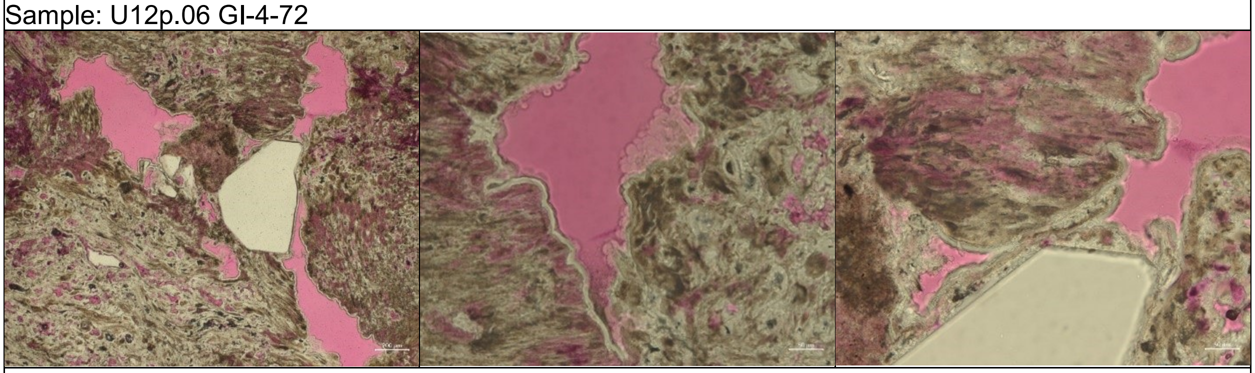

- Varying abundances and sizes of pumice throughout thin section (and core sample) with most glass content incipiently to completely zeolitized, some areas altered to smectite, and most pores lined with opal and/or zeolite
- Heterogeneous, poorly sorted, and layered components with pumice-rich zone at bottom and top of sample; matrix-dominated in middle—very similar to VNT-4 sample GI-3-51
- Dominant pore-lining phases: zeolite and opal with lesser smectite and volcanic glass

Figure 15. Plane light photomicrographs for thin section U12p.06 GI-4-72 with petrographic observations.

VNT-6
Sample: U12p.06 DA-1-17

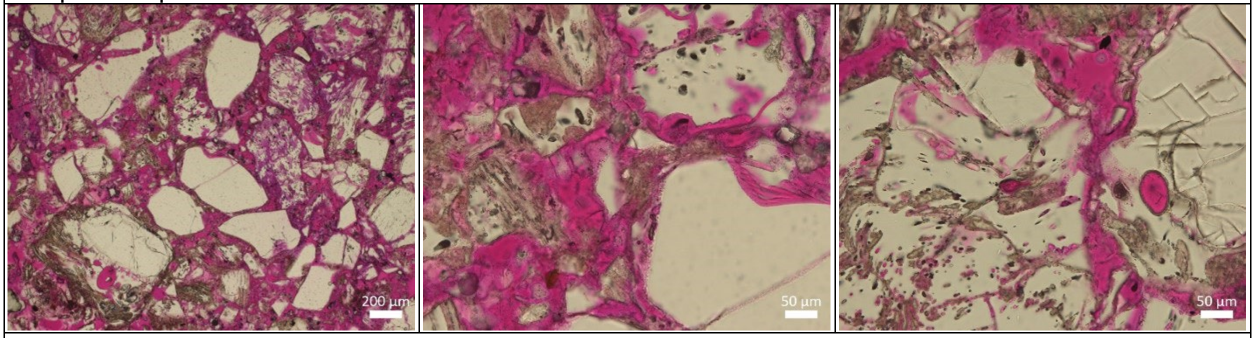

- Mostly vitric ash and pumice fragments with no anisotropy, some incipient zeolitization and clay-linings at pumice and glass fragment boundaries
- Heterogeneity in alteration occurs as incipient zeolitization within matrix at edges of thin section as well as in pumice vesicles and replacing glass walls
- Fine to medium grain sizes with roughly equal amounts of pumice and matrix
- Pumice occurs nearly solid glass clasts (few or no vesicles) just as commonly as highly vesiculated clasts, reducing intragranular porosity
- Dominant pore-lining phases: volcanic glass and clay

Figure 16. Plane light photomicrographs for thin section U12p.06 DA-1-17 with petrographic observations.

VNT-7
Sample: U12p.06 DA-1-19

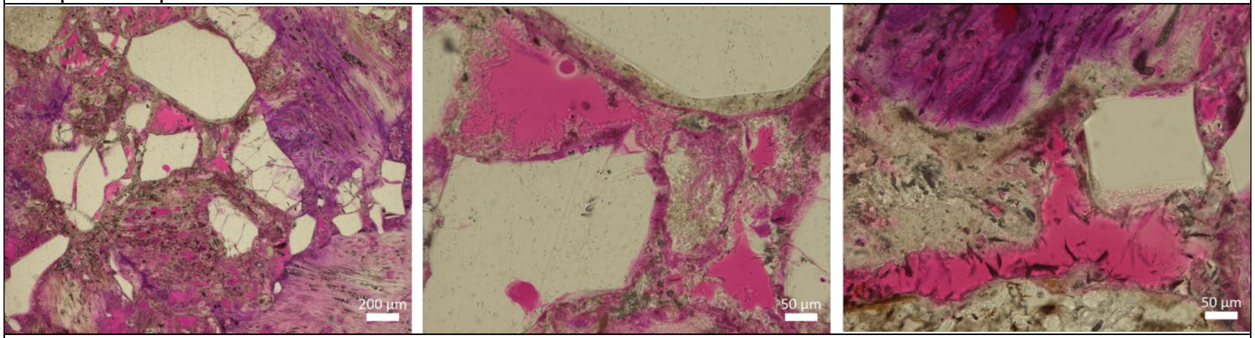

- Vitric and incipiently to moderately zeolitized matrix and pumice with no anisotropy and no heterogeneity beyond typical tuff texture
- Incipiently zeolitized pumice still retains some vesicular texture
- Where glass is only incipiently zeolitized, pink epoxy shows through glass (pink does not always indicate porosity)
- Clay and zeolite rims commonly occur at pumice boundaries
- Medium grain sizes with pumice as dominant component type
- Dominant pore-lining phases: zeolite and clay with lesser volcanic glass

Figure 17. Plane light photomicrographs for thin section U12p.06 DA-1-19 with petrographic observations.

VNT-8
Sample: U12p.06 DA-1-25

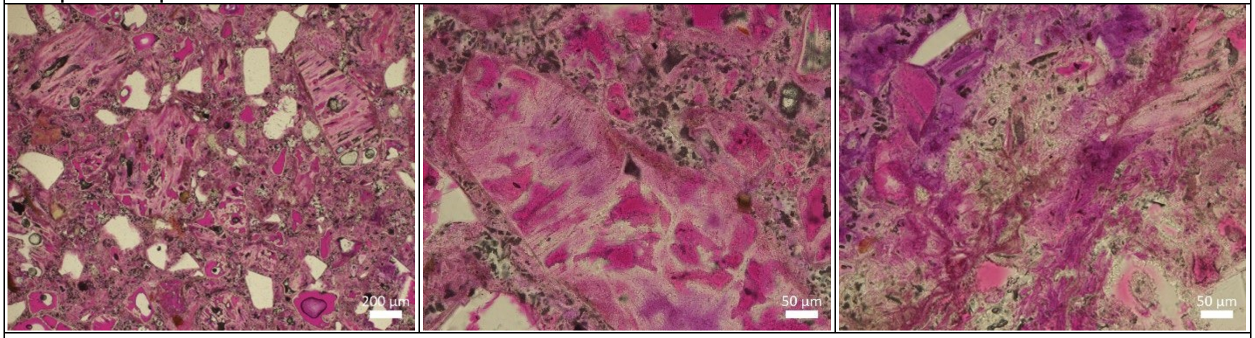

- Incipient to moderately zeolitized matrix and pumice with no anisotropy and no heterogeneity beyond typical tuff texture
- Incipiently zeolitized pumice still retains some vesicular and frothy texture
- Limited intergranular porosity due to zeolitization and ash-sized fragments filling space between components; most porosity is found in void space created by the incomplete process of zeolitization of pumice and glass shards
- Dominant pore-lining phases: zeolite with lesser volcanic glass and smectite

Figure 18. Plane light photomicrographs for thin section U12p.06 DA-1-25 with petrographic observations.

VNT-9
Sample: U12p.06 DA-1-35

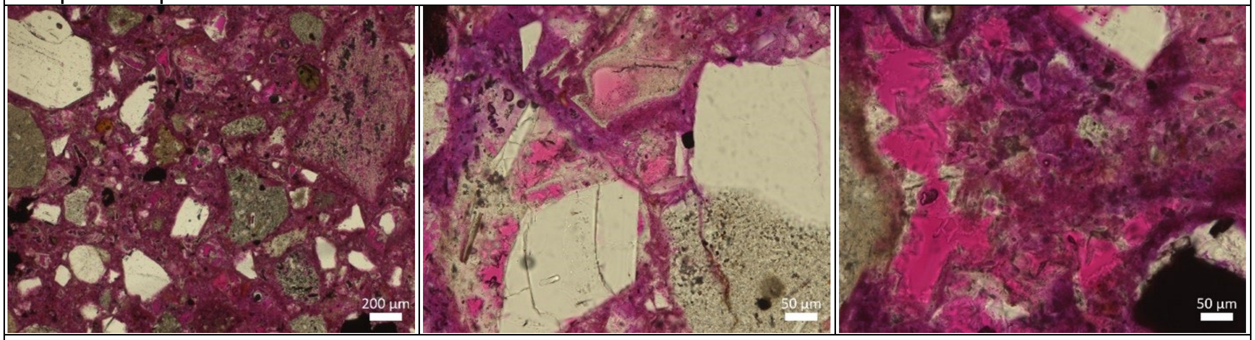

- Incipient to moderately zeolitized matrix and pumice with no anisotropy and no heterogeneity beyond typical tuff texture
- Finer grain size for most components with smallest fragments commonly filling intergranular space
- Zeolite mineralization common along pore/grain boundaries
- Intragranular porosity is common due to incomplete replacement of glass by zeolite in pumice and glass shards
- Dominant pore-lining phases: zeolite with lesser volcanic glass and smectite

Figure 19. Plane light photomicrographs for thin section U12p.06 DA-1-35 with petrographic observations.

VNT-10
Sample: U12p.06 DA-1-36

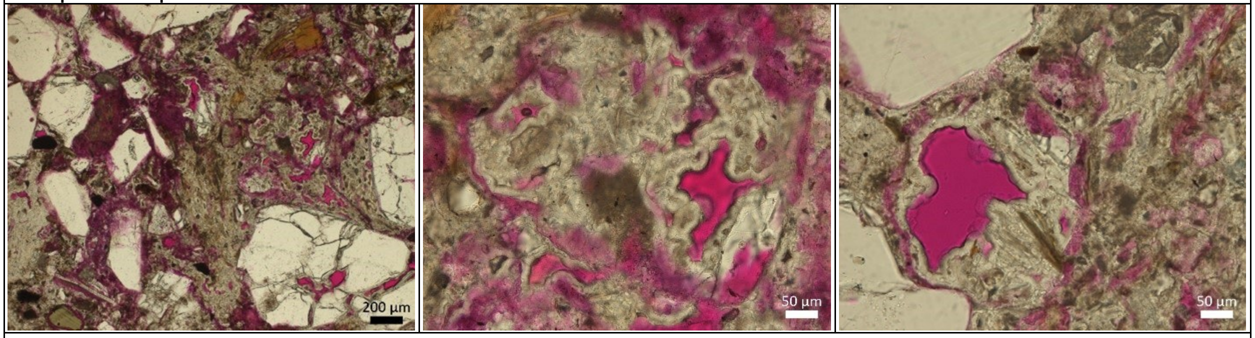

- Incipiently to completely zeolitized matrix and pumice with some smectite alteration occurring as isolated clumps/components and opal lining many pores and filling fractures in phenocrysts; zeolitization and alteration is heterogeneous across thin section, creating a patchy texture, but no anisotropy/alignment of features
- Phenocrysts are particularly abundant with a range of submicron to 2mm grain sizes; larger phenocrysts create a nearly grain-supported texture
- Dominant pore-lining phases: zeolite, smectite, and opal

Figure 20. Plane light photomicrographs for thin section U12p.06 DA-1-36 with petrographic observations.

UZNT
Sample: U12p.06 AC-1-65

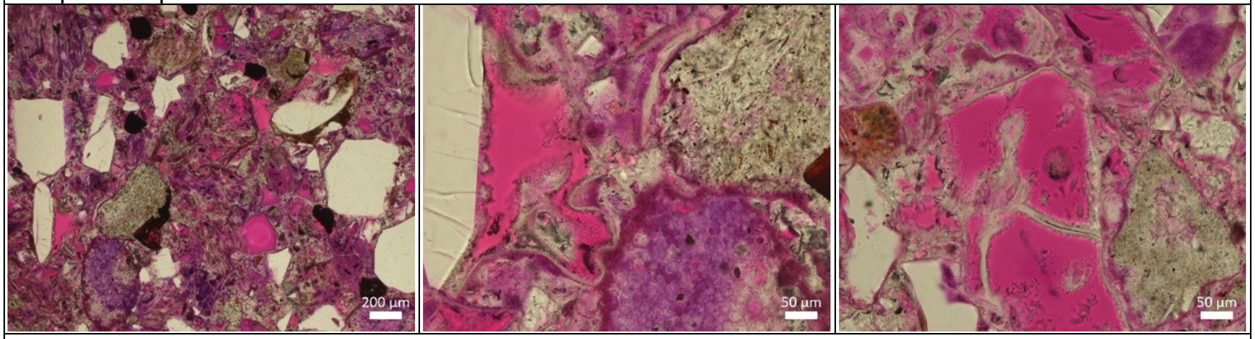

- Incipiently to moderately zeolitized matrix and pumice with no anisotropy or heterogeneity beyond typical tuff texture
- Intergranular spaces are commonly filled or partially filled with small tuff components or zeolite mineralization
- Intragranular porosity is common due to incomplete replacement of glass by zeolite
- Dominant pore-lining phases: zeolite, volcanic glass, and lesser smectite

Figure 21. Plane light photomicrographs for thin section U12p.06 AC-1-65 with petrographic observations.

UZNT
Sample: U12p.06 AC-1-71

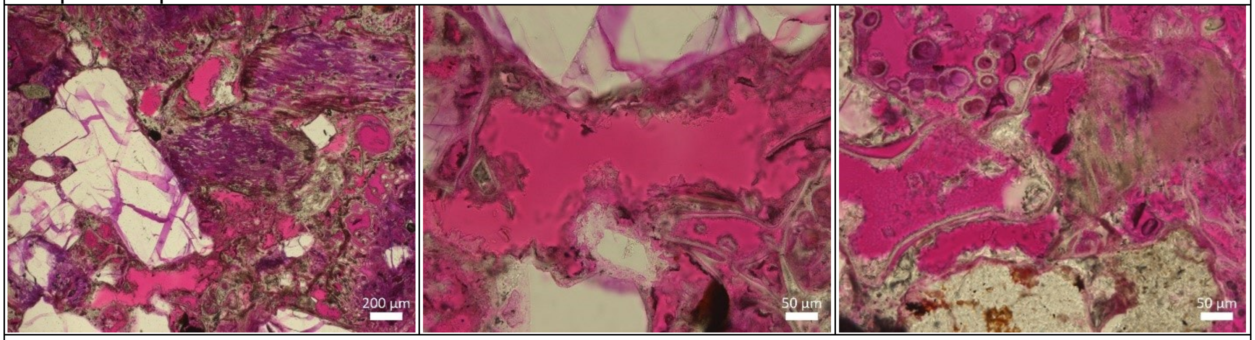

- Incipiently to moderately zeolitized matrix and pumice with patchy zeolitization and local alteration of some volcanic glass to smectite
- Intergranular porosity is locally more prevalent than shallower UZNT sample (AC-1-65), but pores are commonly lined with zeolite
- Dominant pore-lining phases: zeolite with lesser smectite

Figure 22. Plane light photomicrographs for thin section U12p.06 AC-1-71 with petrographic observations.

UZNT
Sample: U12p.06 AC-1-111

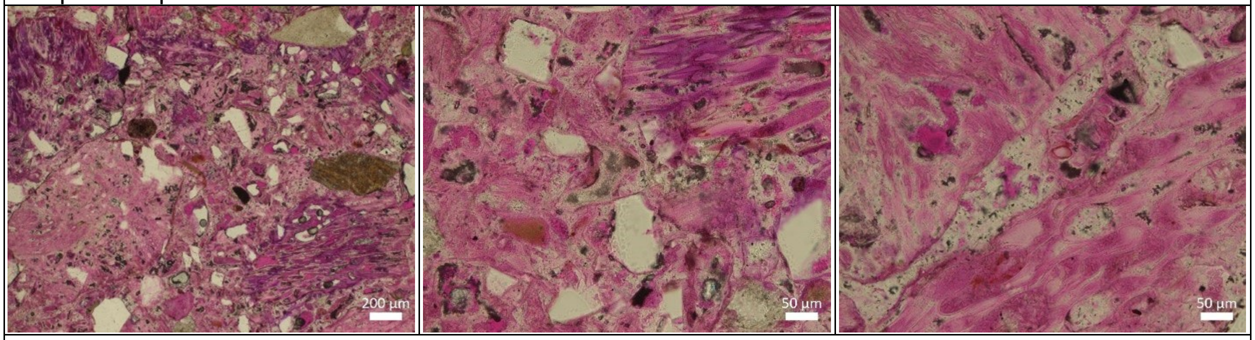

- Incipiently to nearly completely zeolitized matrix and pumice, locally more extensive creating a patchy zeolitic texture but with no anisotropy
- Intergranular porosity is low due to nearly complete zeolitization of matrix and/or filling of voids with submicron component fragments
- Intragranular porosity is moderately prevalent due to incomplete zeolitization of glass in pumice and glass shards
- Dominant pore-lining phases: zeolite with lesser volcanic glass and smectite

Figure 23. Plane light photomicrographs for thin section U12p.06 AC-1-111 with petrographic observations.

3.2.2. SEM-EDS

Thin sections were prepared for scanning electron microscopy (SEM) by coating with a gold-palladium alloy using a Denton Vacuum Desk IV sputter-coater. Microtexture of each thin section was observed and imaged using backscattered electrons (BSE) and secondary electrons (SE) in high-vacuum mode at an accelerating voltage of 20.0 kV on a TESCAN Vega3 Scanning Electron Microscope. In order to confirm presence of key primary and alteration minerals (zeolite, silica, clay minerals, etc.), elemental compositions from select portions of each thin section were obtained using an energy dispersive X-ray (EDAX) system. Energy dispersive (EDS) spectra were collected and analyzed using an Oxford Instruments Xplore 3D EDS detector and AZtec EDS software, version 6.0.

BSE images of volcanic tuff provide a clear view of pore and crystal morphologies due to the readily apparent difference between pores (black) and pore-lining phases (grayscale value dependent on atomic weight). BSE and EDS elemental overlay maps for select thin sections in Figures 24-30 show a progression of volcanic tuff that is mostly vitric (labeled V on maps) with incipient alteration to zeolite and smectite, to tuff with no glass content and correspondingly higher zeolitic content with varying amounts of smectite alteration and silica cementation. These alteration minerals both replace glass and partially to completely, depending on degree of alteration, fill inter- and intragranular pores.

Zeolite morphologies vary, including wispy (Figure 24), skeletal (Figures 25-28), needle-like, and blocky crystals (Figures 29 and 30) growing into pore spaces. Complete closure of pore space can be found in some regions in zeolitized samples (Figure 30). Generally, zeolite is enriched in Ca and Mg and depleted in K and Na compared to the volcanic glass that it replaces. Variations in Si, Al, Na, and K abundances within zeolite are observed and likely reflect different zeolite varieties (clinoptilolite, heulandite, and mordenite) that may form under dynamic diagenetic conditions (e.g., Chipera et al., 2006). Fe- and Mg-enriched smectite occurs as clumps intermixed with zeolite within pumice vesicles and between grains and commonly exhibits desiccation microcracks (Figures 26, 27, 29, and 30). Silica cementation is often nodular and appears to form in pores after alteration of volcanic glass to zeolite and/or smectite (Figure 28).

As mentioned in Section 3.2.1, note that thin section sample preparation may potentially have altered the morphology of water-sensitive phases (e.g., opal, zeolite, and swelling clays). Imaging of preserved samples via environmental SEM in humid environments with a cryo focused ion beam – scanning electron microscopy could be used to further characterization potentially representative morphology of water-sensitive pore-lining phases.

VNT-4
Sample: U12p.06 GI-4-54

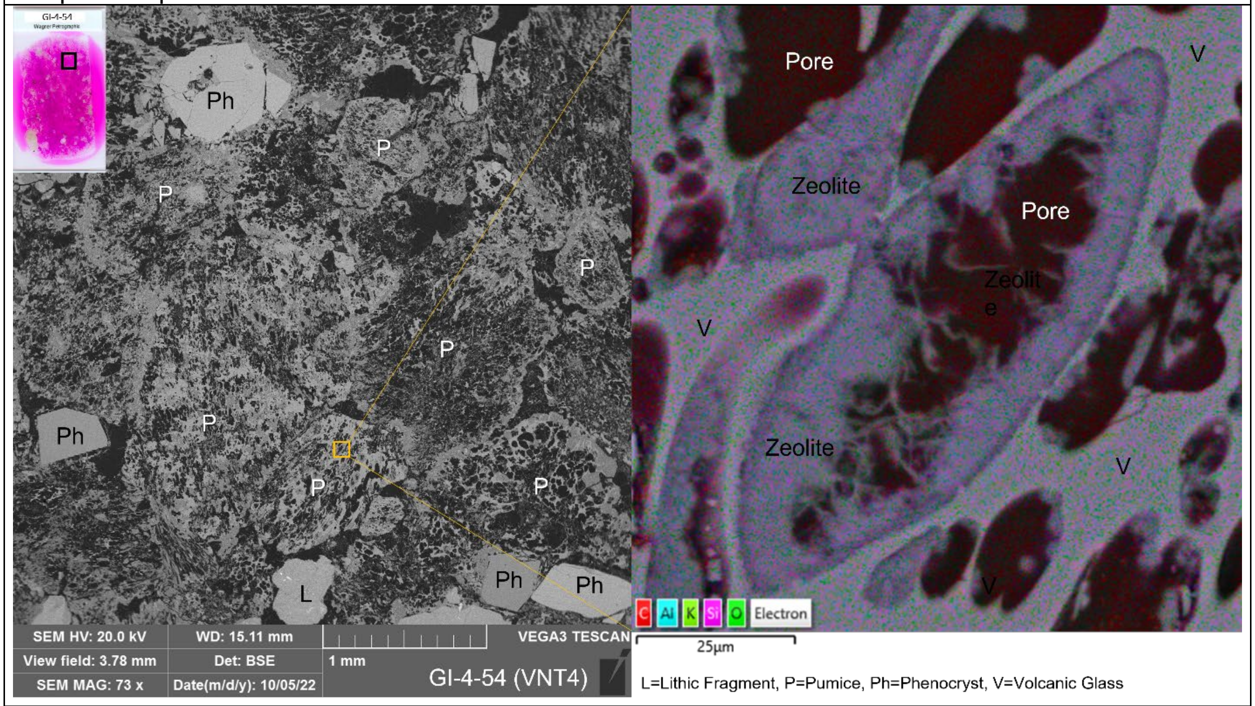

Figure 24. Representative BSE (left) and EDS map (right) from SEM observations of thin section U12p.06 GI-4-54 (VNT-4) with interpretations of relevant phases and textural observations.

VNT-1 Unit
Thin Section Sample: U12p.06 GI-2-6

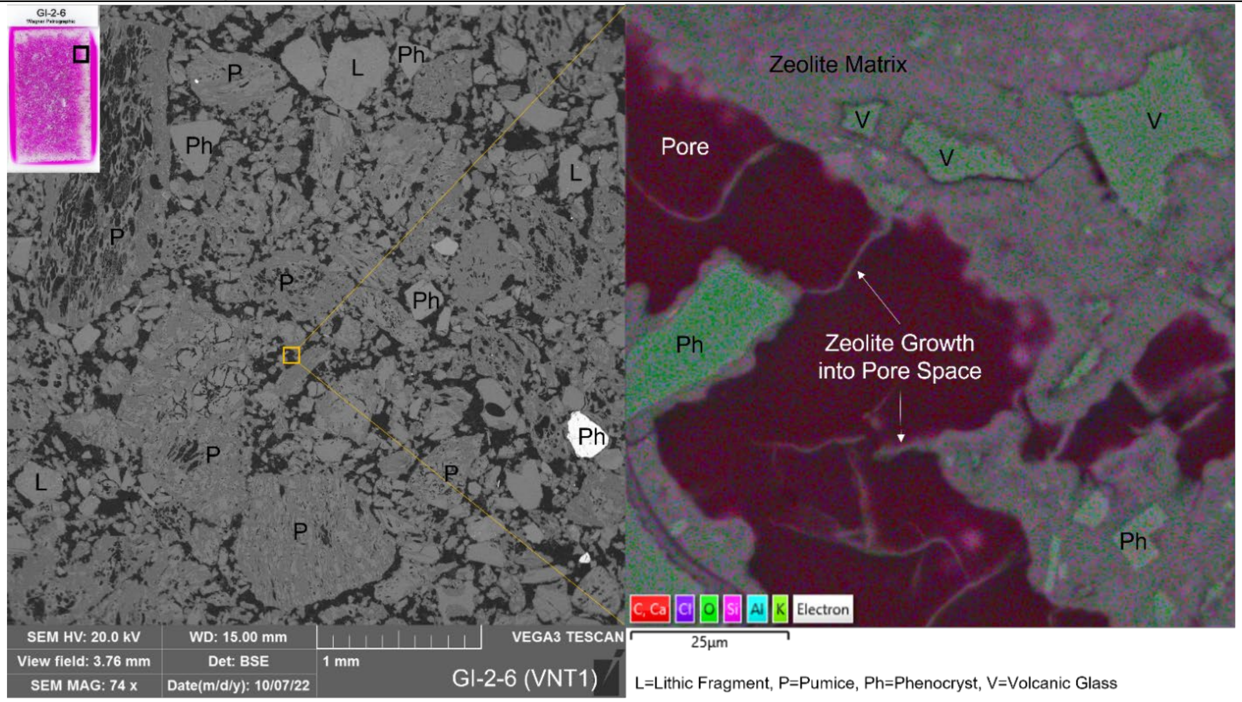

Figure 25. Representative BSE (left) and EDS map (right) from SEM observations of thin section U12p.06 GI-2-6 with interpretations of relevant phases and textural observations.

VNT-3
Sample: U12p.06 GI-4-35

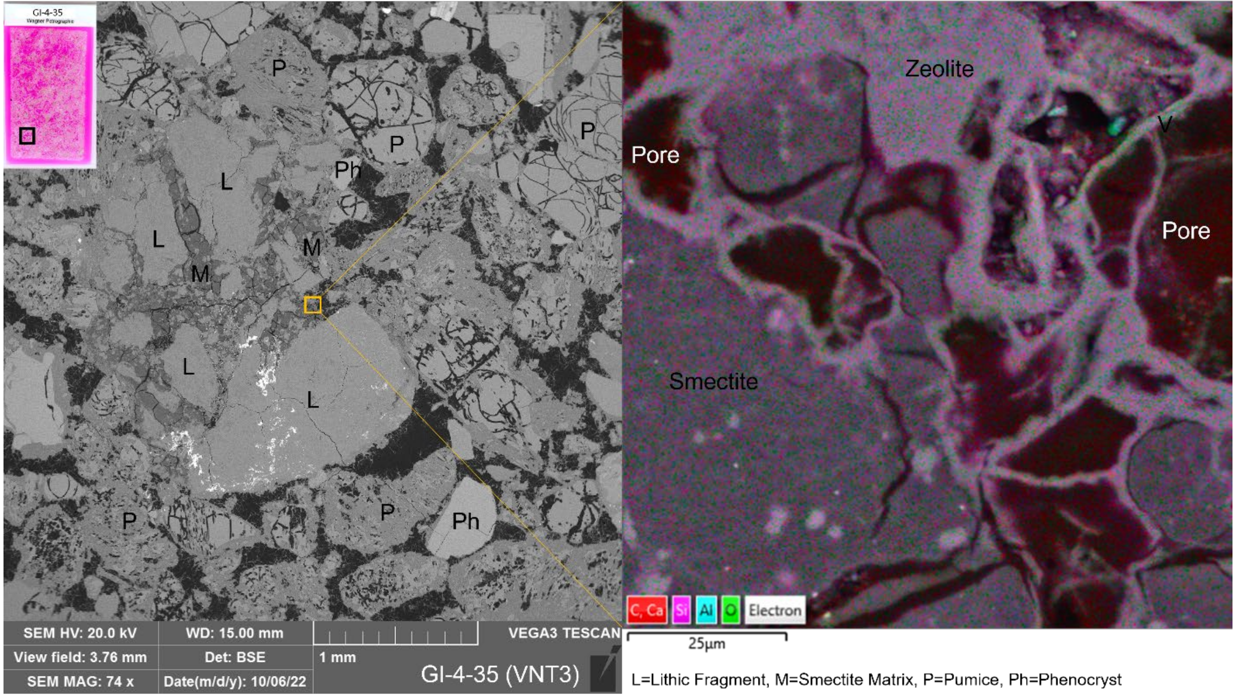

Figure 26. Representative BSE (left) and EDS map (right) from SEM observations of thin section U12p.06 GI-4-35 with interpretations of relevant phases and textural observations.

VNT-6
Sample: U12p.06 DA-1-17

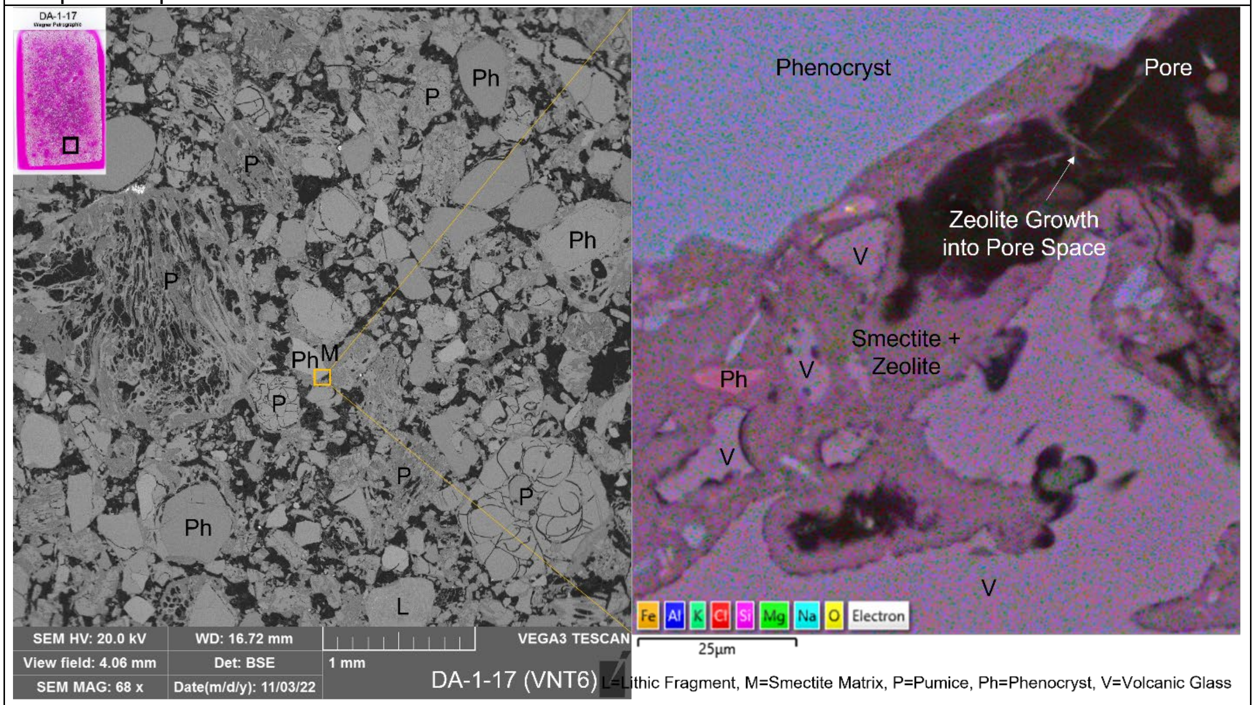

Figure 27. Representative BSE (left) and EDS map (right) from SEM observations of thin section U12p.06 DA-1-17 with interpretations of relevant phases and textural observations.

VNT-4
Sample: U12p.06 GI-4-49

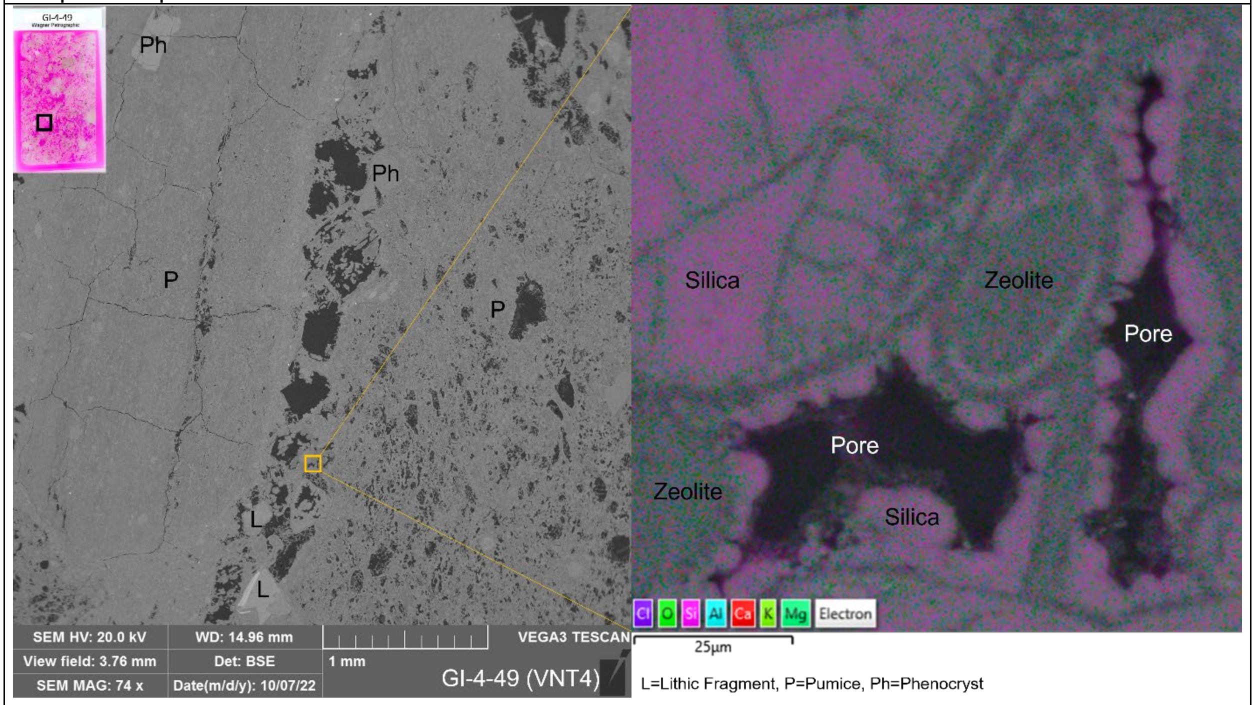

Figure 28. Representative BSE (left) and EDS map (right) from SEM observations of thin section U12p.06 GI-4-49 with interpretations of relevant phases and textural observations.

UZNT
Sample: U12p.06 AC-1-111

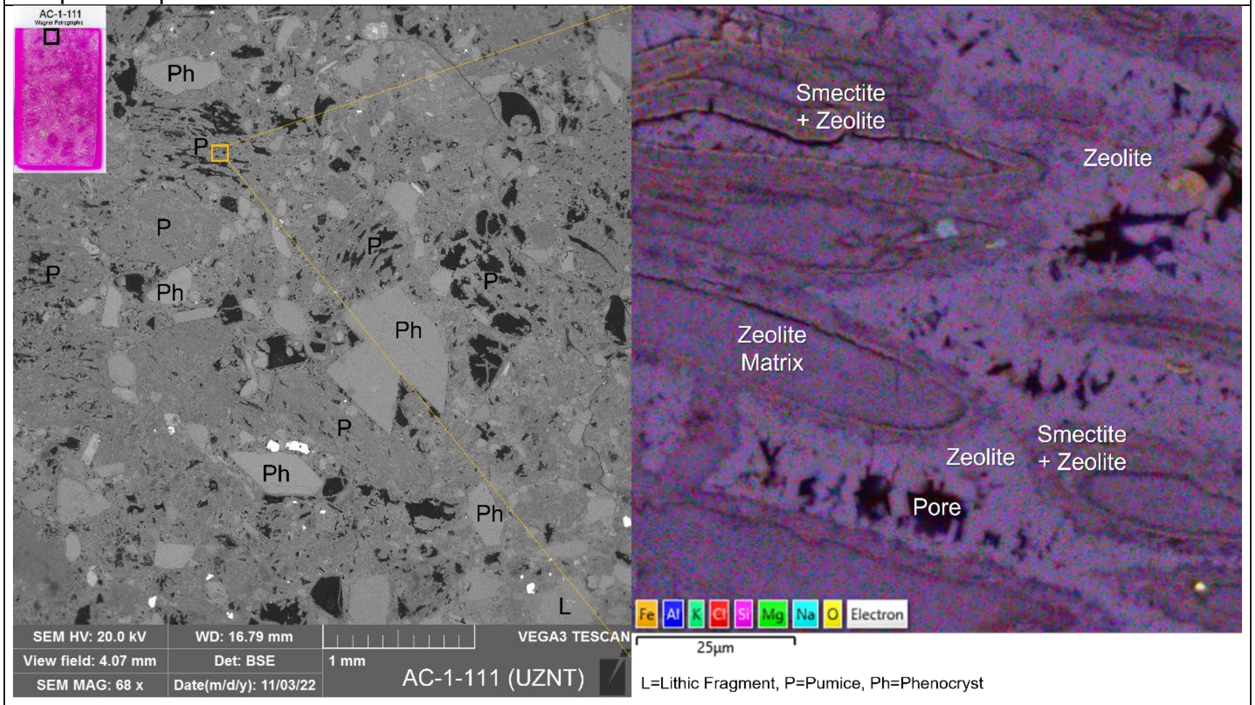

Figure 29. Representative BSE (left) and EDS map (right) from SEM observations of thin section U12p.06 AC-1-111 with petrographic observations.

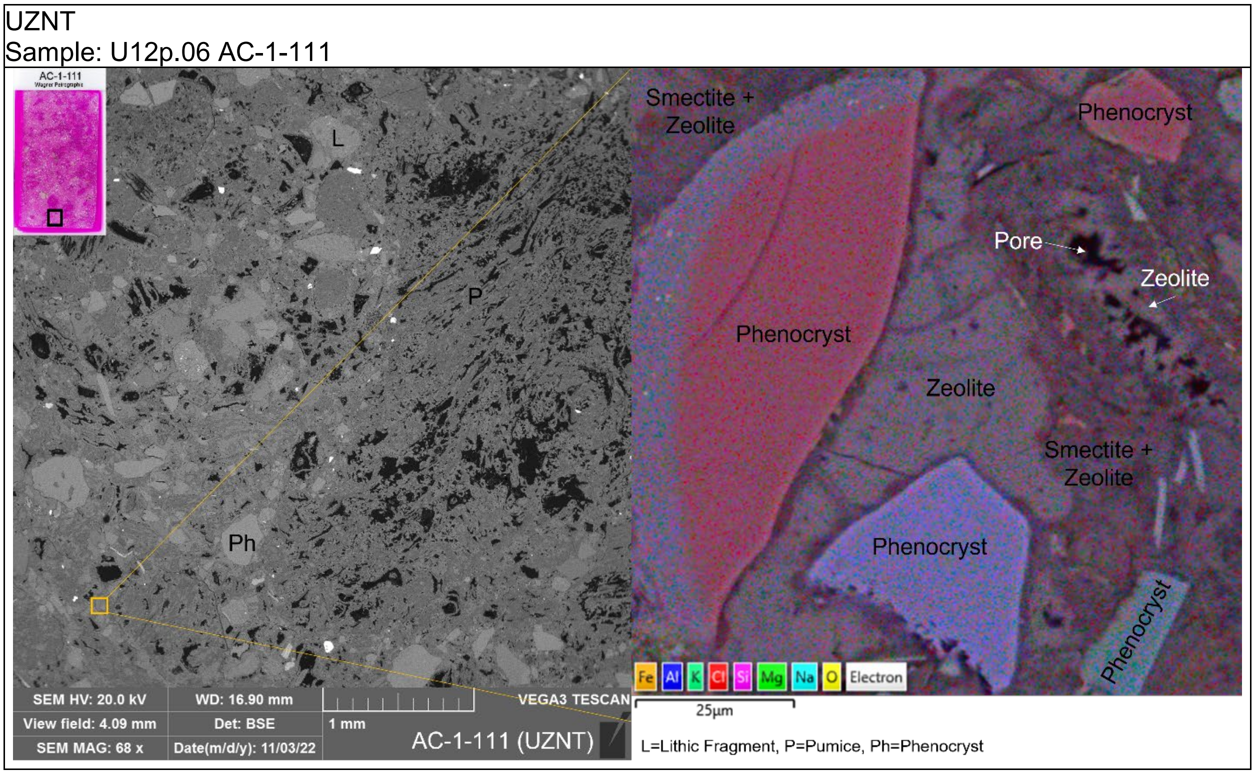

Figure 30. Representative BSE (left) and EDS map (right) from SEM observations of thin section U12p.06 AC-1-111 with interpretations of relevant phases and textural observations.

3.2.3. X-ray Diffraction

Samples for XRD were prepared from rock material trimmed away from each thin section billet so that the XRD results correlate to optical petrography. Trimming was performed with a Buehler IsoMet1000 Precision saw using DI water as lubricant. The material removal for XRD was such that it would provide at least 10 grams of ground-up material. The rock material was sent to Premier Oilfield Group LLC, which performed bulk and clay-sized fraction analyses. The XRD analysis equipment includes Bruker D8 and/or D4 diffractometers with a 2θ goniometer and 250-cm radius, Cu Kα radiation, a SSD160 Lynxeye detector, and a 0.6 mm divergence slit and 4.1° Soller slits for optimal intensity-resolution ratio. Sample preparation included homogenization, McCrone wet milling, spray drying, and front and/or side loading. The clay-size fraction at <2 µm was obtained by sonication and centrifugation, and oriented clay preparation used a filter transfer method. Clay expandability was determined using the clay separation-glycolation-heat treatment method (Moore and Reynolds, 1997), aided by the NEWMOD clay modelling software (Yuan and Bish, 2010). Mineral quantification used the Reference Intensity Ratio method, aided by Bruker EVA DIFFRAC SUITE software (Giencke, 2007) and the PDF4+ mineral database (Fawcett et al., 2018), and quantification was performed using customized Mineral Intensity Factor (MIF) values obtained from commercial and in-house standards. The mineral percentages are reported as weight percent.

Table 5 and Table 6 present the bulk and clay-sized fraction XRD results. The VNT units of the PE1 testbed can contain highly variable and at times very high percentages of secondary (i.e., diagenetic) phases including zeolites (e.g.., clinoptilolite or heulandite), clay, and opal.

Table 5. X-ray diffraction results of bulk analysis.

Sample ID	Lith. Unit	Framework Silicate			Clay	Other											Total
		Qtz	Plag	Kfsp	Clay	Clin	Heu	Amph	Crst	Tridy	Amorph	Opal C	Opal CT	Opal A	Obsid	Volc glass	
		%	%	%	%	%	%	%	%	%	%	%	%	%	%	%	%
GI-2-6	VNT-1	10.0	7.5	11.0	2.4	9.9	13.3	0.0	0.9	Tr	45.0	-	-	-	Tr	++	100.0
GI-3-2	VNT-2	7.5	3.0	7.7	33.4	2.4	0.0	0.0	0.0	0.0	46.0	+	-	++	-	-	100.0
GI-4-8	VNT-2	5.0	2.0	6.6	2.5	49.3	0.0	0.0	0.0	0.0	34.6	+	++	+	-	-	100.0
GI-4-18	VNT-3	5.8	1.5	6.5	1.7	18.5	0.0	0.0	0.0	0.0	66.0	+	+	++	-	-	100.0
GI-4-35	VNT-3	5.7	1.3	5.9	1.1	18.0	0.0	0.0	0.0	0.0	68.0	+	+	++	-	-	100.0
GI-3-51	VNT-4	3.8	2.3	6.0	4.9	60.0	0.0	0.0	0.0	0.0	23.0	+	++	+	-	-	100.0
GI-4-49	VNT-4	7.8	1.1	8.4	1.6	57.1	0.0	0.0	0.0	0.0	24.0	++	+	+	-	-	100.0
GI-4-54	VNT-4	5.6	0.8	6.6	21.0	21.0	0.0	0.0	0.0	0.0	45.0	+	-	++	-	-	100.0
GI-2-65	VNT-5	3.5	3.5	7.0	1.6	63.4	0.0	0.0	0.0	0.0	21.0	+	++	+	-	-	100.0
GI-4-72	VNT-5	5.0	0.9	6.9	4.6	59.8	0.0	0.0	0.0	0.0	22.8	++	+	+	-	-	100.0
DA-1-17	VNT-6	13.0	9.4	16.0	13.5	9.0	Tr	0.0	0.5	Tr	38.6	-	-	-	Tr	++	100.0
DA-1-19	VNT-7	10.0	8.0	6.0	10.9	9.4	34.0	0.0	1.5	Tr	20.2	-	-	-	Tr	++	100.0
DA-1-25	VNT-8	9.2	11.0	8.0	11.2	8.8	32.3	0.0	1.0	Tr	18.5	-	-	-	Tr	++	100.0
DA-1-35	VNT-9	8.6	25.0	13.3	10.4	4.0	18.0	1.0	1.0	Tr	18.7	-	-	-	Tr	++	100.0
DA-1-36	VNT-10	3.0	25.5	10.0	23.0	9.0	4.0	2.2	0.7	Tr	22.6	-	-	-	Tr	++	100.0
AC-1-65	UZNT	8.5	20.0	10.3	9.9	30.0	6.0	0.0	Tr	Tr	15.3	-	-	-	Tr	++	100.0
AC-1-71	UZNT	9.5	27.1	15.0	8.7	16.0	5.0	0.7	Tr	Tr	18.0	-	-	-	Tr	++	100.0
AC-1-111	UZNT	7.3	19.0	9.8	9.1	31.4	9.0	0.0	Tr	Tr	14.4	-	-	-	Tr	++	100.0

++ major amorphous phase; + minor amorphous phase; - not detected; Lith., Lithologic *Note:* Key to mineral abbreviations: Qtz, Quartz; Plag, Plagioclase; Kfsp, K-feldspar; Clay, Total Clay + Mica; Clin, Clinoptilolite; Heu, Heulandite; Amph, Amphibole; Crst, Cristobalite; Tridy, Tridymite; Amorph, Total amorphous phases; Obsid, Obsidian; Volc. glass, volcanic glass; Total, Total of Minerals; Tr, trace amounts; minerals not detected across all samples include Calcite, Dolomite, Fe-Dolomite, Anatase, and Pyrite.

Table 6. X-ray diffraction results of clay fraction analysis.

Sample ID	Lith. Unit	Clay Minerals						
		Na-Sme	Al-Sme	ML I/S	Ill+Mic	Chl	ML I/S Exp	Total
		%	%	%	%	%	%	%
GI-2-6	VNT-1	0.0	2.0	0.0	0.4	0.0	-	2.4
GI-3-2	VNT-2	31.7	0.0	0.0	1.7	0.0	-	33.4
GI-4-8	VNT-2	1.2	0.0	0.0	0.6	0.0	-	1.8
GI-4-18	VNT-3	0.7	0.0	0.0	1.0	0.0	-	1.7
GI-4-35	VNT-3	0.8	0.0	0.0	0.3	0.0	-	1.1
GI-3-51	VNT-4	4.9	0.0	0.0	Tr	0.0	-	4.9
GI-4-49	VNT-4	1.6	0.0	0.0	Tr	0.0	-	1.6
GI-4-54	VNT-4	0.0	21.0	0.0	Tr	0.0	-	21.0
GI-2-65	VNT-5	0.6	0.0	0.0	1.0	0.0	-	1.6
GI-4-72	VNT-5	4.6	0.0	0.0	Tr	0.0	-	4.6
DA-1-17	VNT-6	0.0	8.7	2.8	2.0	0.0	80-90	13.5
DA-1-19	VNT-7	0.0	6.1	2.0	2.8	0.0	80-90	10.9
DA-1-25	VNT-8	0.0	3.1	3.5	4.6	0.0	80-90	11.2
DA-1-35	VNT-9	0.0	2.0	4.0	4.4	0.0	80-90	10.4
DA-1-36	VNT-10	0.0	17.0	1.0	5.0	0.0	80-90	23.0
AC-1-65	UZNT	0.0	8.0	0.0	1.9	0.0	-	9.9
AC-1-71	UZNT	0.0	7.0	0.0	1.7	0.0	-	8.7
AC-1-111	UZNT	0.0	7.8	0.0	1.3	0.0	-	9.1

Note: Lith. = lithologic*;* Key to mineral abbreviations: Na Sme, Discrete Na-rich smectite; Al Sme, Discrete Al-rich smectite; ML I/S, Mixed-Layer Illite/Smectite; Ill+Mic, Illite + Mica; Chl, Chlorite; ML I/S Exp, Average Expandability of Mixed-Layer Illite/Smectite (Percent Expandable Layers); Total, Total of Minerals; Tr, Trace Amounts

3.2.4. *Spatial X-ray Fluorescence and Compositional Analysis*

A Bruker M4 Tornado μ-XRF mapping system was used for spatial X-ray fluorescence mapping on polished thin section or polished epoxied billets (see Section 3.2.1). The system includes a micro-focused Rh source (50 kV, 200 μA) with a poly-capillary optic and a silicon-drift detector for collection of fluorescence spectra at approximately 25 μm spatial resolution (for further details, see Rodriguez et al., 2012). The XRF scanning produces spectra (intensity versus energy) for each pixel where the mapping step size was 50 microns in both x and y dimensions, thus resulting in large data cubes that require post-processing to reduce the per pixel spectrum to spatially significant groups of phases (e.g., minerals or non-mineral mineraloid or amorphous phases such as opal or glass). SNL's in-house principal component analysis (PCA) and multivariate statistical analysis (MSA) software was used for the post-processing the spatial spectral data (Kotula et al., 2006; Rodriguez et al., 2013; see Heath et al., 2012, for a geologic application of the MSA software).

Post-processing of the spatial XRF data produces two-dimensional (2D) maps of the solid phases (minerals, mineraloids, and amorphous phases) in terms of a score from the PCA with an associated representative spectrum for the scored phases (Figure 31 through Figure 35), which can be used in further post-processing (e.g., via segmentation for quantification of phases). The PCA analysis used 2×2 binning on the spatial XRF data, and thus the PCA resulting resolution is 100 μm.

Thin sections GI-4-35, GI-4-49, GI-4-54, and GI-4-72 have been scanned, as well as polished billets GI-4-54 and GI-4-72. Notable findings include that the spatial XRF with PCA seems to be able to distinguish different types of silica including crystalline quartz and amorphous phases including volcanic glass and opal. Zones of different types of diagenesis are visible, for example, in Figure 35 where the left portion of the thin section is rich in opal and the right portion contains abundant zeolite.

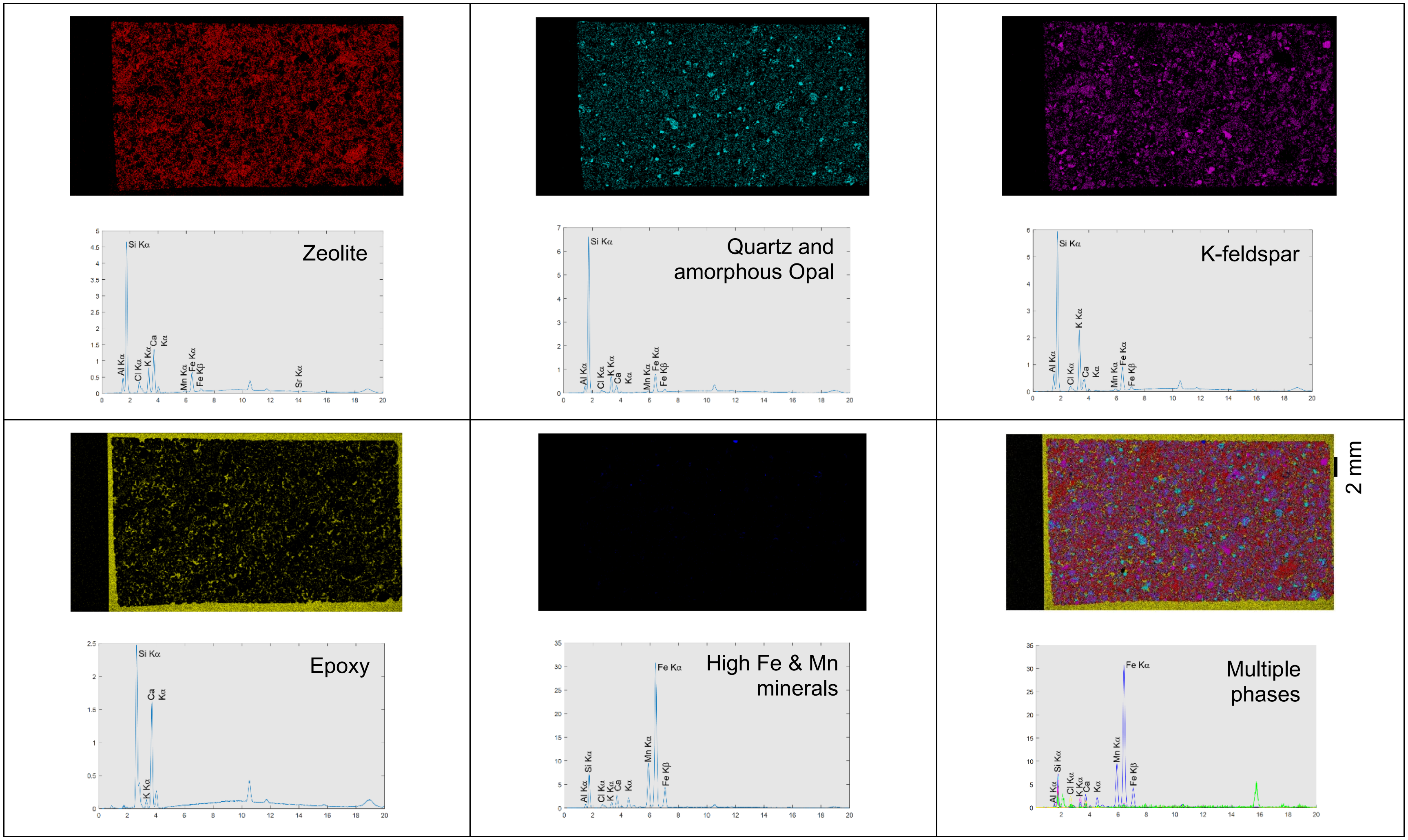

Figure 31. A subset of results of principal component analysis (PCA) and multivariate statistical analysis on thin section GI-4-35 (VNT-3). The images display spatial rendering of the PCA-identified chemical phases for the associated representative PCA-spectrum. The y-axes of the spectra are normalized counts such that, for a particular chemical phase, the product of the normalized counts and the intensity of the corresponding component image (not shown) results in counts equivalent to the original X-ray counts. The x-axes are X-ray energy (kV). The color intensity of a given image is proportional to the concentration of the chemical phase.

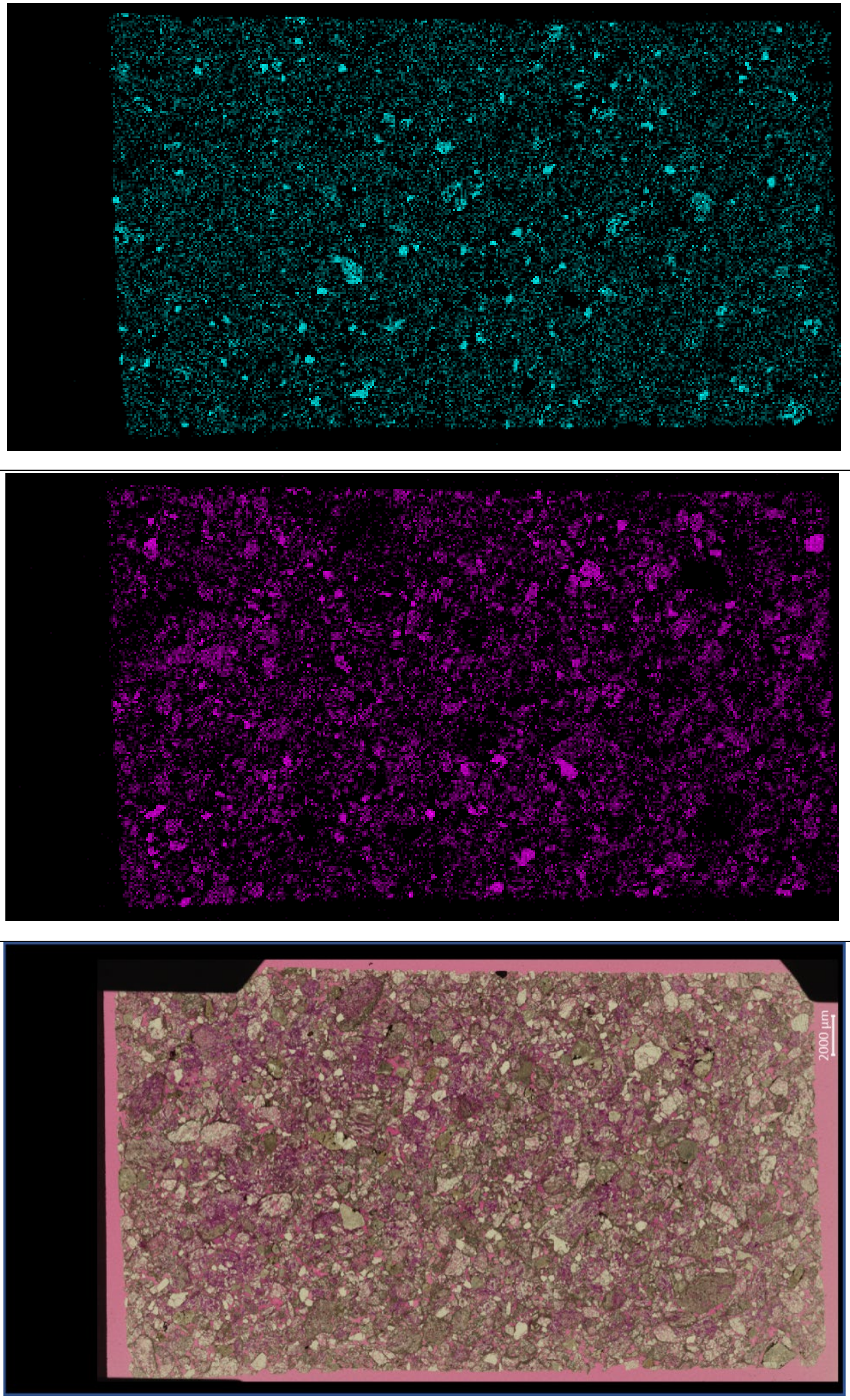

Figure 32. Quartz/amorphous opal and feldspar phases from X-ray fluorescence principal component analysis (see Figure 31 for details) next to a plane light photomicrograph mosaic for thin section GI-4-35 (VNT-3) for comparison.

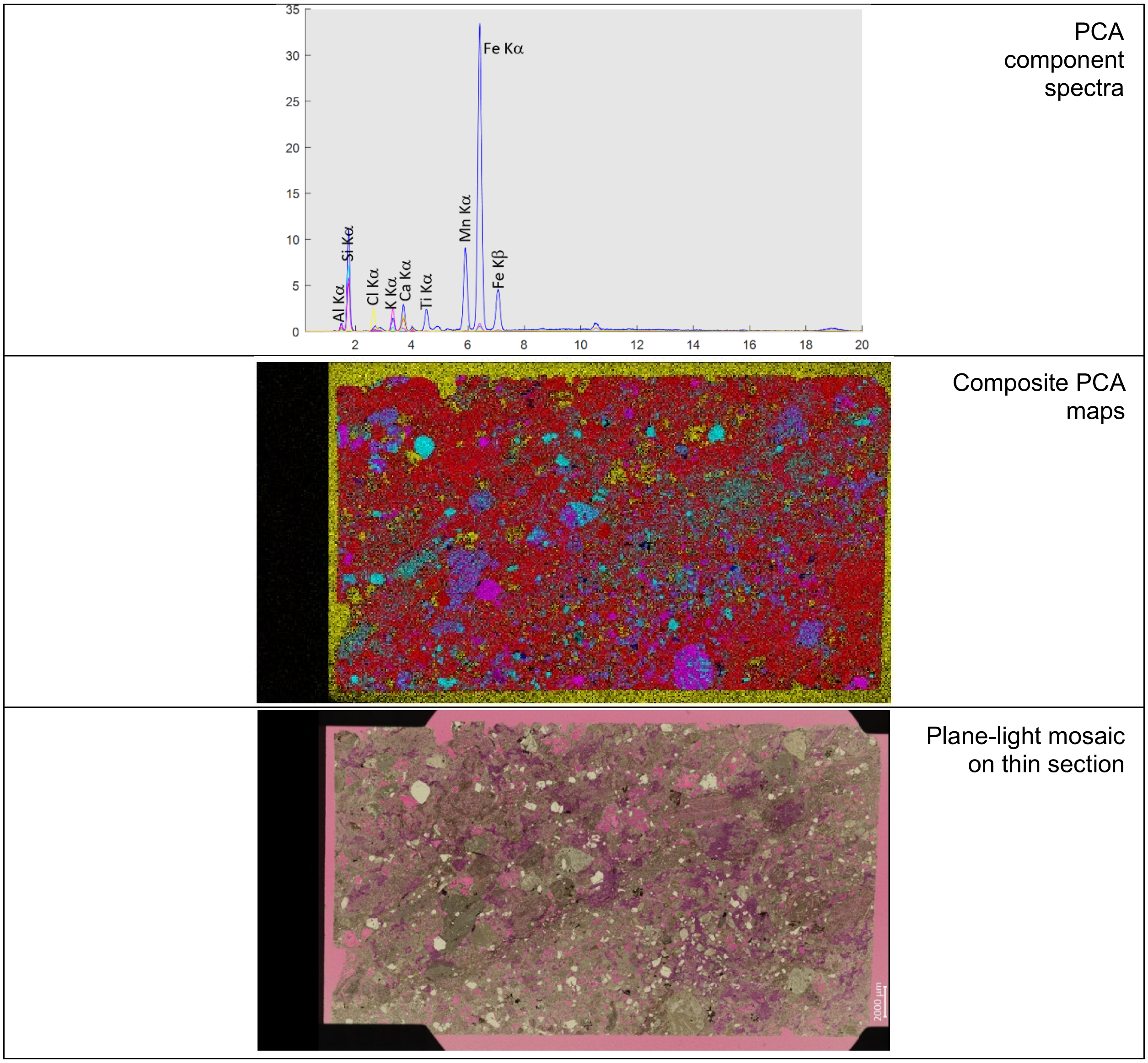

Figure 33. A subset of spectra based on principal component analysis (PCA) and multivariate statistical analysis on X-ray fluorescence analysis on thin section GI-4-49 (VNT-4), the spatial rendering of the PCA-identified phases, and a plane-light photomicrograph mosaic. The y-axis of the spectra plot is normalized counts such that, for a particular chemical phase, the product of the normalized counts and the intensity of the corresponding component image (not shown) results in counts equivalent to the original X-ray counts. The x-axis is X-ray energy (kV). The color intensity of a given image is proportional to the concentration of the chemical phase.

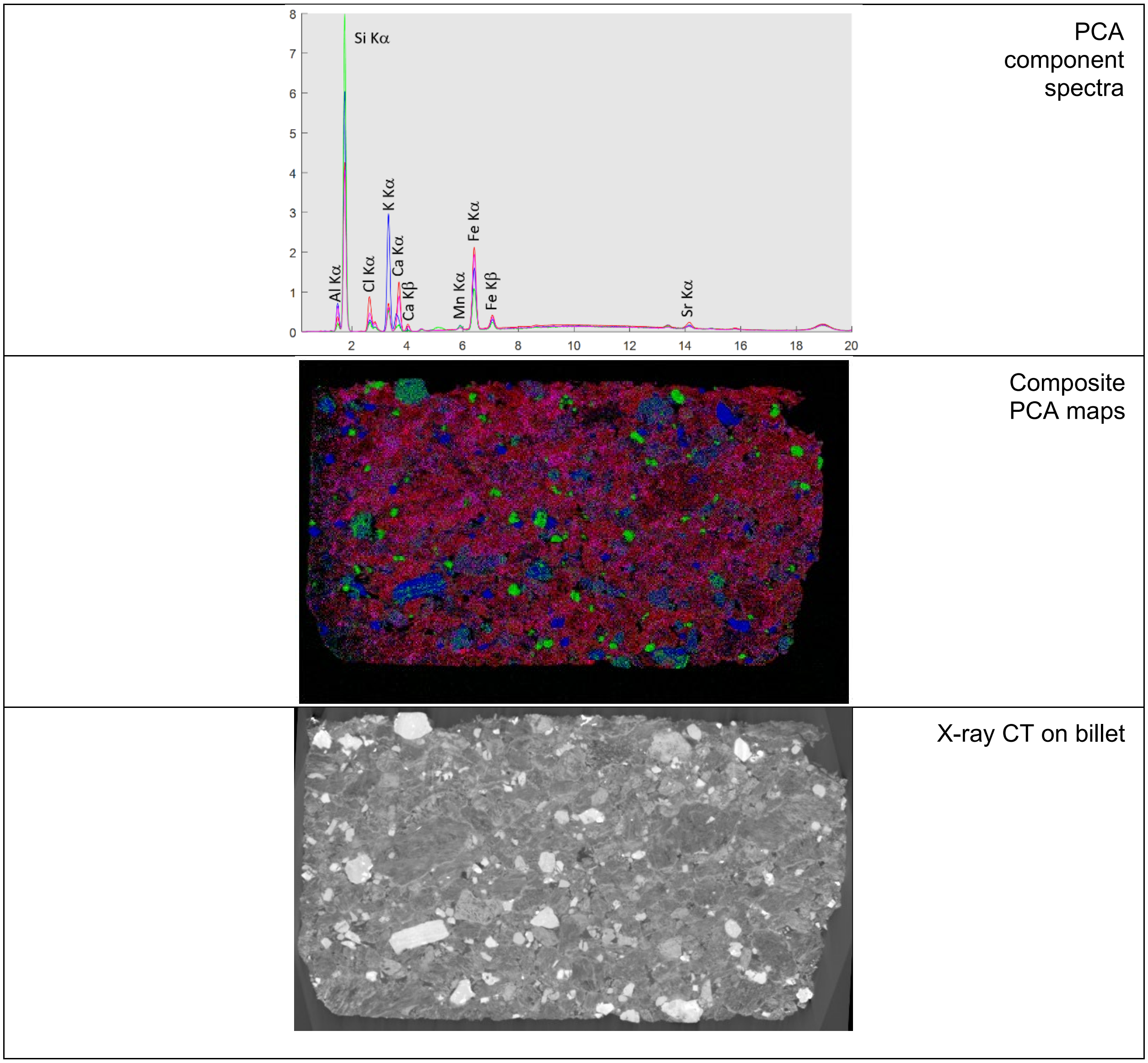

Figure 34. A subset of spectra based on principal component analysis (PCA) and multivariate statistical analysis on X-ray fluorescence analysis on billet GI-4-54 (VNT-4), the spatial rendering of the PCA-identified phases, and an image from X-ray computed tomography. The y-axis of the spectra plot is normalized counts such that, for a particular chemical phase, the product of the normalized counts and the intensity of the corresponding component image (not shown) results in counts equivalent to the original X-ray counts. The x-axis is X-ray energy (kV). The color intensity of a given image is proportional to the concentration of the chemical phase. The xy area is approximately that of a standard thin section (27 mm × 46 mm).

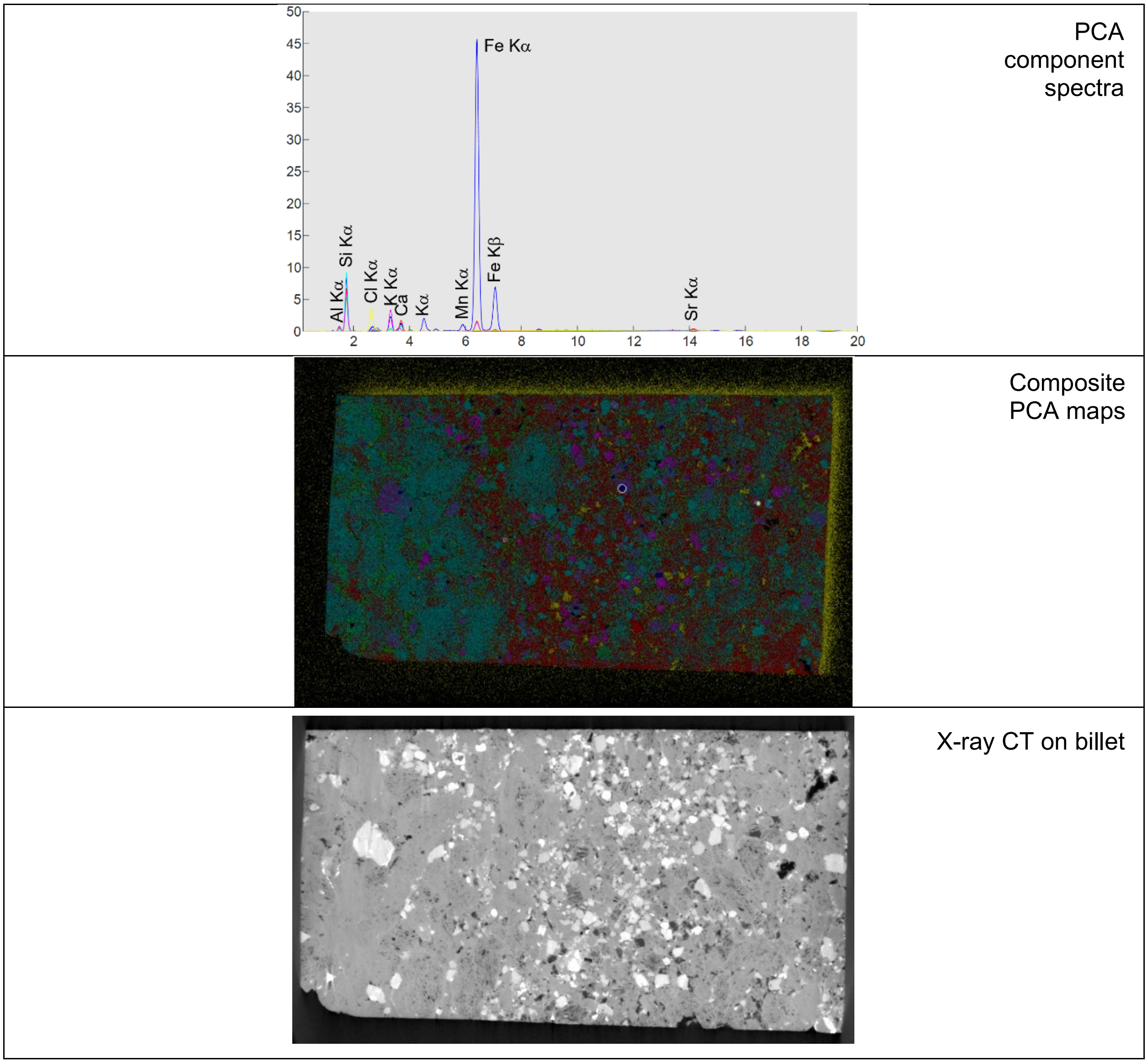

Figure 35. A subset of spectra based on principal component analysis (PCA) and multivariate statistical analysis on X-ray fluorescence analysis on billet GI-4-72 (VNT-5), the spatial rendering of the PCA-identified phases, and an image from X-ray computed tomography. The y-axis of the spectra plot is normalized counts such that, for a particular chemical phase, the product of the normalized counts and the intensity of the corresponding component image (not shown) results in counts equivalent to the original X-ray counts. The x-axis is X-ray energy (kV). The color intensity of a given image is proportional to the concentration of the chemical phase. The xy area is approximately that of a standard thin section (27 mm × 46 mm).

3.2.5. X-ray Computed Tomography

Two of the 18 billets (see Section 3.2.1) were scanned by X-ray CT with a Zeiss Xradia 620 Versa. These two billets were chosen for comparison between vitric and zeolitized samples. Data were collected on a flat panel detector with 21- or 23-μm voxel size over the entire billets, and data were also collected with a reduced field of view and higher resolution at 5.8 or 5.9 μm voxel size. Re-alignment and export of image stacks of the datasets were performed with Fiji ImageJ software (Schindelin et al., 2012). Air regions and artifact sections of the dataset were cropped out during that process.

Figure 36 through Figure 39 present 3D rendering using Avizo™ 3D 2021.2 software by Thermo Fisher Scientific of the full billets and the sub-volume scans, including 2D images at various orientations to give the reader a feel for the differences in the high and low resolution datasets in terms of resolvable features (e.g., the 21 and 23 μm datasets do not resolve many fine features visible in the 5.8 or 5.9 μm datasets).

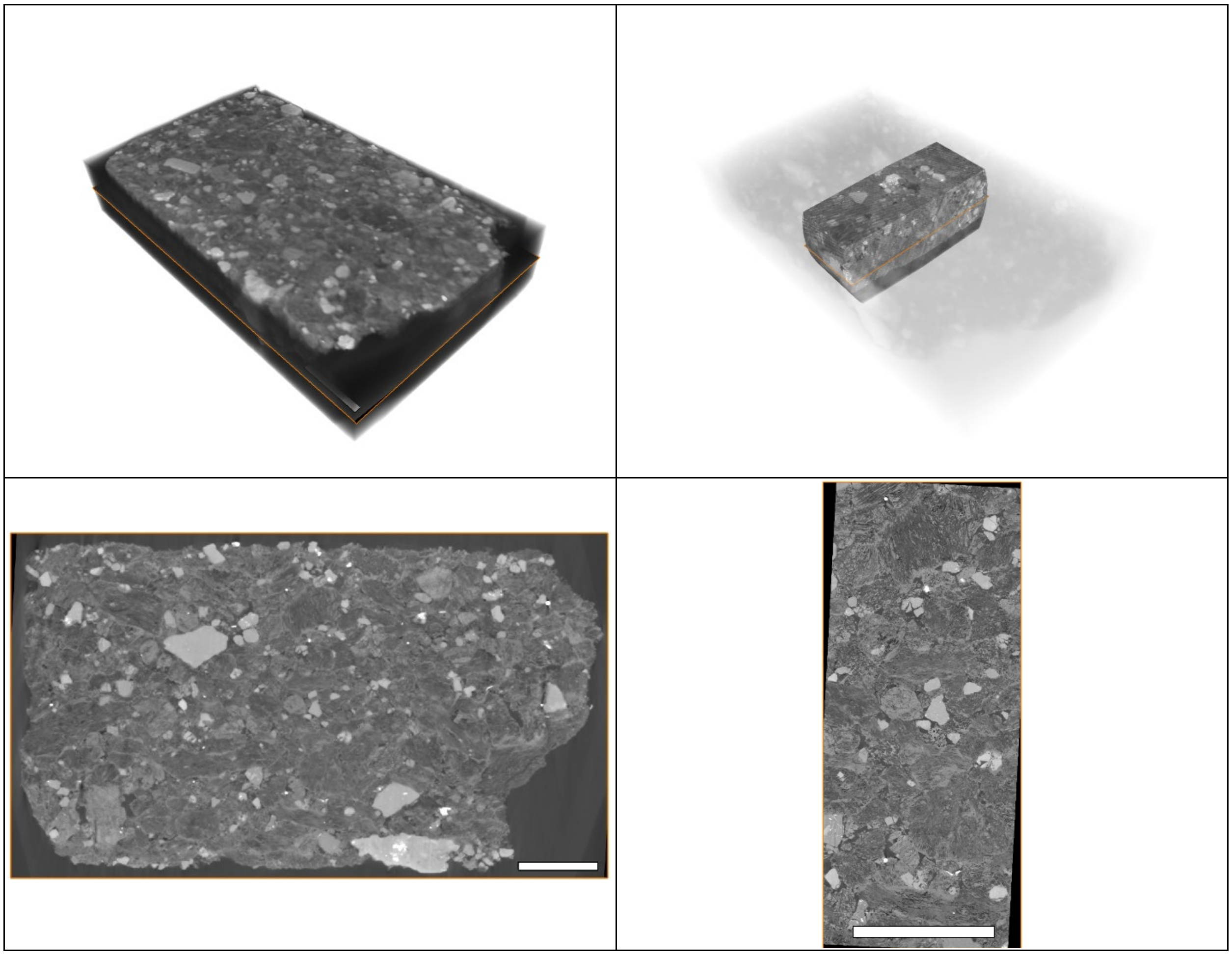

Figure 36. Overview of X-ray CT datasets obtained from billet GI-4-54 (VNT-4). (Upper left) 3D rendering of the 21-µm voxel resolution dataset taken over the entire billet with the darker grayscale values on the outer margins representing epoxy, and the top representing the polished upper surface of the billet. The plane highlighted in orange represents the image shown in the lower left. (Lower left) A 2D image from the 21-µm X-ray CT dataset, where the white scale bar is 5 mm. (Upper right) 3D rendering of the registered inset X-ray CT dataset collected at 5.8-µm voxel resolution—the surrounding billet of the 21-µm dataset has been made transparent. The plane highlighted in orange represents the image shown in the lower right. (Lower right) A 2D image from the 5.8-µm resolution X-ray CT dataset, where the white scale bar is 5 mm. Compare the middle portion of the lower left image to the image in the lower right as they represent the same location imaged at different resolutions.

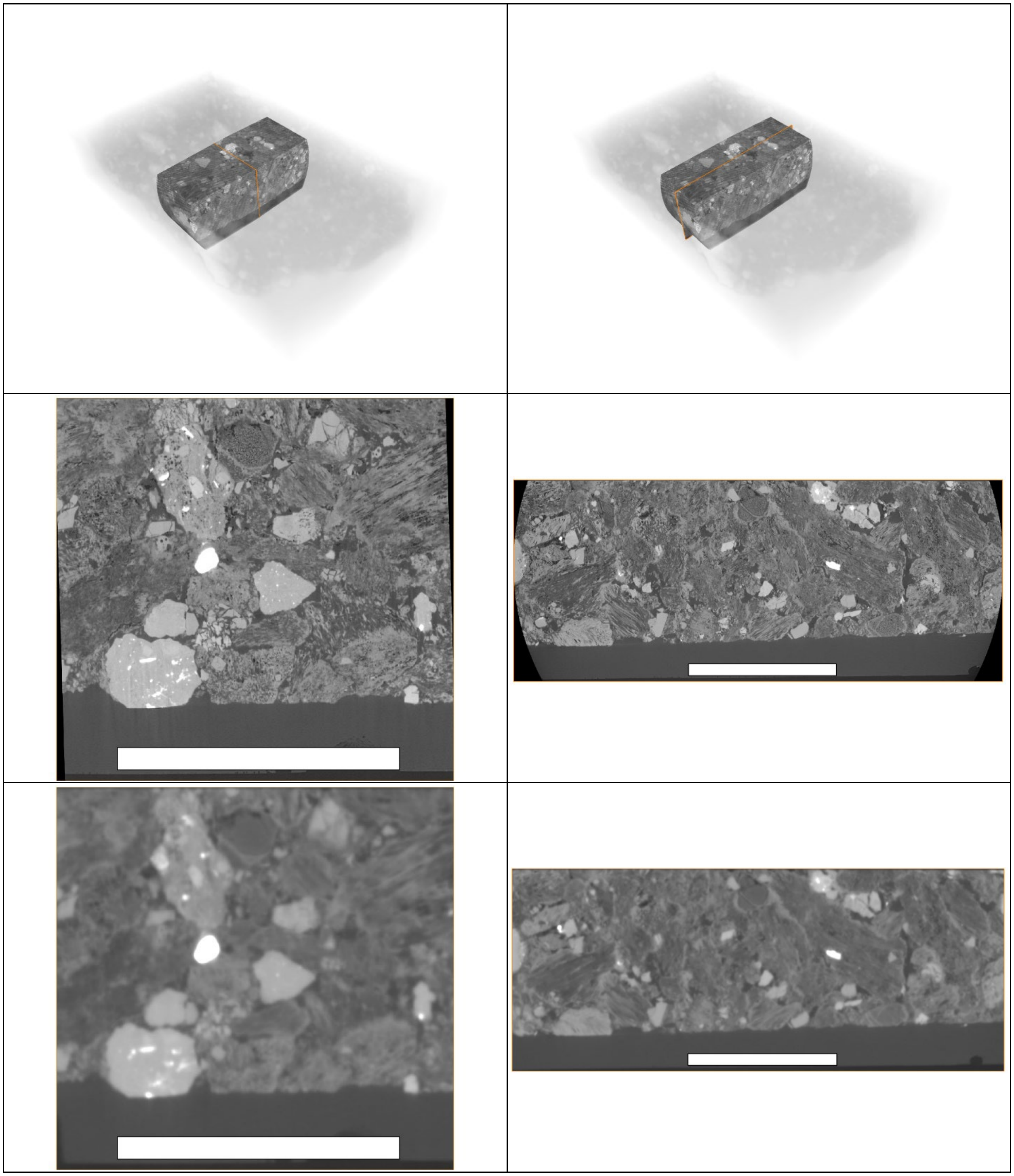

Figure 37. Comparison of the higher (5.8 μm) and lower (21 μm) resolution X-ray CT datasets on billet GI-4-54 (VNT-4) for the same planes. The scale bars represent 5 mm. Note the higher resolution dataset is in the shape of a cropped or truncated cylinder and thus has curved margins, but actual rock sample is not that shape. The first row shows where the planes are located, with the lower resolution dataset made transparent.

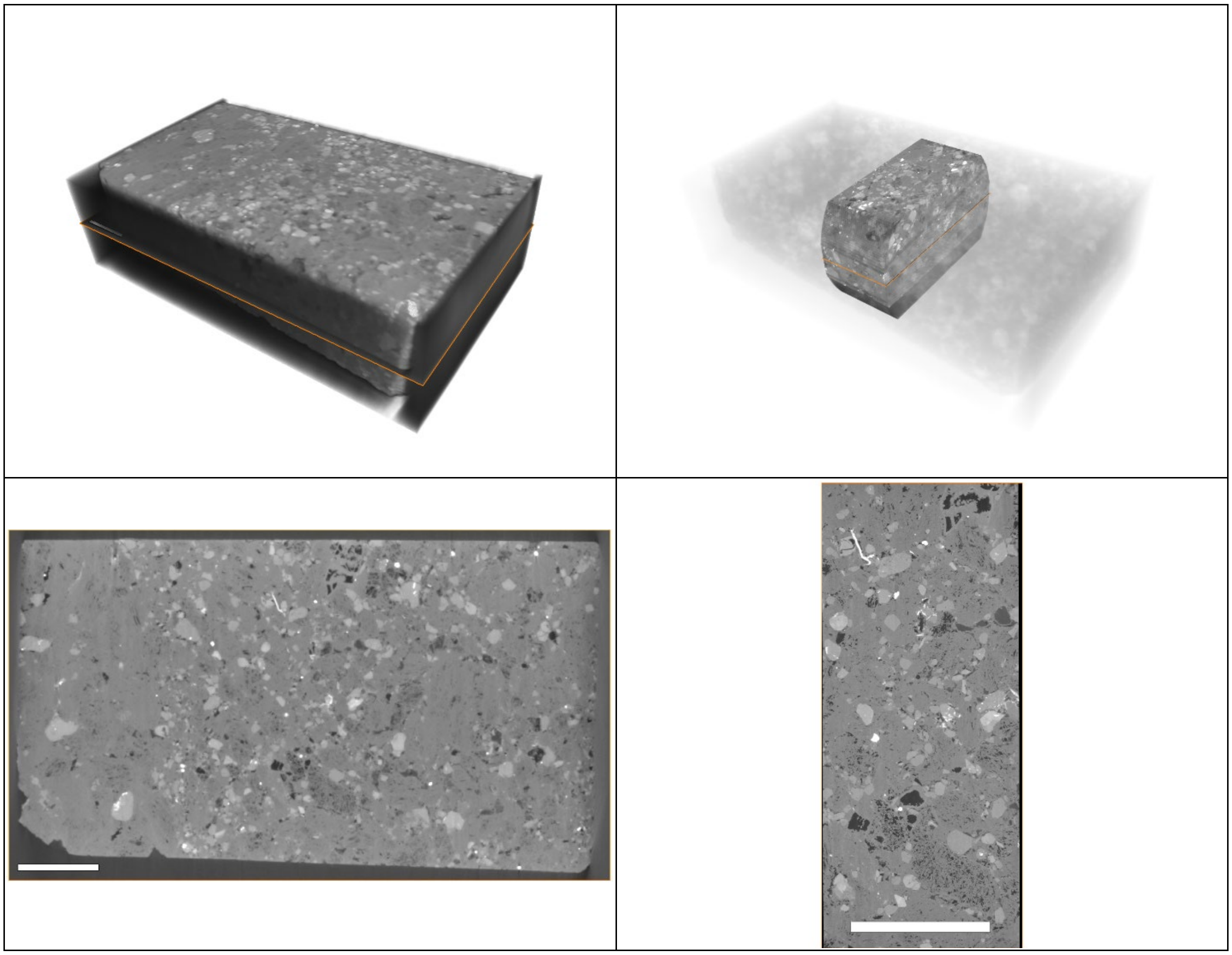

Figure 38. Overview of X-ray CT datasets obtained from billet GI-4-72 (VNT-5). (Upper left) 3D rendering of the 23-µm voxel resolution dataset taken over the entire billet with the darker grayscale values on the outer margins representing epoxy, and the top representing the polished upper surface of the billet. The plane highlighted in orange represents the image shown in the lower left. (Lower left) A 2D image from the 23-µm X-ray CT dataset, where the white scale bar is 5 mm. (Upper right) 3D rendering of the registered inset X-ray CT dataset collected at 5.9-µm voxel resolution—the surrounding billet of the 23-µm dataset has been made transparent. The plane highlighted in orange represents the image shown in the lower right. (Lower right) A 2D image from the 5.9-µm resolution X-ray CT dataset, where the white scale bar is 5 mm. Compare the middle portion of the lower left image to the image in the lower right as they represent the same location imaged at different resolutions.

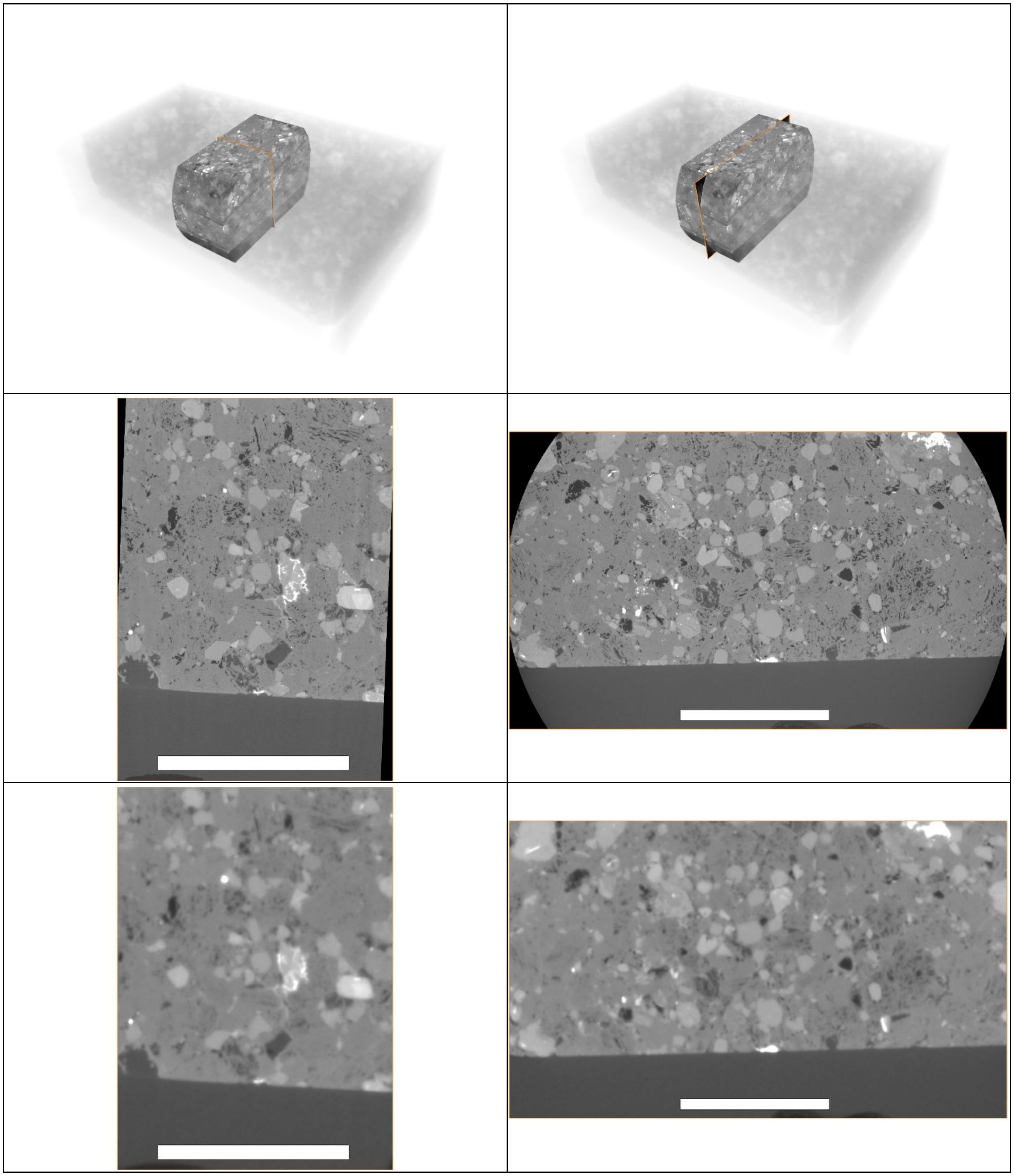

Figure 39. Comparison of the higher (5.9 µm) and lower (23 µm) resolution X-ray CT datasets on billet GI-4-72 (VNT-5) for the same planes. The scale bars represent 5 mm. Note the higher resolution dataset is in the shape of a cropped or truncated cylinder and thus has curved margins, but actual rock sample is not that shape. The first row shows where the planes are located, with the lower resolution dataset made transparent.

3.3. Hydrologic Laboratory Data

3.3.1. Capillary Pressure and Predicted Relative Permeability

Mercury intrusion capillary pressure (MICP) measurements, including an extrusion phase, were collected on a Micrometrics AutoPore IV 9500 Series porosimeter by CoreSpec Alliance, LLC. Samples were typically ~ 0.9-inch diameter × 0.9 inch long to fit into the penetrometer cup of the porosimeter, but some samples were irregular (Table 7). All eight samples were dried in a vacuum oven at 100°C for ~24 hours, and digital photos were taken. Samples were weighed and analyzed on the AutoPore IV and set to reach equilibrium by time (e.g., 30 seconds at both low and high pressure). Low-pressure intrusion proceeded to approximately 27 psia, after which the high-pressure intrusion commences, taking the pressure up to ~ 60,000 psia. The extrusion stage included monitoring volumes of mercury leaving the sample as pressure was returned to approximately atmospheric conditions. Data post-processing performed by CoreSpec Alliance, LLC, included corrections for "conformance," which is the volume of mercury that entered the penetrometer cup but did not actually intrude into the pore space of the samples. Other calculations performed were for wetting and non-wetting phase saturation, pore size distributions via the Washburn equation, and conversion to the air-water system using contact angle values. Note that testing for rock samples for GI-4-54 "ran over stem" for two of the four provided sub-samples (see Table 7), meaning that all the available mercury in the stem was intruded into the sample before fully filling the available pore space. A third fresh sub-sample was tested, and the run completed—that is, the run totally filled all the pores—before utilizing all the available mercury in the stem. This third GI-4-54 sample had a MICP-based porosity value of 50.41%. Data for the GI-4-54 sub-samples that ran over stem are not plotted in this report.

Figure 40 through Figure 49 present a summary of ranges in pore sizes for the eight MICP samples, a plot of MICP-calculated permeability to porosity, and plots of individual pore size distributions and mercury saturation versus pore size. Note that some saturation curves may show a "jag" at the crossover point between low- and high-pressure intrusion of ~ 27 psia (which corresponds to a pore size of ~ 4 μm), which should be considered when interpreting the intrusion and pore size distribution data as the jags are an artifact. Table 8 presents MICP-analysis-derived rock properties including porosity, grain density, dry bulk density, median pore radius, calculated Swanson permeability (Swanson, 1981), and retained mercury saturation after the extrusion stage to ambient pressure. The very high porosity sample GI-4-54 has a correspondingly relatively lower dry bulk density of 1.13 g/cm^3, whereas other samples are typically closer to ~1.6 or 1.7 g/cm^3; one sample does reach the higher dry bulk density of 1.99 g/cm^3. For potential use in numerical modeling, mercury intrusion capillary pressure data can be converted to the air-water system (or other fluid pair systems) and fit with capillary pressure models, and such fits can also be used to estimate or predict relative permeability as a function of saturation (Heath et al., 2021). Furthermore, MICP data measured on samples from different locations or lithologies, as parameterized for ready comparison to each other, can help characterize heterogeneity in multiphase fluid flow properties. Thus, following methods of Heath et al. (2021), the MICP curves are converted to the air-water system using air-water-rock contact angles of 16.75° for the vitric samples and 17.52° for the zeolitized samples—these contact angle values are based on measurements on samples that were Argon ion milled (these data are not presented herein). Uni-modal and bi-modal van Genutchten (VG) model Markov chain Monte Carlo fits are presented in Figure 50 through Figure 57, including relative permeability predictions based on the VG fitting parameters for water and gas (Kuhlman et al., 2022).

Table 7. Descriptions including photos of samples used in mercury intrusion capillary pressure measurements.

Sample ID	Description	Sample Photos*
GI-2-6A	VNT-1 Vitric ash-fall tuff	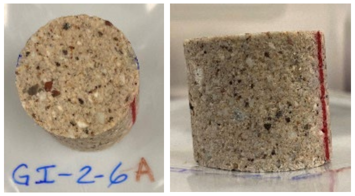
GI-2-6B	VNT-1 Vitric ash-fall tuff	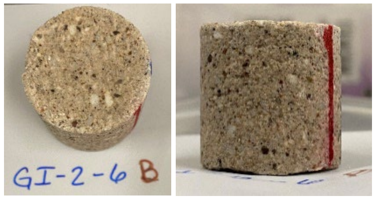
GI-3-2A	VNT-2 Vitric pumice-fall tuff	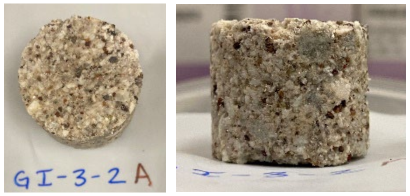
GI-3-2B	VNT-2 Vitric pumice-fall tuff	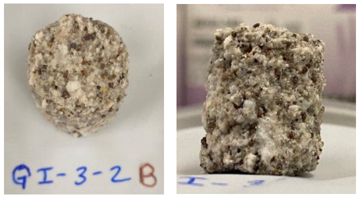
GI-3-21A	VNT-3 Vitric ash-fall tuff	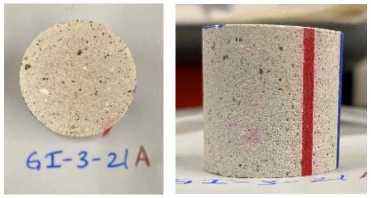

Sample ID	Description	Sample Photos*
GI-3-21B	VNT-3 Vitric ash-fall tuff	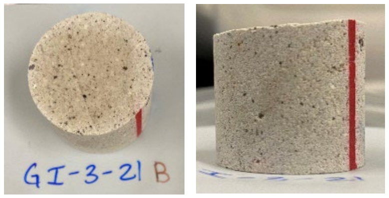
GI-4-18	VNT-3 Vitric ash-fall tuff with silica bands; plug has chip on one end	
GI-4-35	VNT-3 Vitric ash-fall tuff with abundant pumice and lithic fragments	
GI-4-43A	VNT-4 Zeolitized pumice-fall tuff	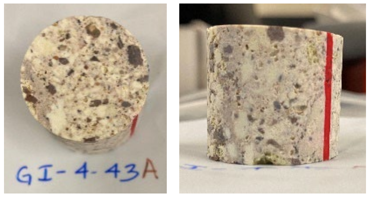
GI-4-43B	VNT-4 Zeolitized pumice-fall tuff	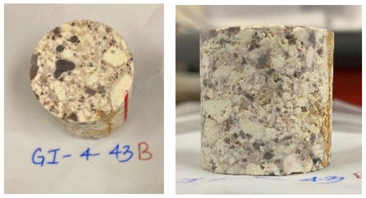

Sample ID	Description	Sample Photos*
GI-4-44	VNT-4 Zeolitized pumice-fall tuff with pumice and lithic fragments and localized silicification	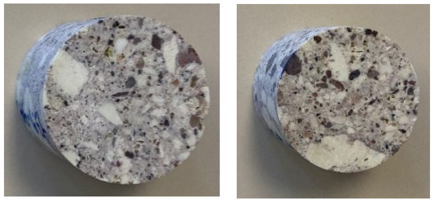
GI-4-54	VNT-4 Vitric pumice-fall tuff that is too friable to core or trim to plug geometry; four irregular samples provided	
GI-4-72	VNT-5 Zeolitized pumice-fall tuff with pumice, lithic fragments, and banding running parallel to plug axis	
DA-1-17	VNT-6 Vitric ash-fall tuff with fewer pumice and lithic fragments, less zeolite, and more smectite content than GI-4-35 ash-fall tuff	
DA-1-36	VNT-10 Zeolitized pumice-fall tuff with moderate zeolite and smectite content and prominent pore-lining opal	

Sample ID	Description	Sample Photos*
AC-1-111	UZNT Zeolitized ash-fall tuff with abundant pumice, zeolite, and moderate smectite content	

*Photos taken prior to shipping samples to the commercial laboratory

Table 8. Rock properties derived from the mercury intrusion capillary pressure tests and the retained mercury saturation after extrusion.

Sample ID	Lith. Unit	Porosity (%)	Grain Density (g/cm^3)	Bulk Density (g/cm^3)	Median Pore Radius (µm)	Smaller Pore Radius Mode (µm)	Larger Pore Radius Mode (µm)	Swanson Permeability to Air (mD)	Retained Mercury Saturation (fraction)*
GI-2-6A	VNT-1	30.2	2.21	1.54	2.123	0.002**	4.7	86.7	0.828
GI-2-6B	VNT-1	29.7	2.16	1.52	1.464	0.002**	4.3	63.2	0.814
GI-3-2A	VNT-2	31.8	2.27	1.55	2.541	0.006	2.8	131.7	0.858
GI-3-2B	VNT-2	32.7	2.30	1.55	2.7888	0.005	11.6	226.9	0.845
GI-3-21A	VNT-3	38.0	2.74	1.70	0.409	0.004**	2.6	36.8	0.752
GI-3-21B	VNT-3	32.7	2.22	1.50	0.373	0.004*	2.5	27.7	0.755
GI-4-18	VNT-3	23.84	2.14	1.63	0.115	0.009	2.3	3.4	0.669
GI-4-35	VNT-3	28.04	2.17	1.56	0.711	0.004	2.4	40.1	0.809
GI-4-43A	VNT-4	18.7	2.11	1.71	0.019	0.012	1.0	0.8	0.73
GI-4-43B	VNT-4	17.07	2.11	1.73	0.032	0.012	4.3	2.8	0.74
GI-4-44	VNT-4	17.07	2.14	1.77	0.013	0.009	1.2	0.8	0.721
GI-4-54	VNT-4	50.41	2.28	1.13	1.762	0.004	3.9	139.7	0.847
GI-4-72	VNT-5	20.69	2.15	1.71	0.035	0.011	0.93	2.1	0.766
DA-1-17	VNT-6	31.20	2.30	1.58	4.292	0.002	8.9	234.0	0.872
DA-1-36	VNT-10	16.08	2.37	1.99	0.198	0.023	4.3	8.8	0.773
AC-1-111	UZNT	27.62	2.28	1.65	0.061	0.016	0.2	0.3	0.67

*At ambient pressure at the completion of the extrusion stage; Lith. = lithologic.

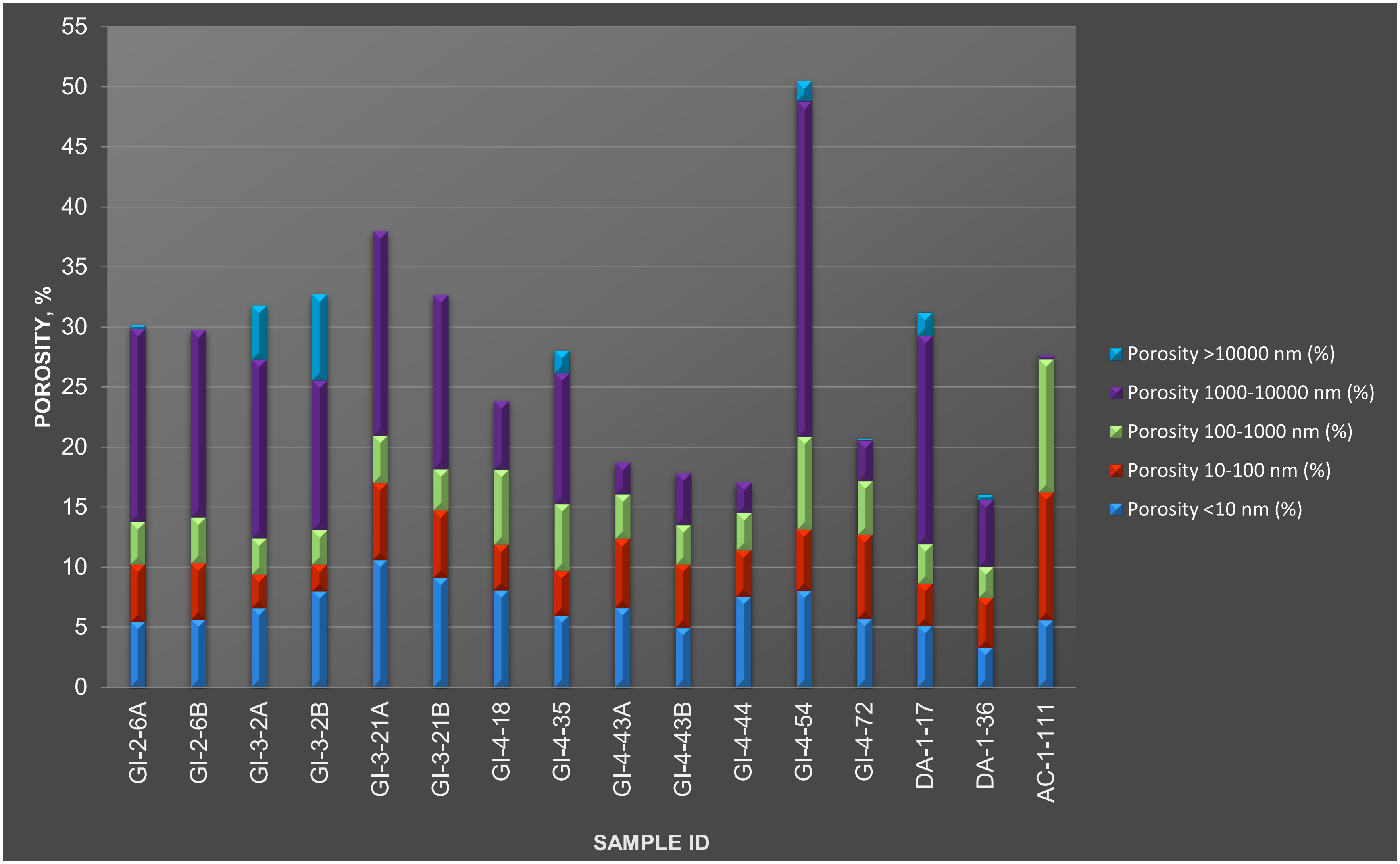

Figure 40. Summary of ranges in pore sizes based on MICP analysis.

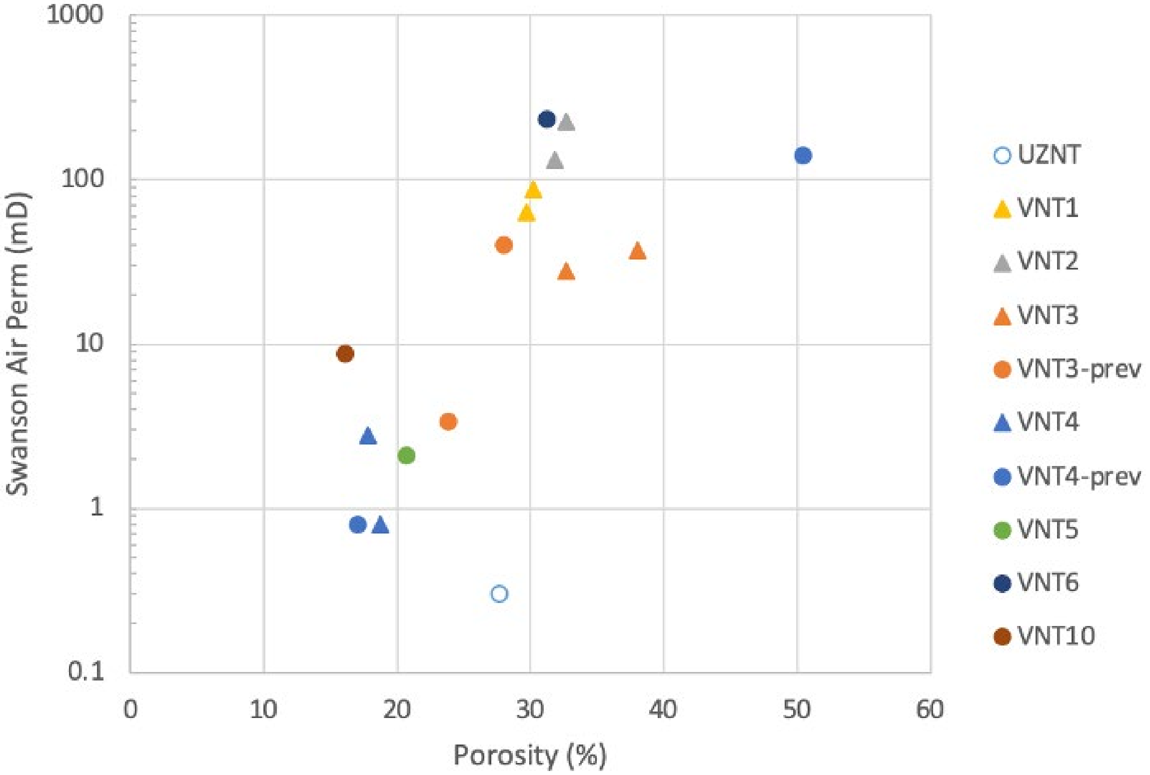

Figure 41. Plot of porosity and Swanson permeability based on mercury intrusion capillary pressure measurements.

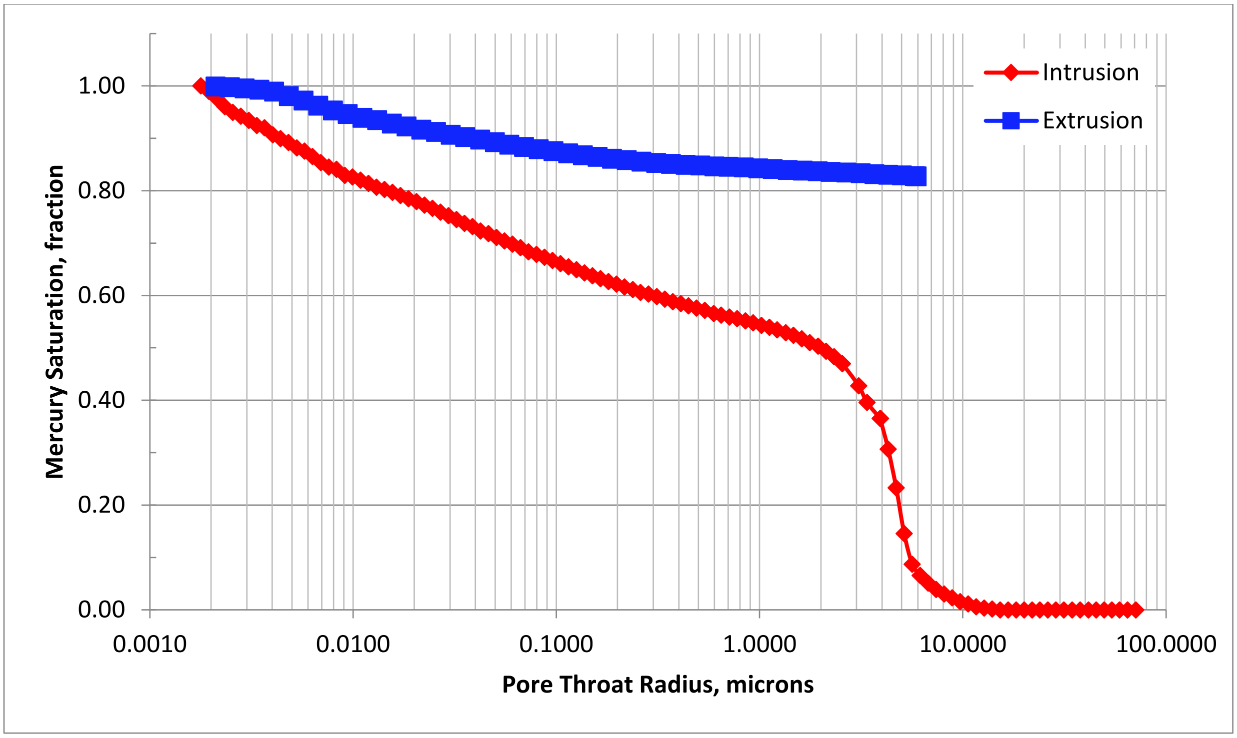

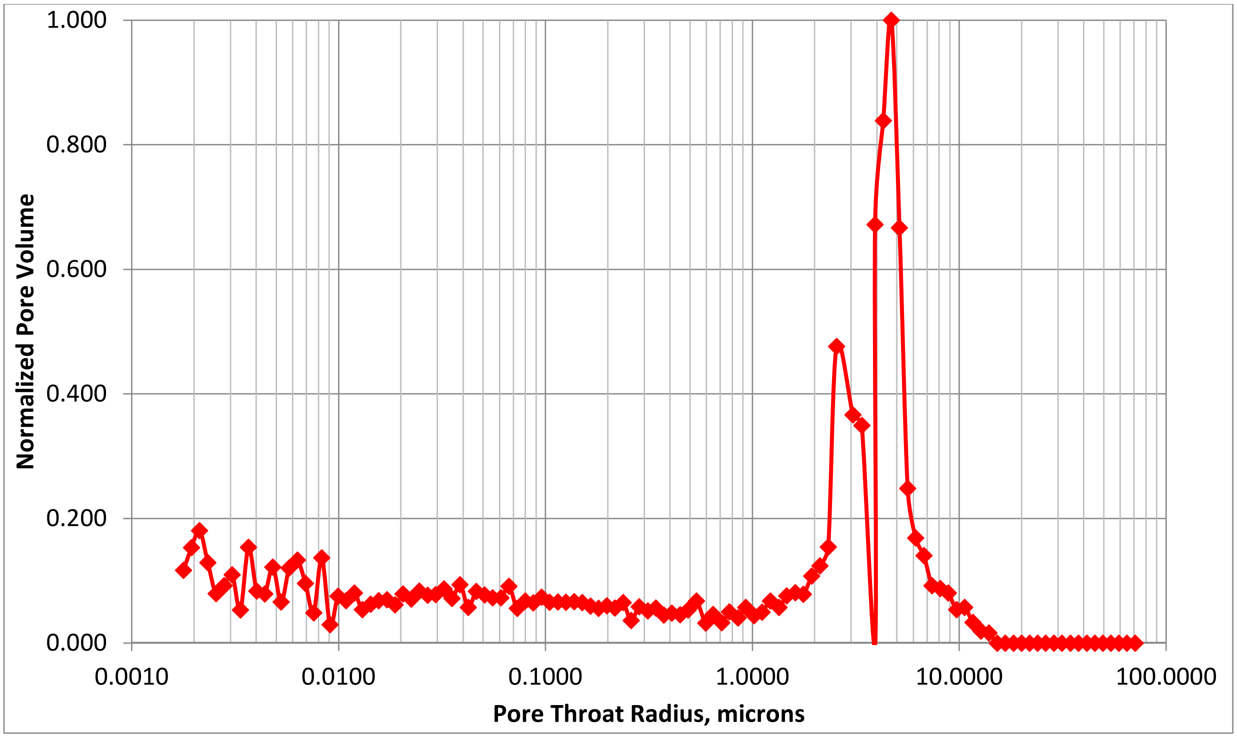

Figure 42. Mercury porosimetry results for sample MICP GI-2-6A (VNT-1). (Upper) Mercury intrusion (red) and extrusion (blue) plotted as mercury saturation as a function of pore size. (Lower) Pore size distribution based on intrusion data.

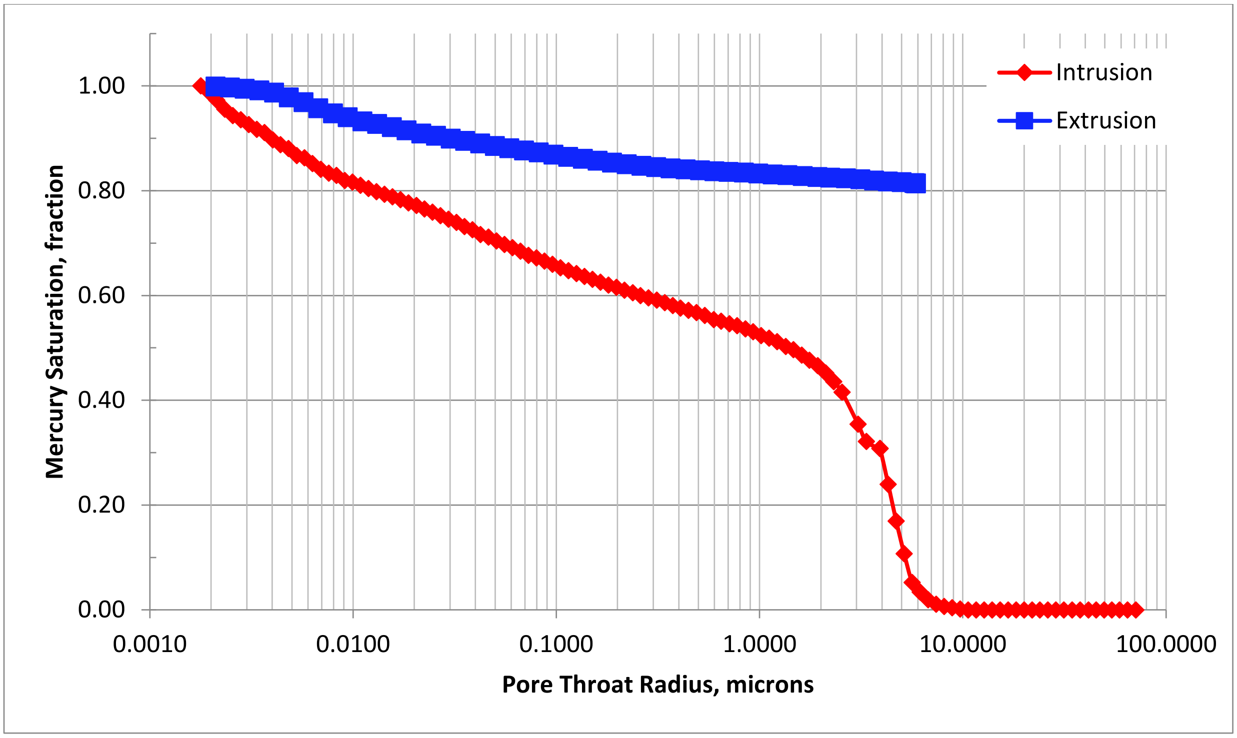

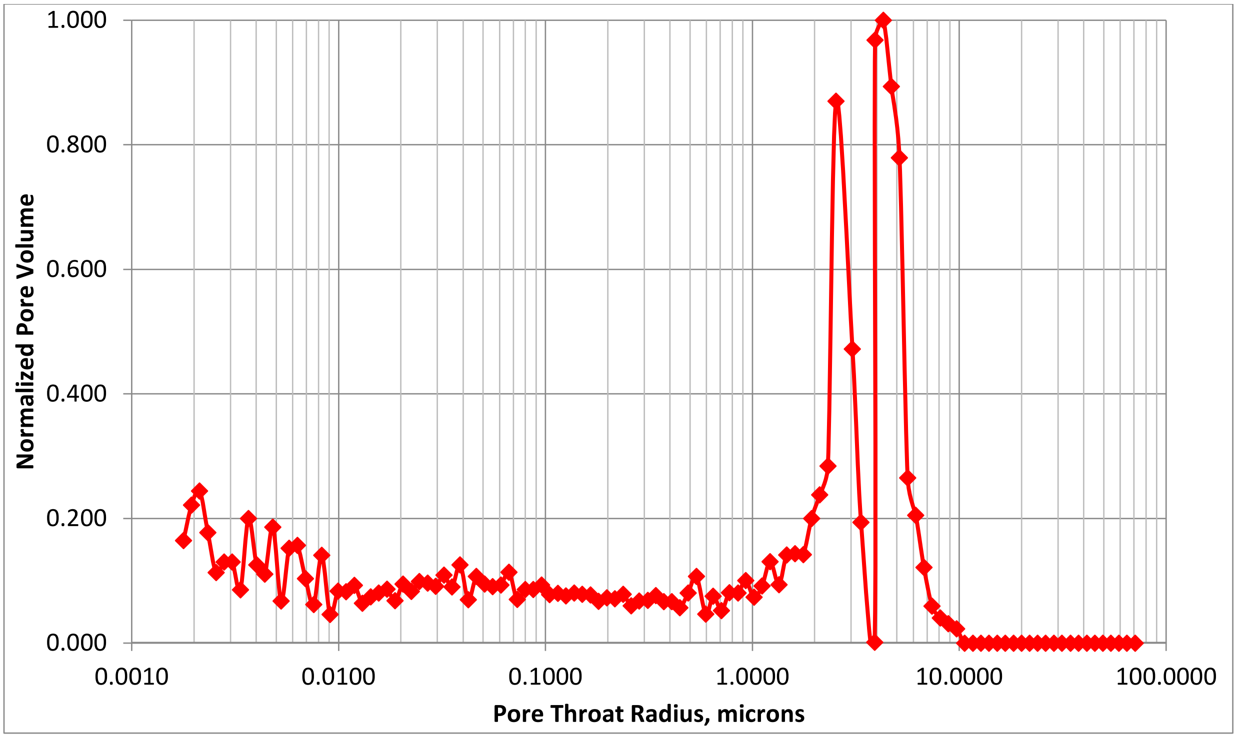

Figure 43. Mercury porosimetry results for sample MICP GI-2-6B (VNT-1). (Upper) Mercury intrusion (red) and extrusion (blue) plotted as mercury saturation as a function of pore size. (Lower) Pore size distribution based on intrusion data.

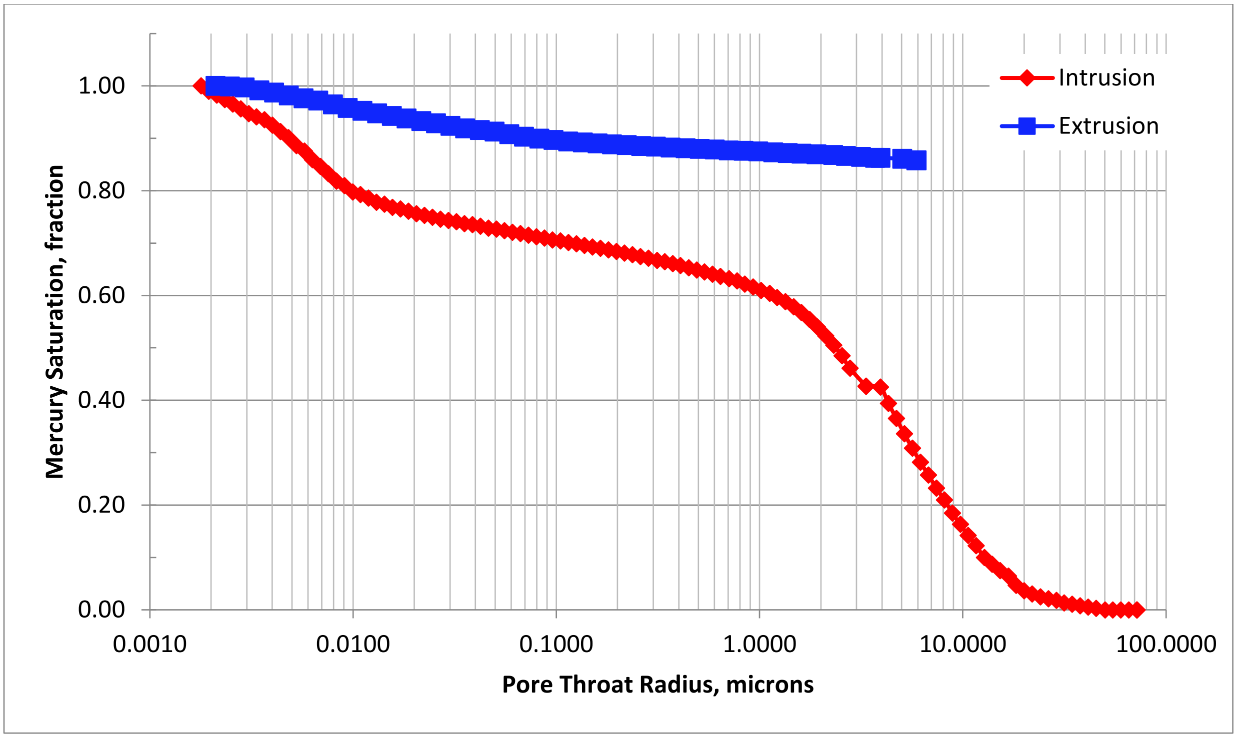

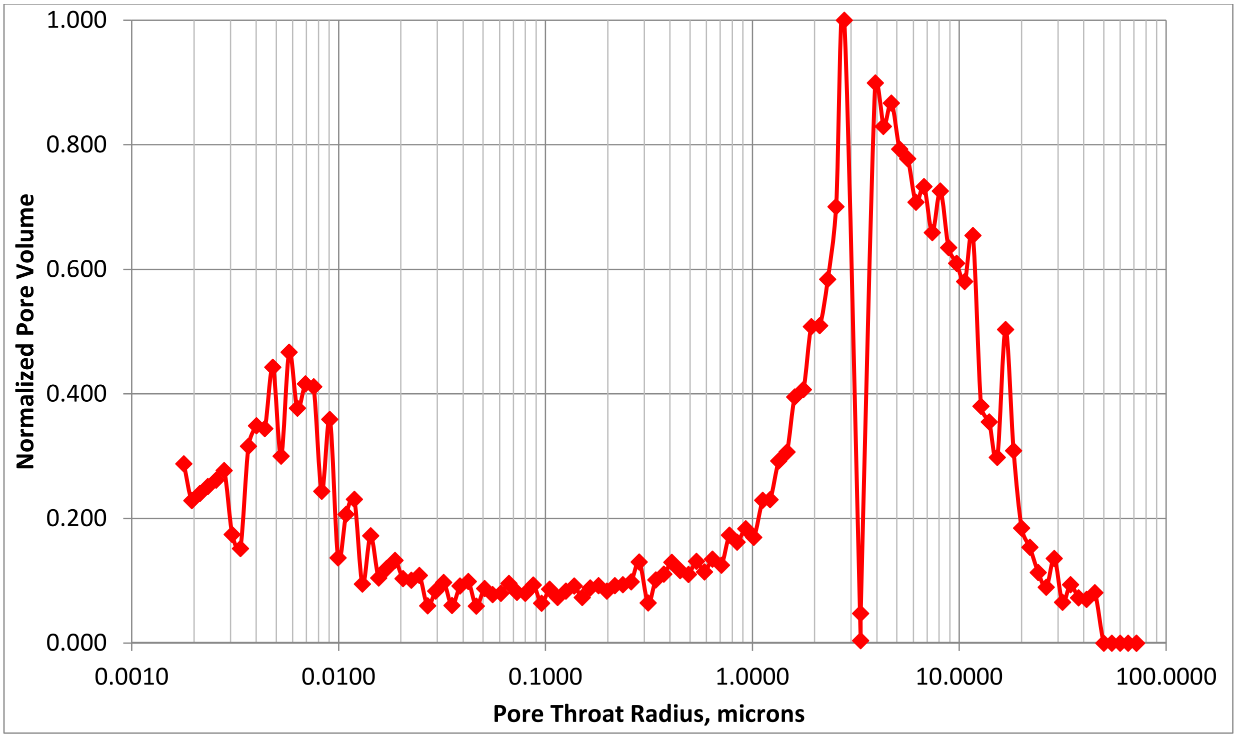

Figure 44. Mercury porosimetry results for sample MICP GI-3-2A (VNT-2). (Upper) Mercury intrusion (red) and extrusion (blue) plotted as mercury saturation as a function of pore size. (Lower) Pore size distribution based on intrusion data.

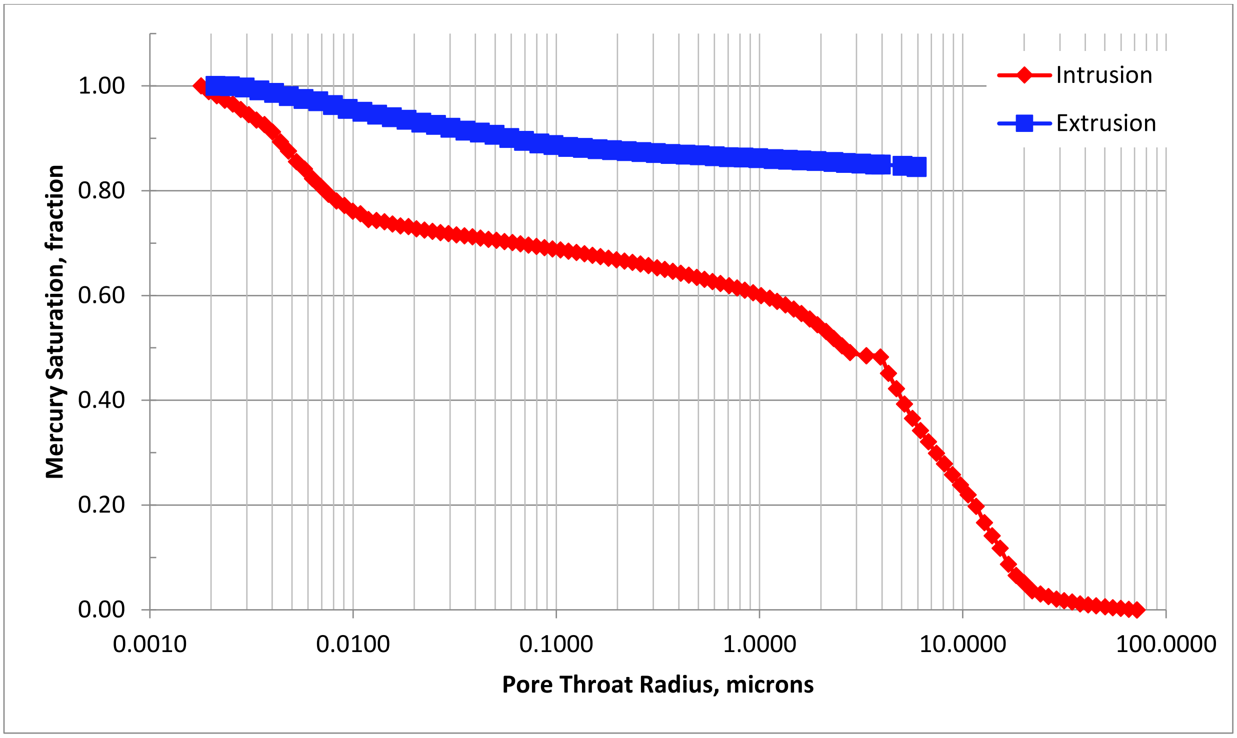

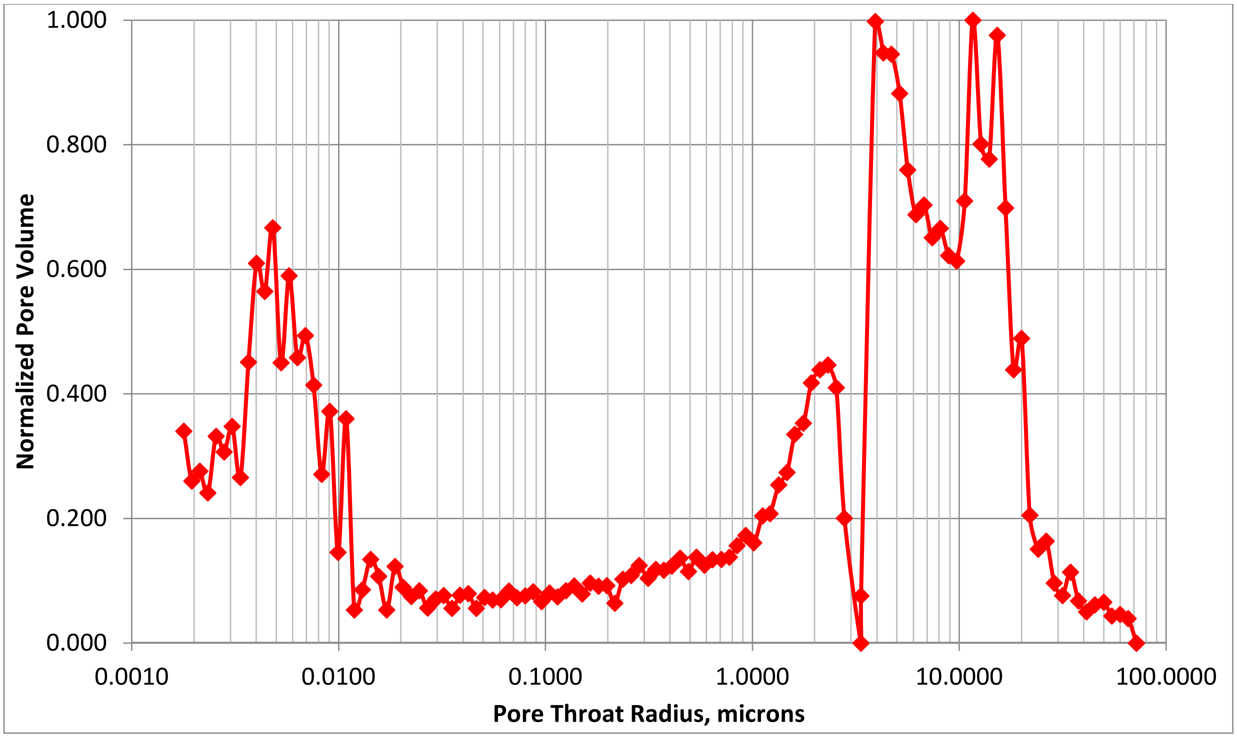

Figure 45. Mercury porosimetry results for sample MICP GI-3-2B (VNT-2). (Upper) Mercury intrusion (red) and extrusion (blue) plotted as mercury saturation as a function of pore size. (Lower) Pore size distribution based on intrusion data.

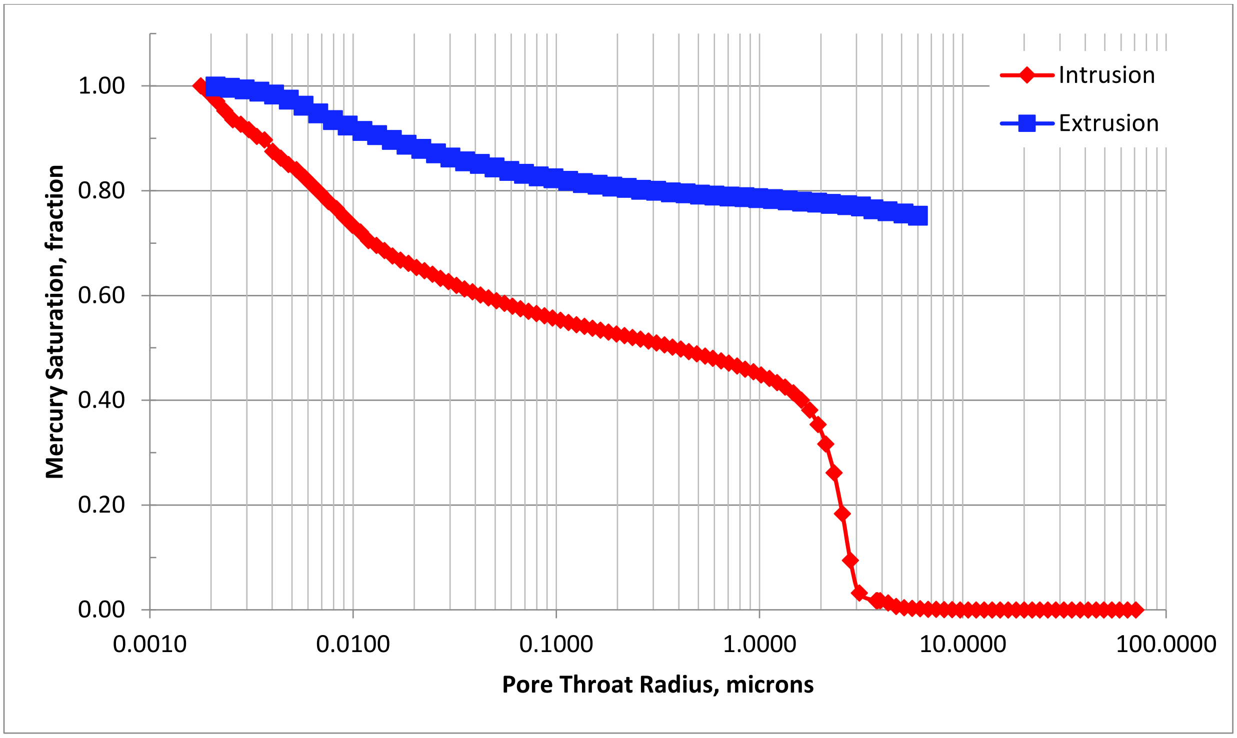

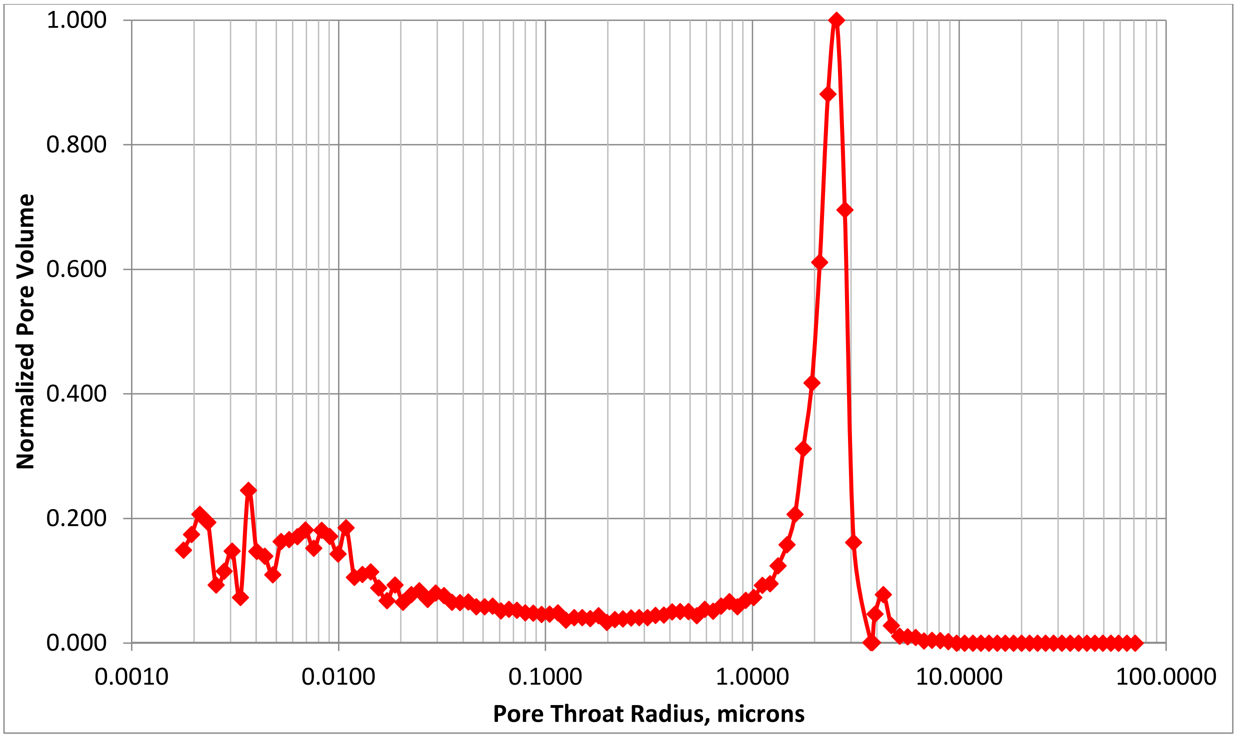

Figure 46. Mercury porosimetry results for sample MICP GI-3-21A (VNT-3). (Upper) Mercury intrusion (red) and extrusion (blue) plotted as mercury saturation as a function of pore size. (Lower) Pore size distribution based on intrusion data.

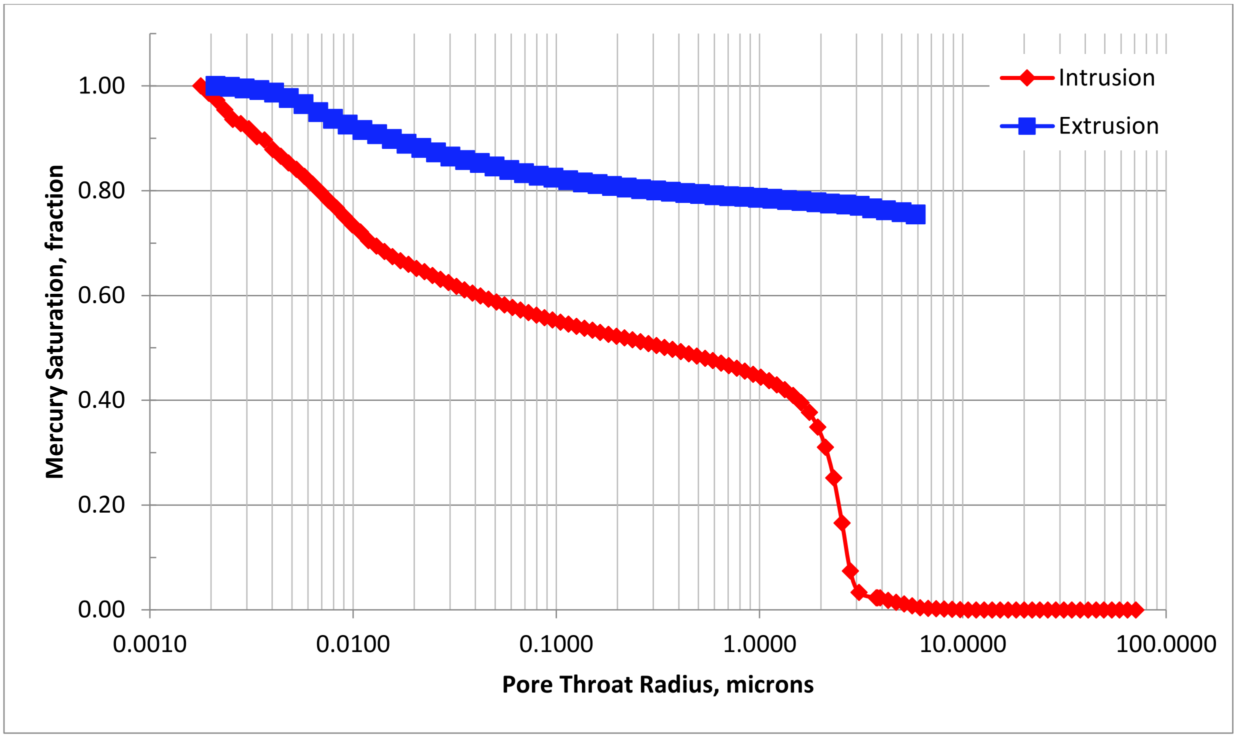

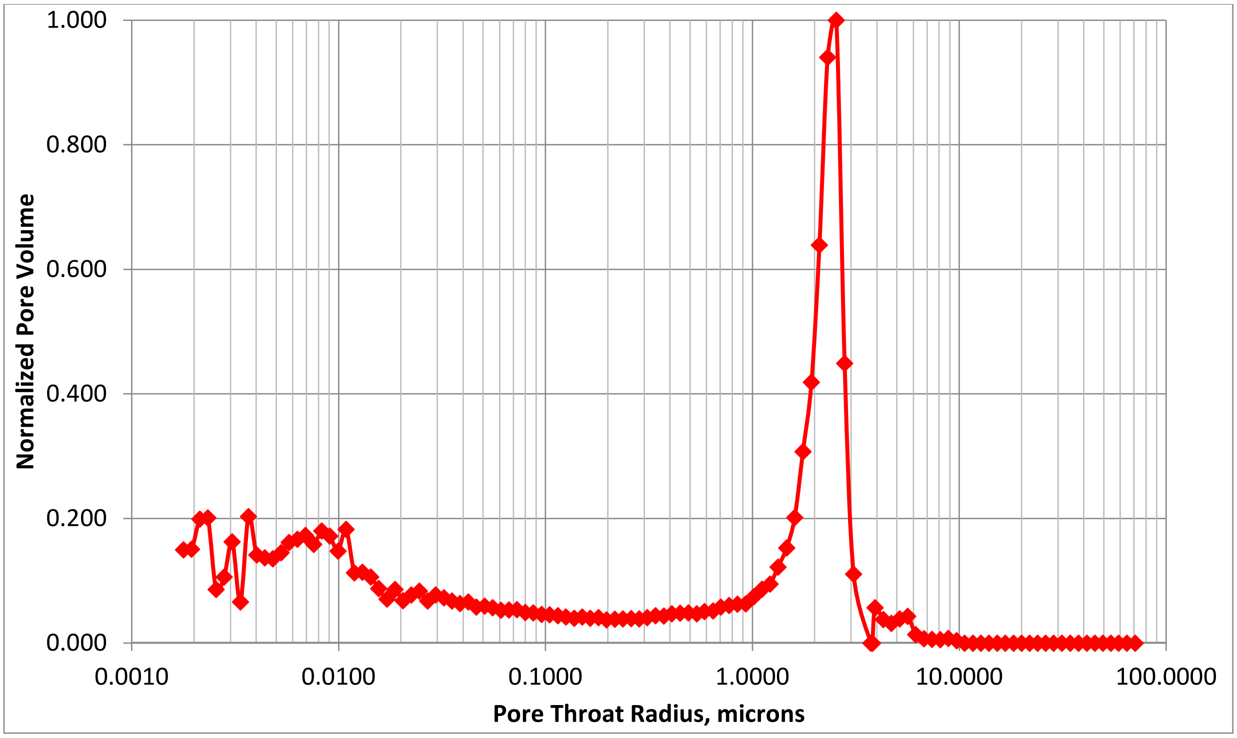

Figure 47. Mercury porosimetry results for sample MICP GI-3-21B (VNT-3). (Upper) Mercury intrusion (red) and extrusion (blue) plotted as mercury saturation as a function of pore size. (Lower) Pore size distribution based on intrusion data.

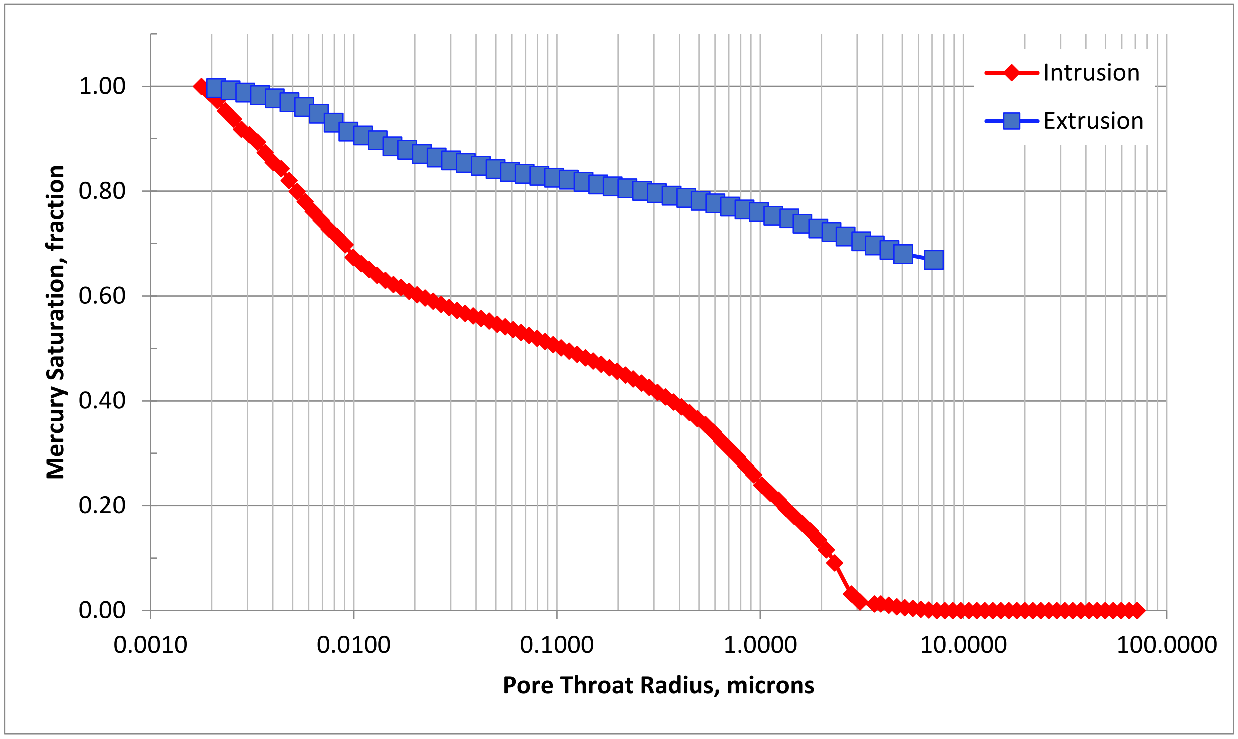

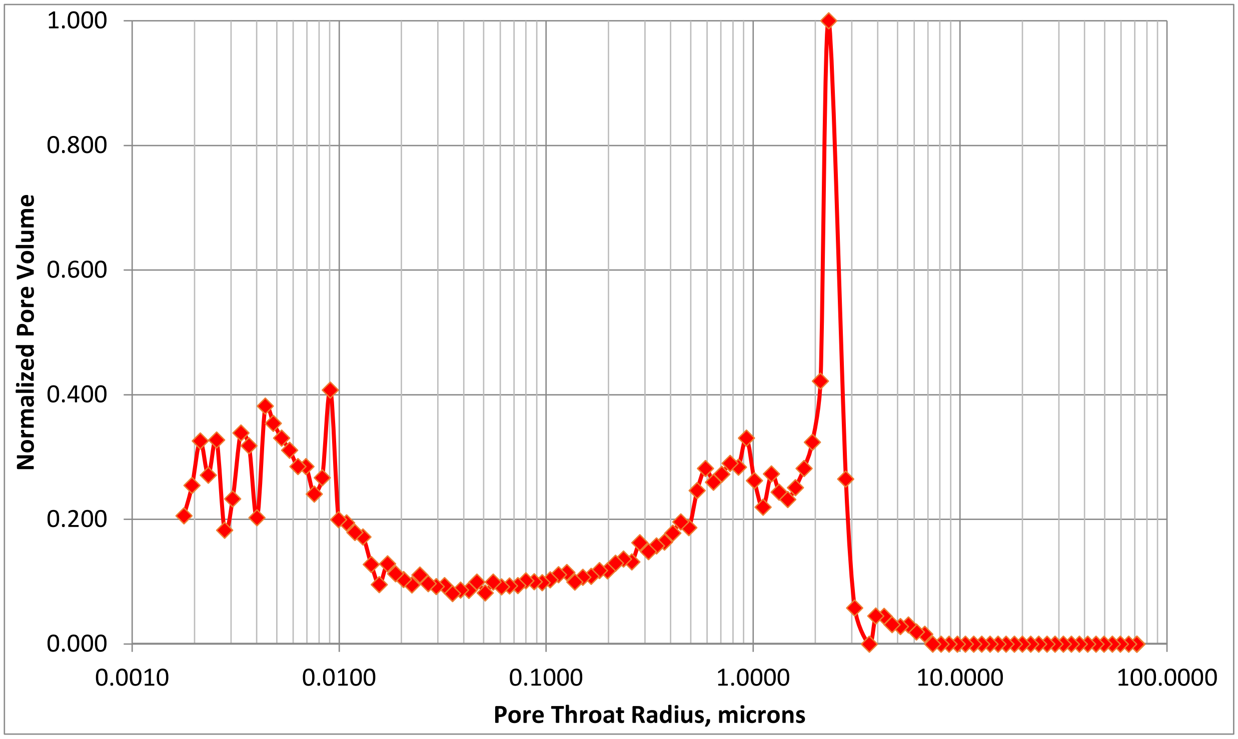

Figure 48. Mercury porosimetry results for sample MICP GI-4-18 (VNT-3). (Upper) Mercury intrusion (red) and extrusion (blue) plotted as mercury saturation as a function of pore size. (Lower) Pore size distribution based on intrusion data.

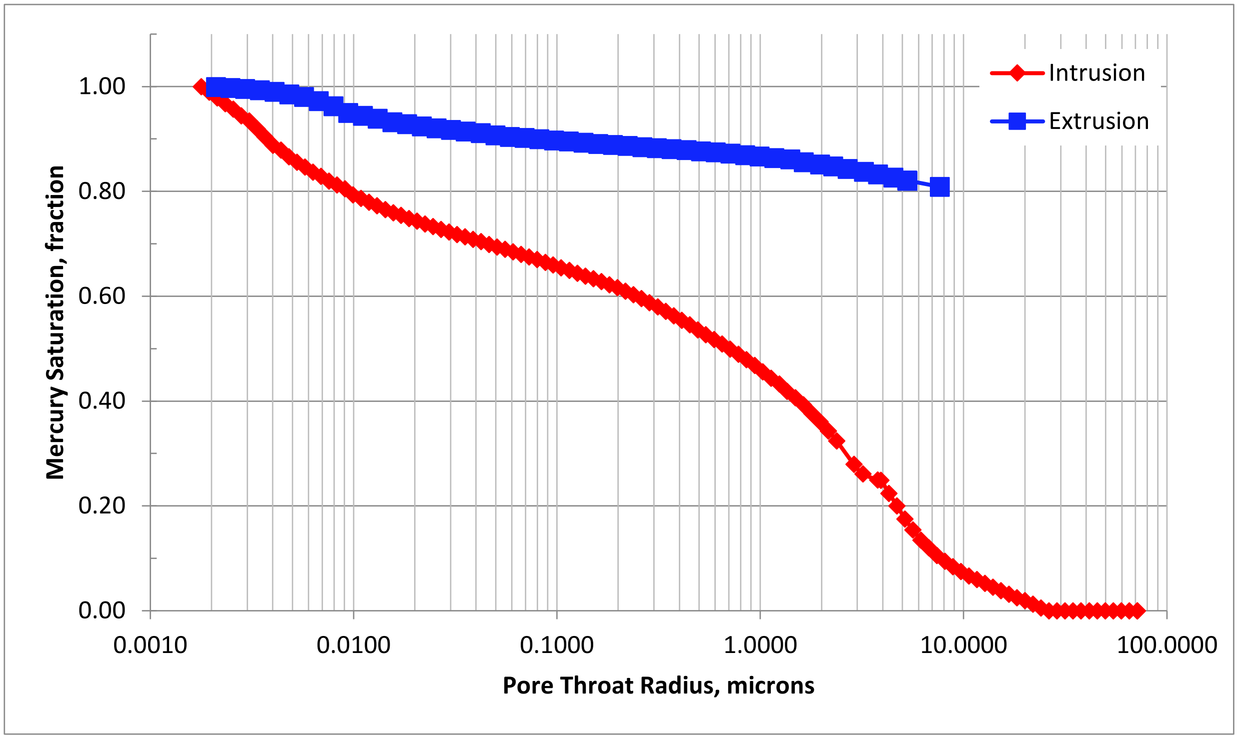

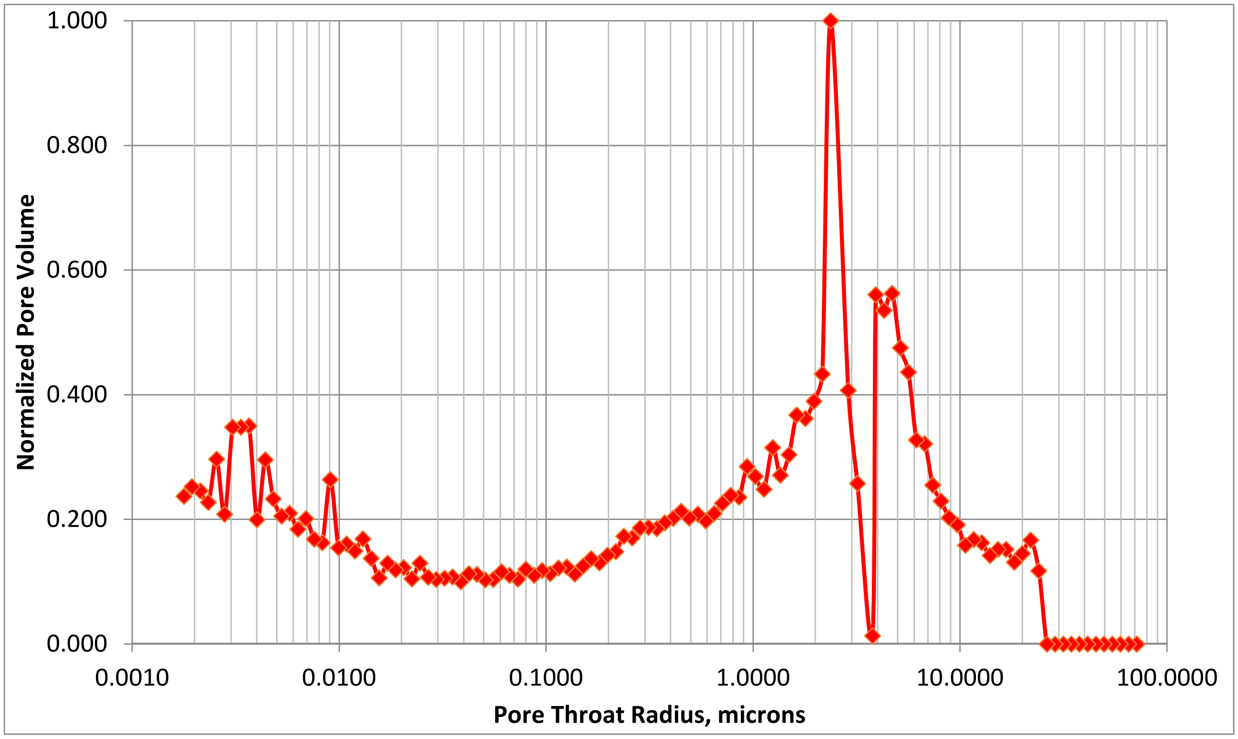

Figure 49. Mercury porosimetry results for sample MICP GI-4-35 (VNT-3). (Upper) Mercury intrusion (red) and extrusion (blue) plotted as mercury saturation as a function of pore size. (Lower) Pore size distribution based on intrusion data.

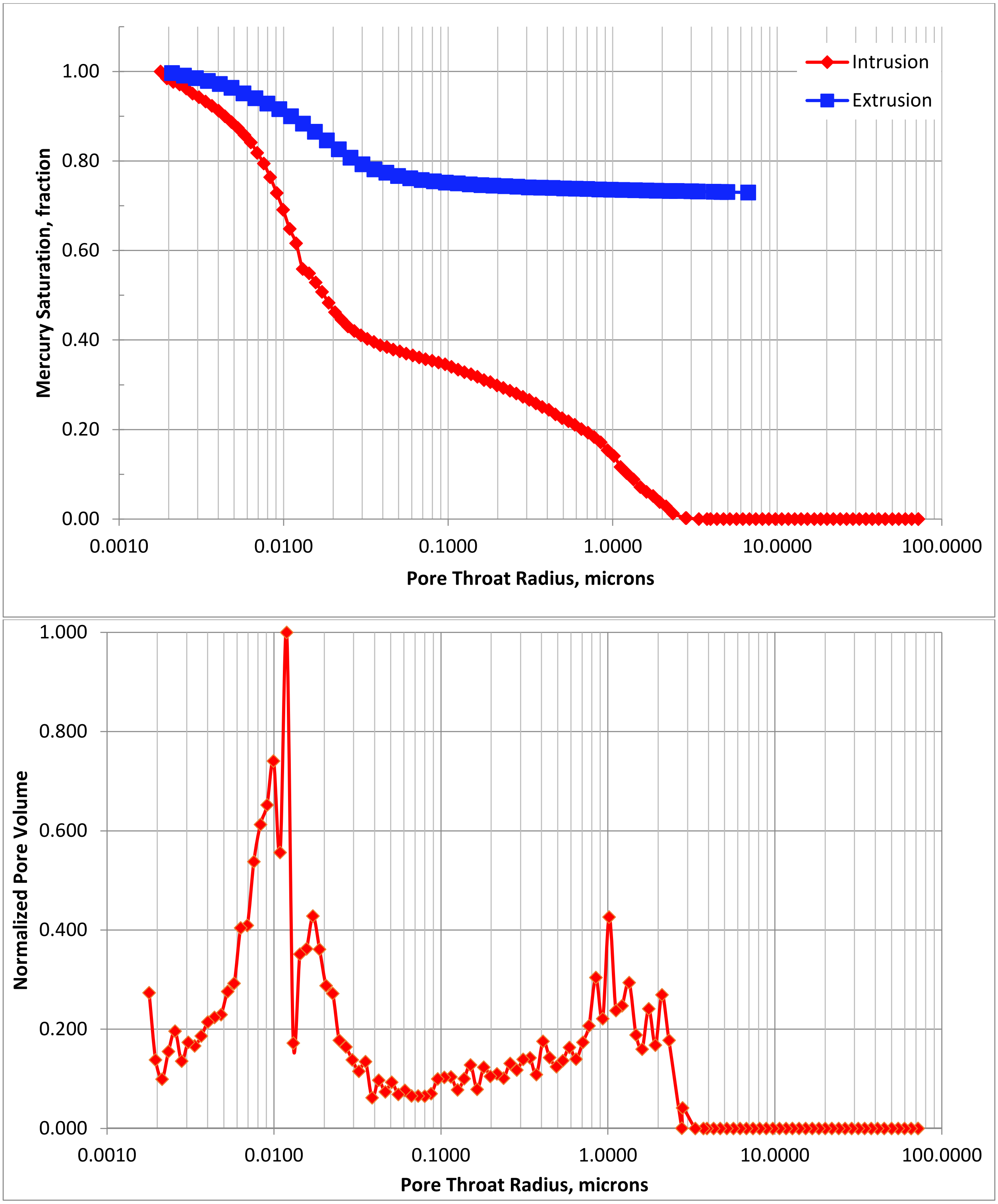

Figure 50. Mercury porosimetry results for sample MICP GI-4-43A (VNT-4). (Upper) Mercury intrusion (red) and extrusion (blue) plotted as mercury saturation as a function of pore size. (Lower) Pore size distribution based on intrusion data.

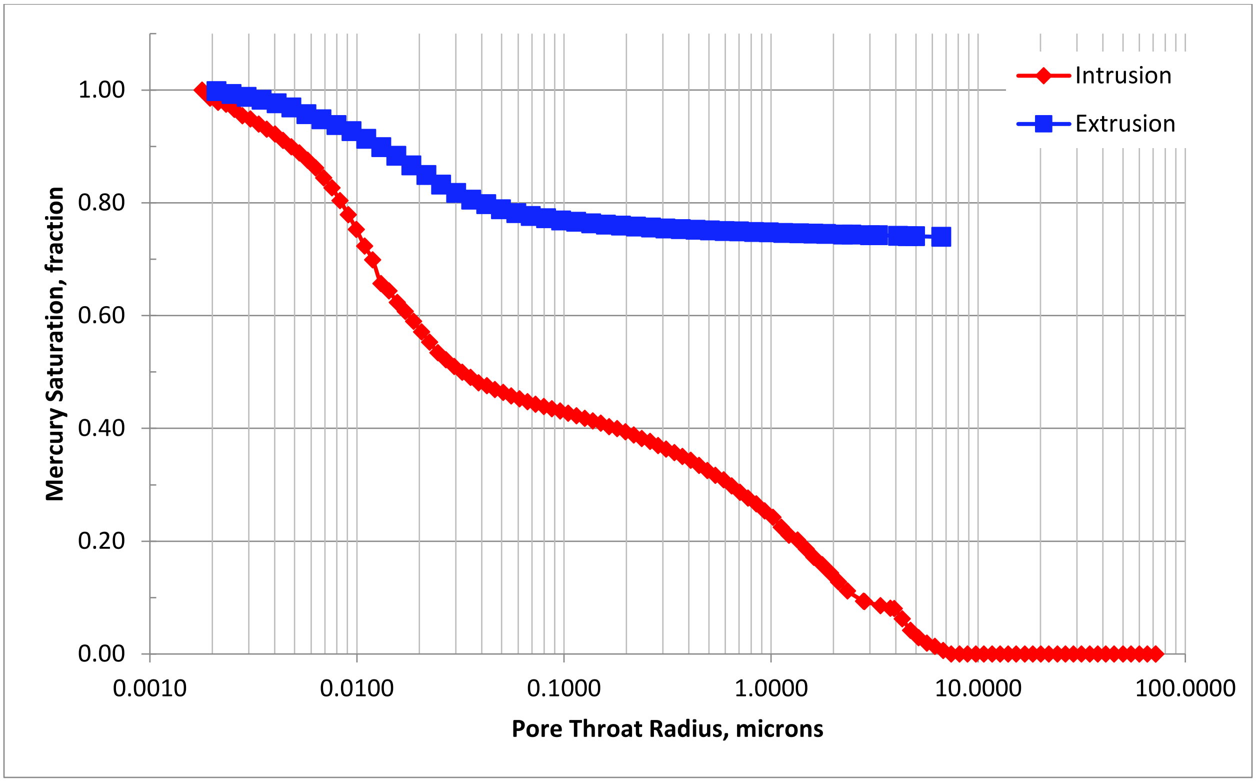

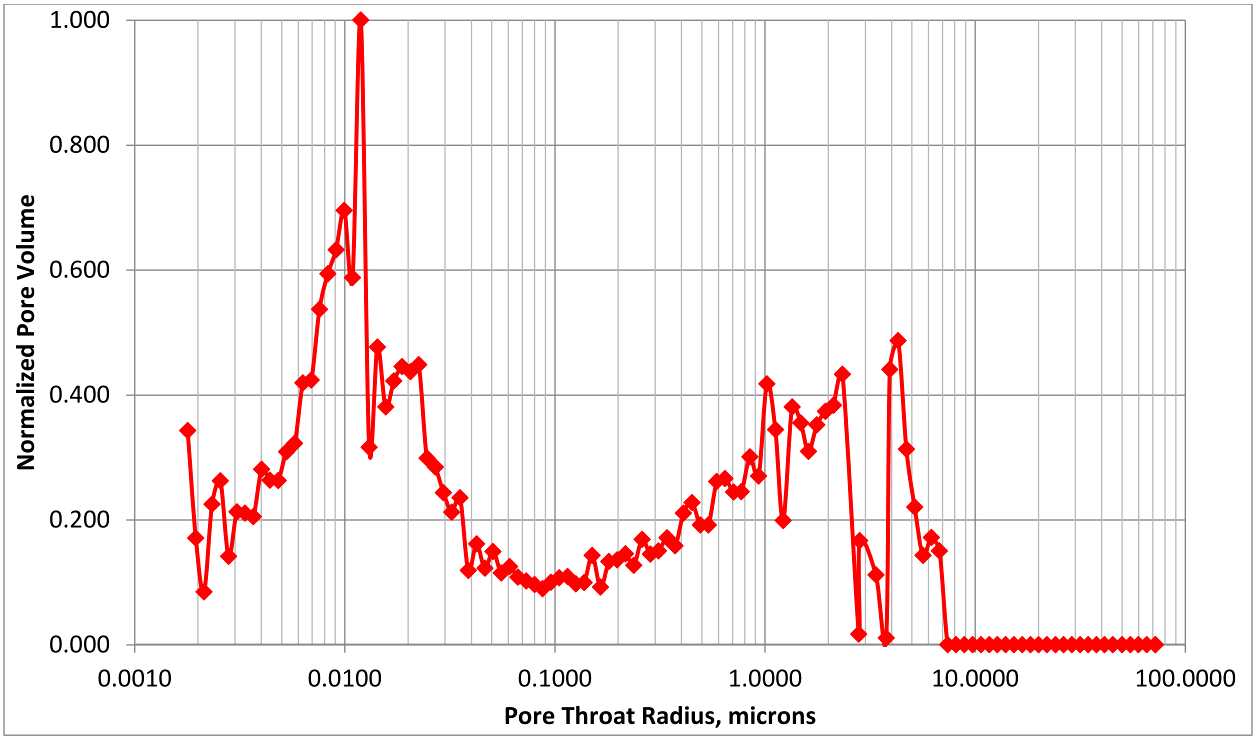

Figure 51. Mercury porosimetry results for sample MICP GI-4-43B (VNT-4). (Upper) Mercury intrusion (red) and extrusion (blue) plotted as mercury saturation as a function of pore size. (Lower) Pore size distribution based on intrusion data.

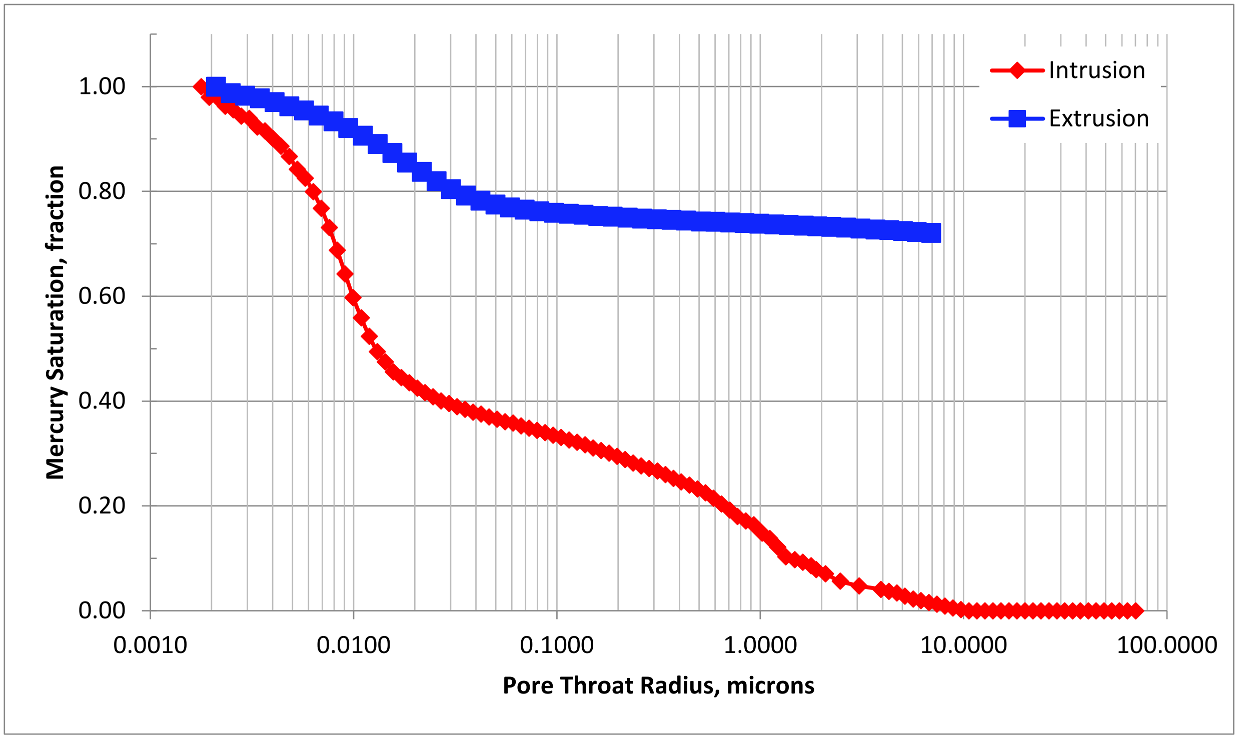

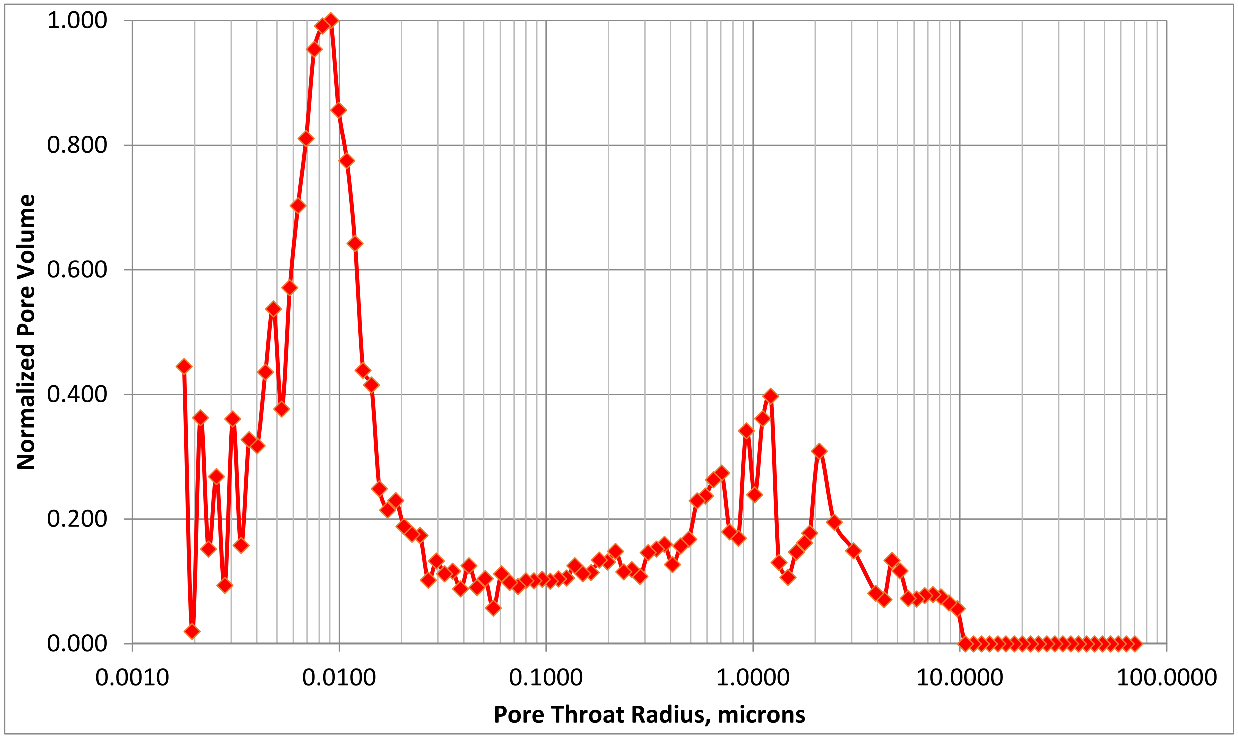

Figure 52. Mercury porosimetry results for sample MICP GI-4-44 (VNT-4). (Upper) Mercury intrusion (red) and extrusion (blue) plotted as mercury saturation as a function of pore size. (Lower) Pore size distribution based on intrusion data.

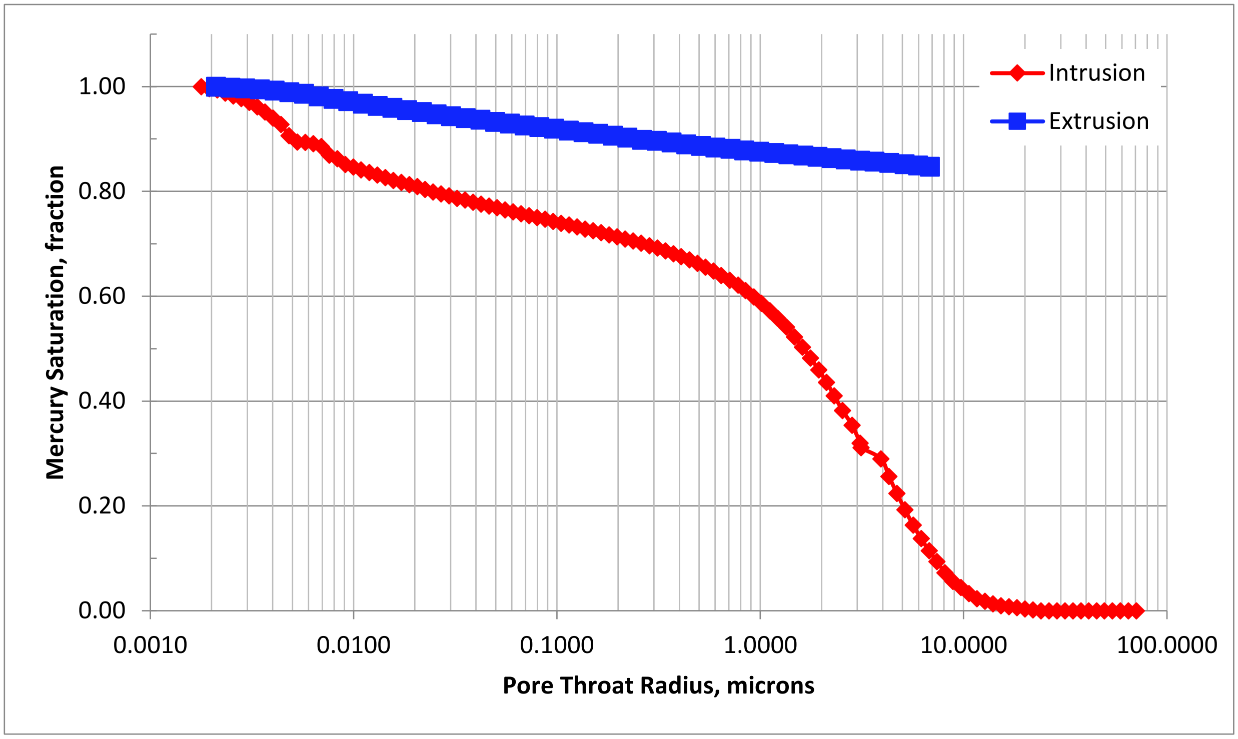

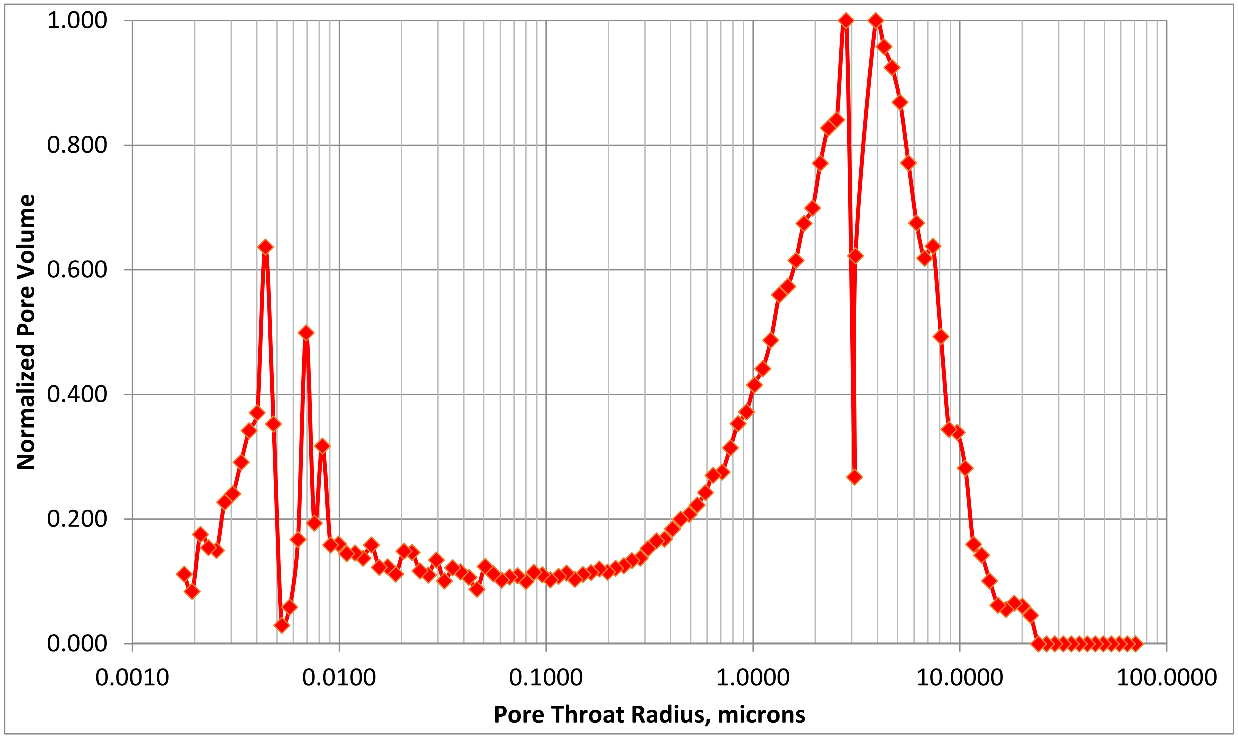

Figure 53. Mercury porosimetry results for sample MICP GI-4-54 (VNT-4). (Upper) Mercury intrusion (red) and extrusion (blue) plotted as mercury saturation as a function of pore size. (Lower) Pore size distribution based on intrusion data.

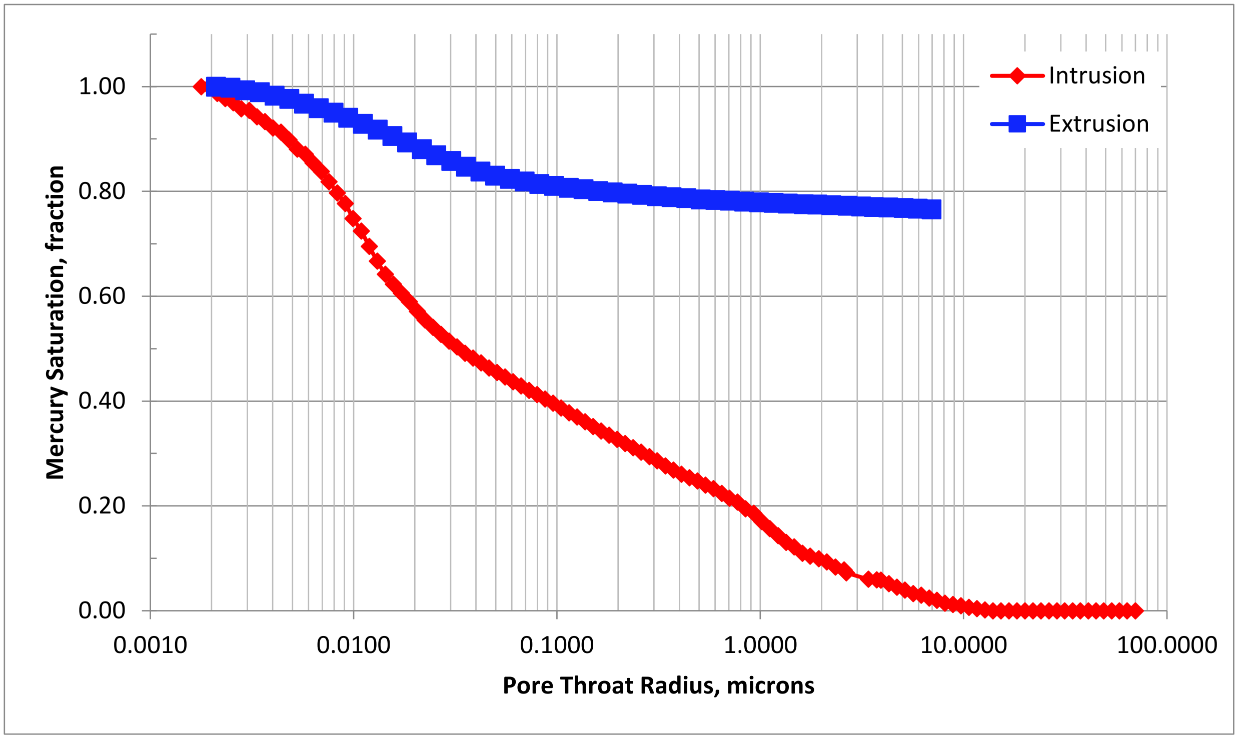

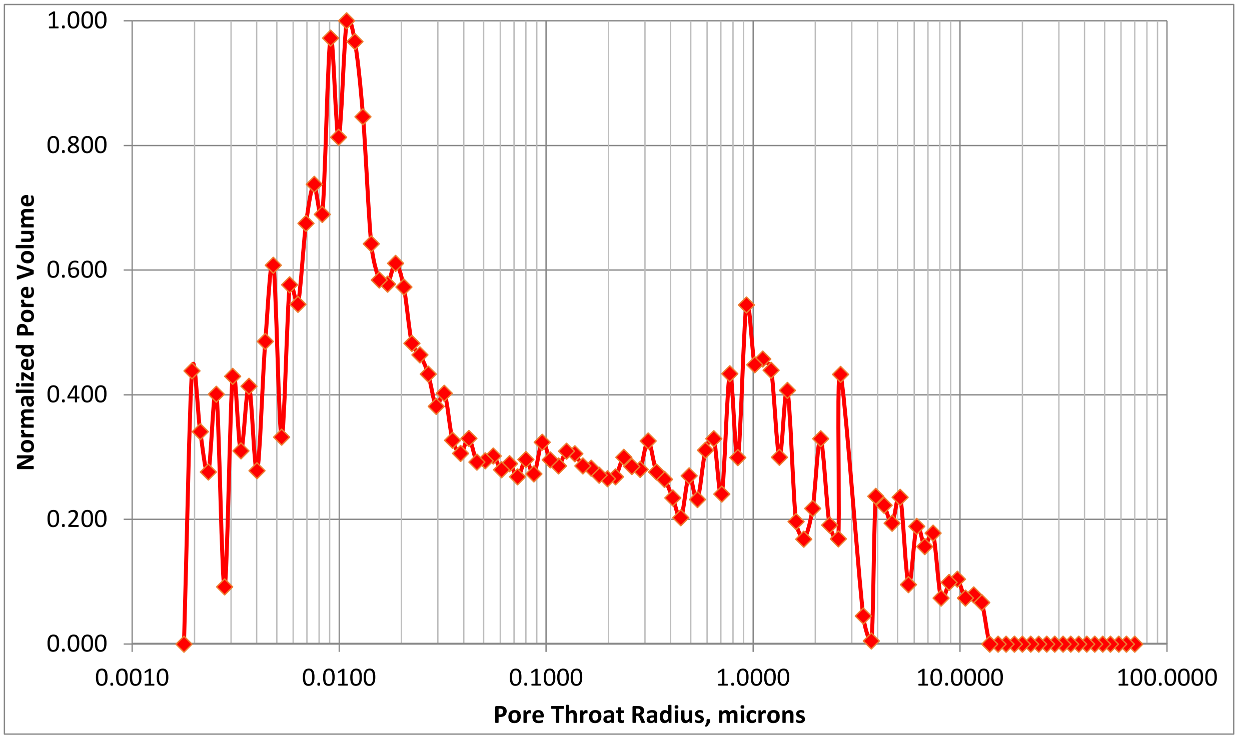

Figure 54. Mercury porosimetry results for sample MICP GI-4-72 (VNT-5). (Upper) Mercury intrusion (red) and extrusion (blue) plotted as mercury saturation as a function of pore size. (Lower) Pore size distribution based on intrusion data.

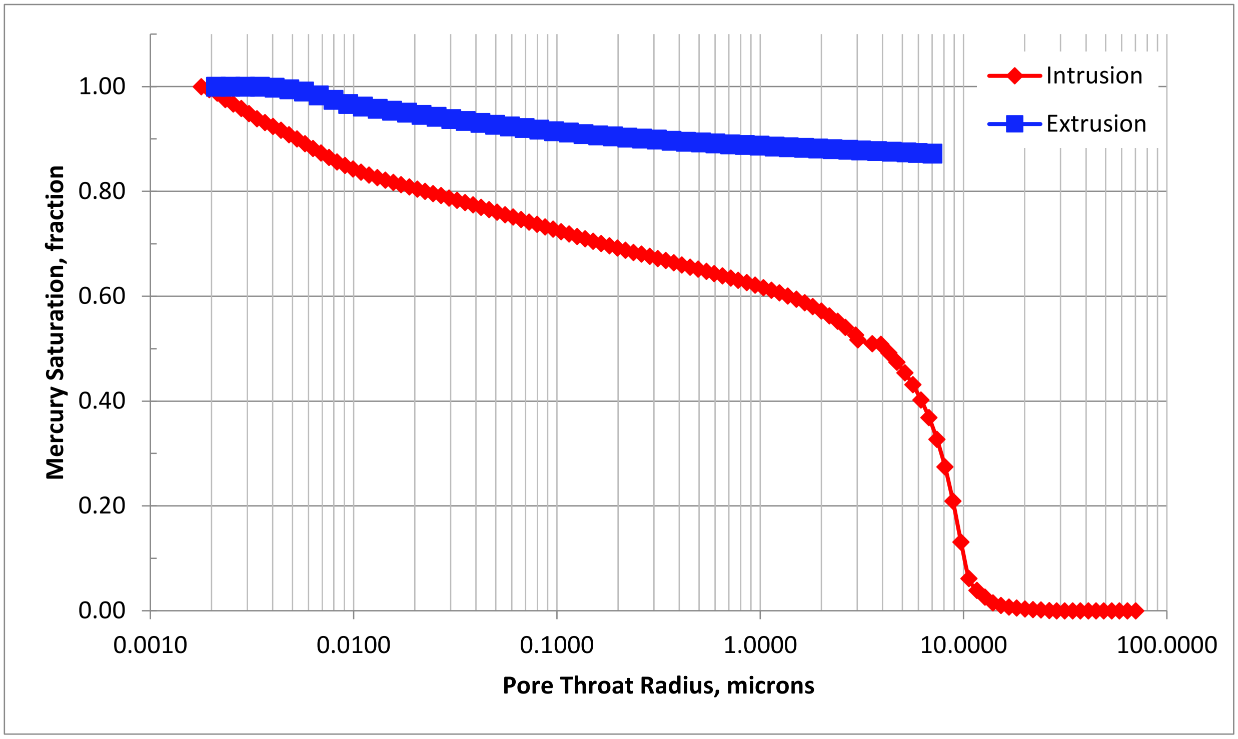

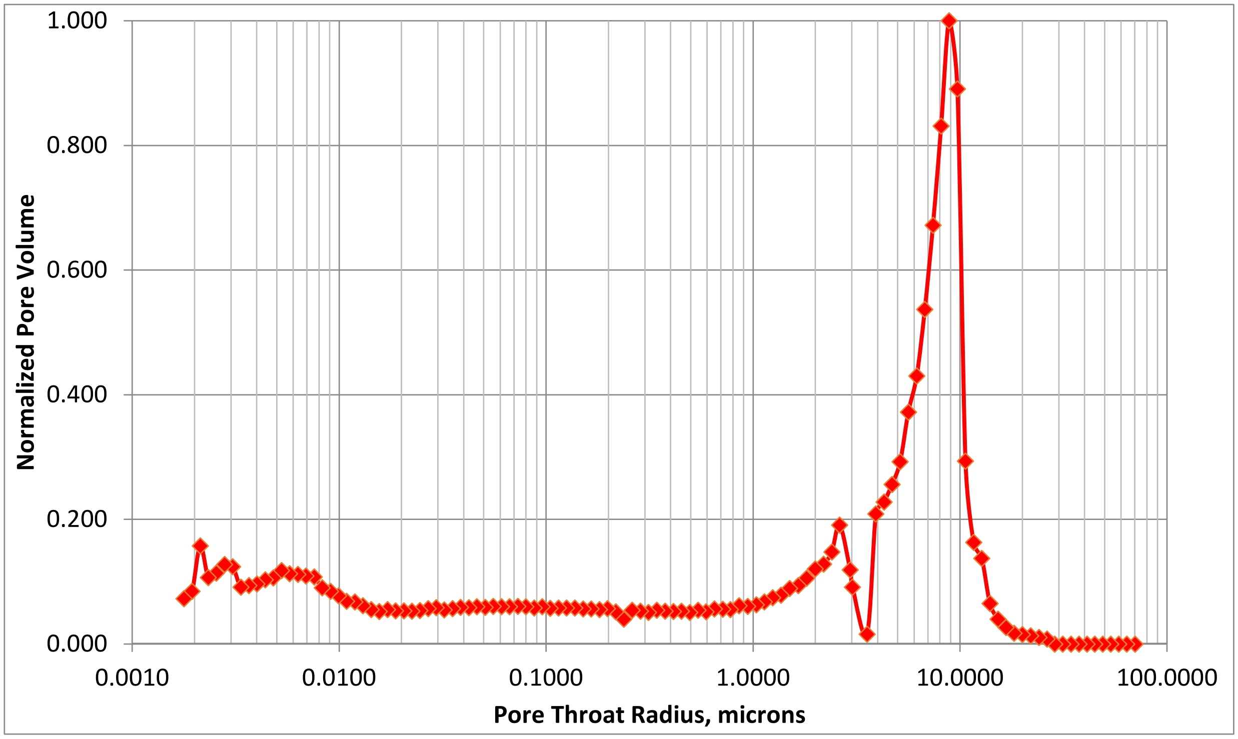

Figure 55. Mercury porosimetry results for sample MICP DA-1-17 (VNT-6). (Upper) Mercury intrusion (red) and extrusion (blue) plotted as mercury saturation as a function of pore size. (Lower) Pore size distribution based on intrusion data.

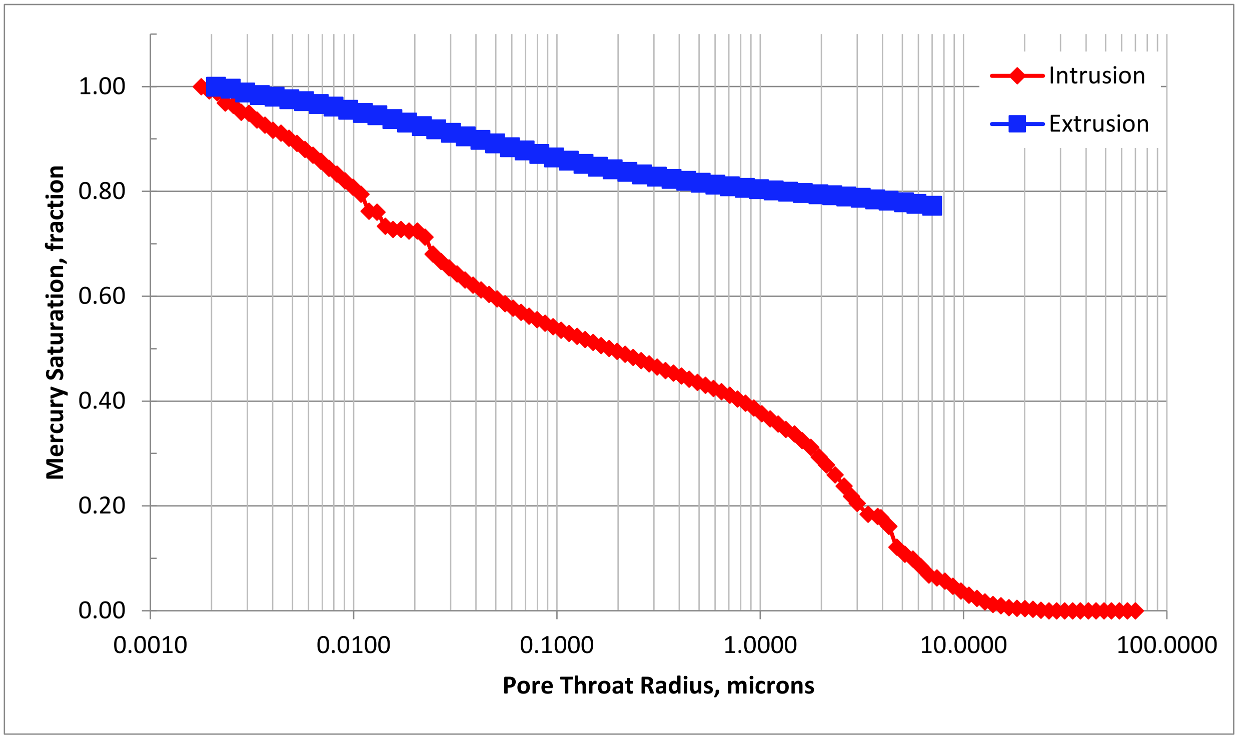

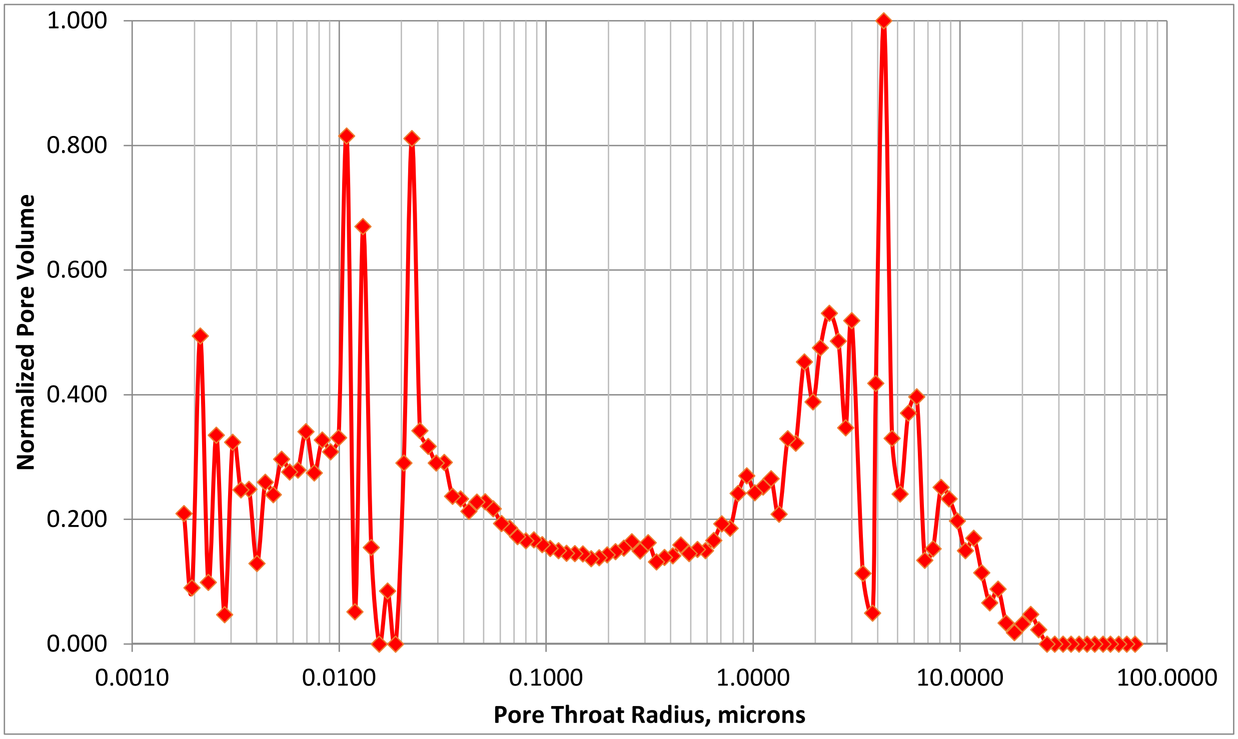

Figure 56. Mercury porosimetry results for sample MICP DA-1-36 (VNT-10). (Upper) Mercury intrusion (red) and extrusion (blue) plotted as mercury saturation as a function of pore size. (Lower) Pore size distribution based on intrusion data.

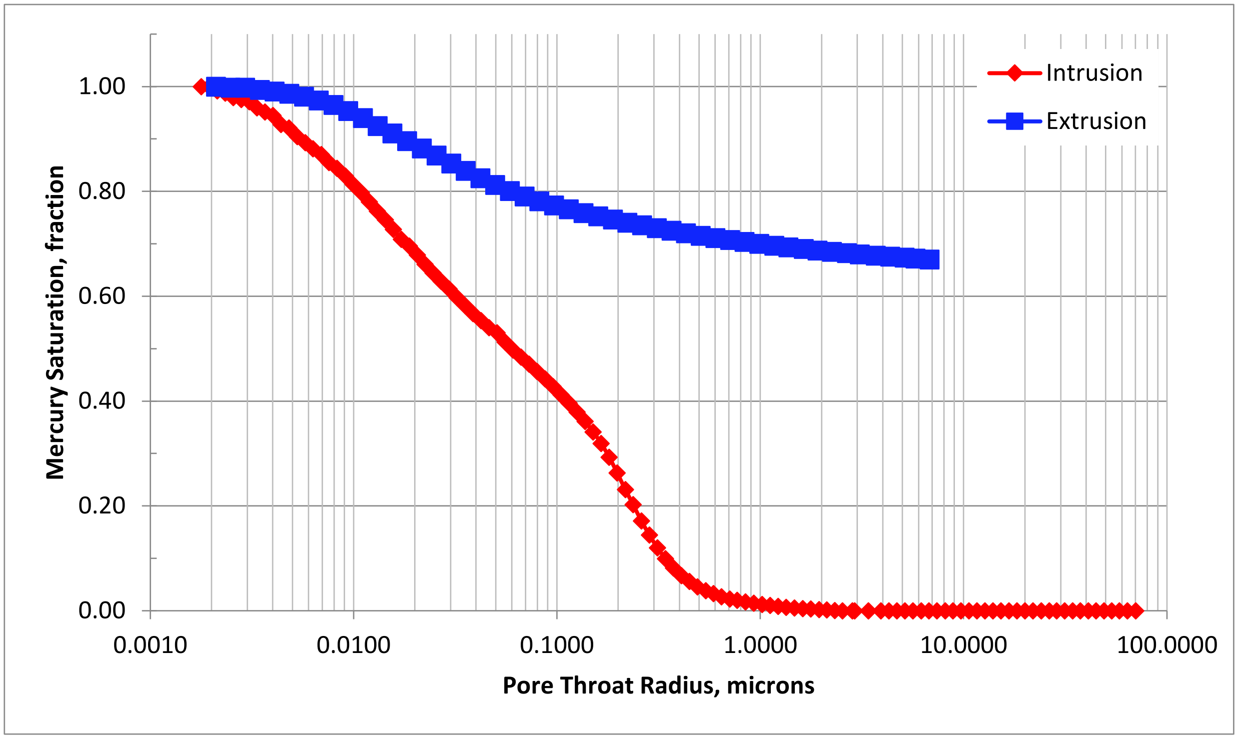

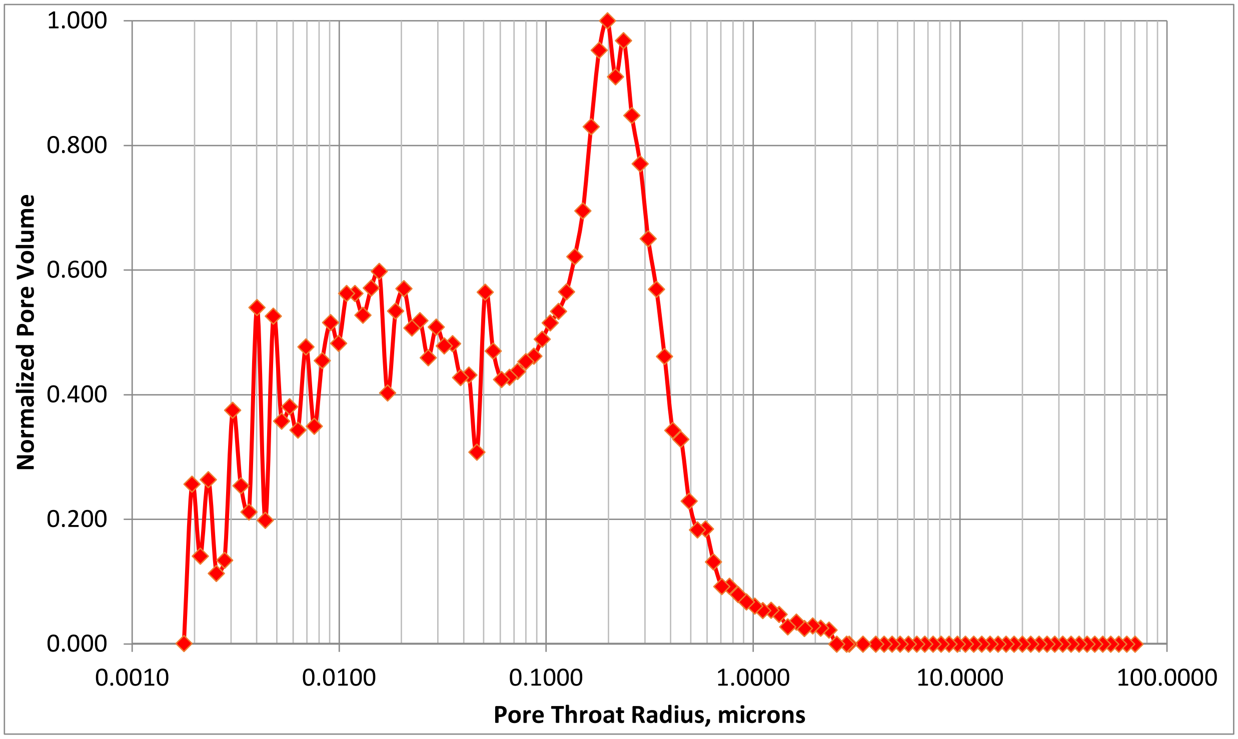

Figure 57. Mercury porosimetry results for sample MICP AC-1-111 (UZNT). (Upper) Mercury intrusion (red) and extrusion (blue) plotted as mercury saturation as a function of pore size. (Lower) Pore size distribution based on intrusion data.

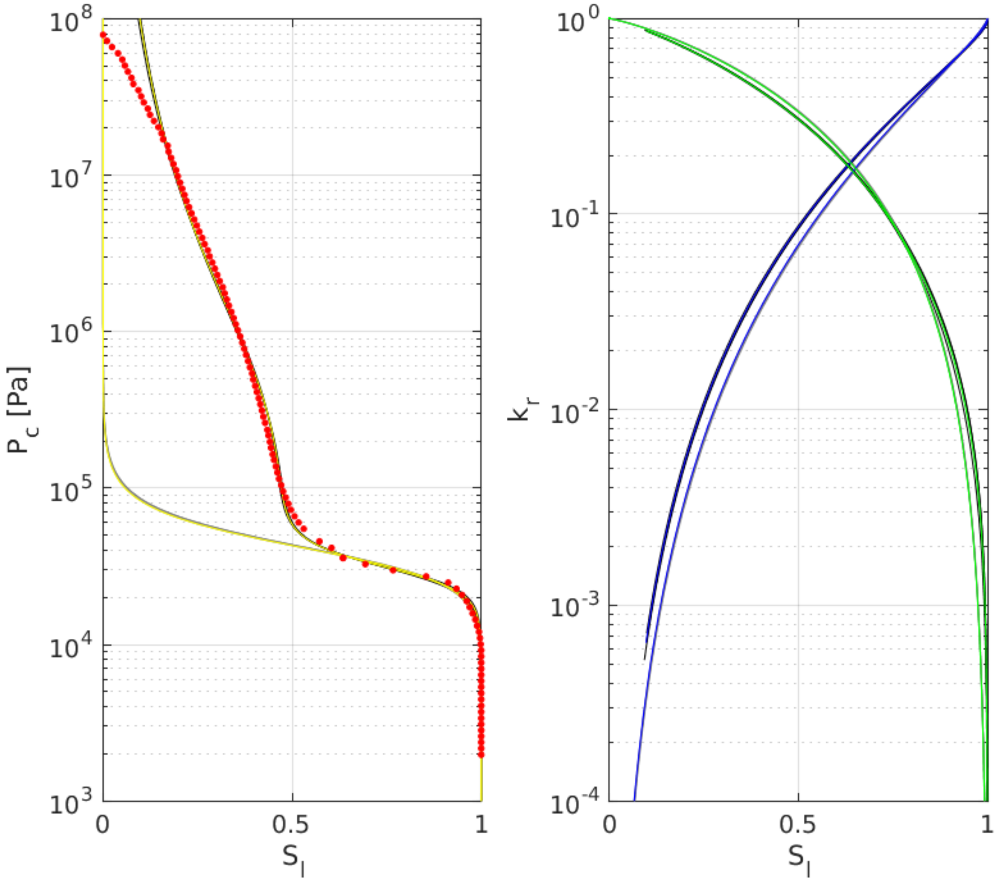

Figure 58. Sample GI-2-6A (VNT-1) converted mercury intrusion capillary pressure (MICP) measurements, fits, and estimated relative permeability. (Left) MICP data converted to air-water system (red dots) with uni- and bi-modal fits (grey and black, respectively). (Right) Predicted water and air relative permeability based on the fitting parameters of the MICP data. Water and air relative permeability reaches 1 and 0, respectively, on the right side of the plot. Grey and black are for predictions based on uni- and bi-modal parameters, respectively. Blue and green lines indicate the mean of the predictions, respectively, for the water and air curves.

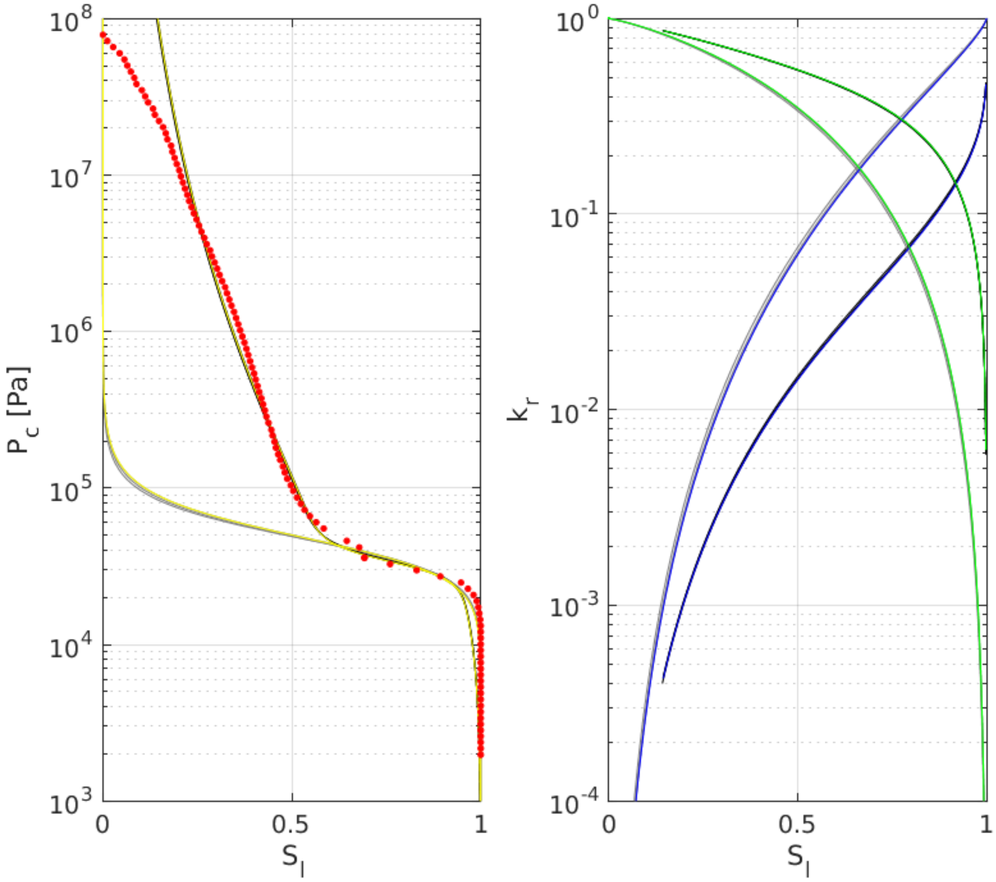

Figure 59. Sample GI-2-6B (VNT-1) converted mercury intrusion capillary pressure (MICP) measurements, fits, and estimated relative permeability. (Left) MICP data converted to air-water system (red dots) with uni- and bi-modal fits (grey and black, respectively). (Right) Predicted water and air relative permeability based on the fitting parameters of the MICP data. Water and air relative permeability reaches 1 and 0, respectively, on the right side of the plot. Grey and black are for predictions based on uni- and bi-modal parameters, respectively. Blue and green lines indicate the mean of the predictions, respectively, for the water and air curves.

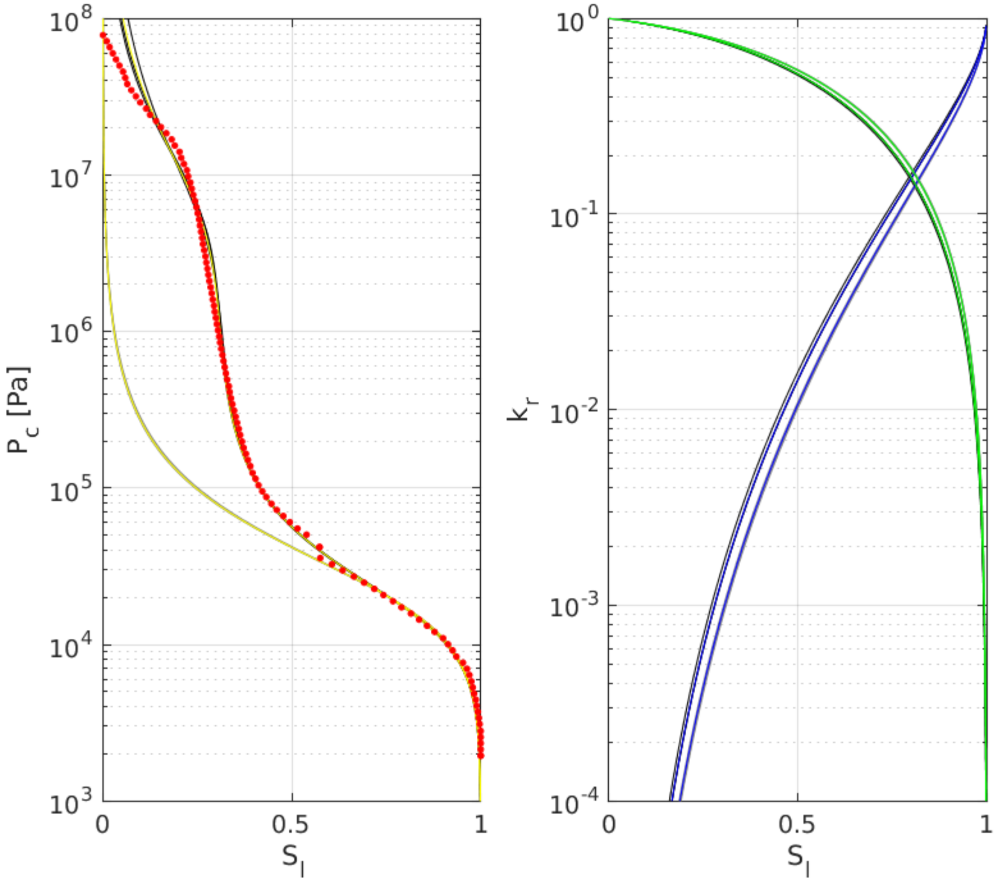

Figure 60. Sample GI-3-2A (VNT-2) converted mercury intrusion capillary pressure (MICP) measurements, fits, and estimated relative permeability. (Left) MICP data converted to air-water system (red dots) with uni- and bi-modal fits (grey and black, respectively). (Right) Predicted water and air relative permeability based on the fitting parameters of the MICP data. Water and air relative permeability reaches 1 and 0, respectively, on the right side of the plot. Grey and black are for predictions based on uni- and bi-modal parameters, respectively. Blue and green lines indicate the mean of the predictions, respectively, for the water and air curves.

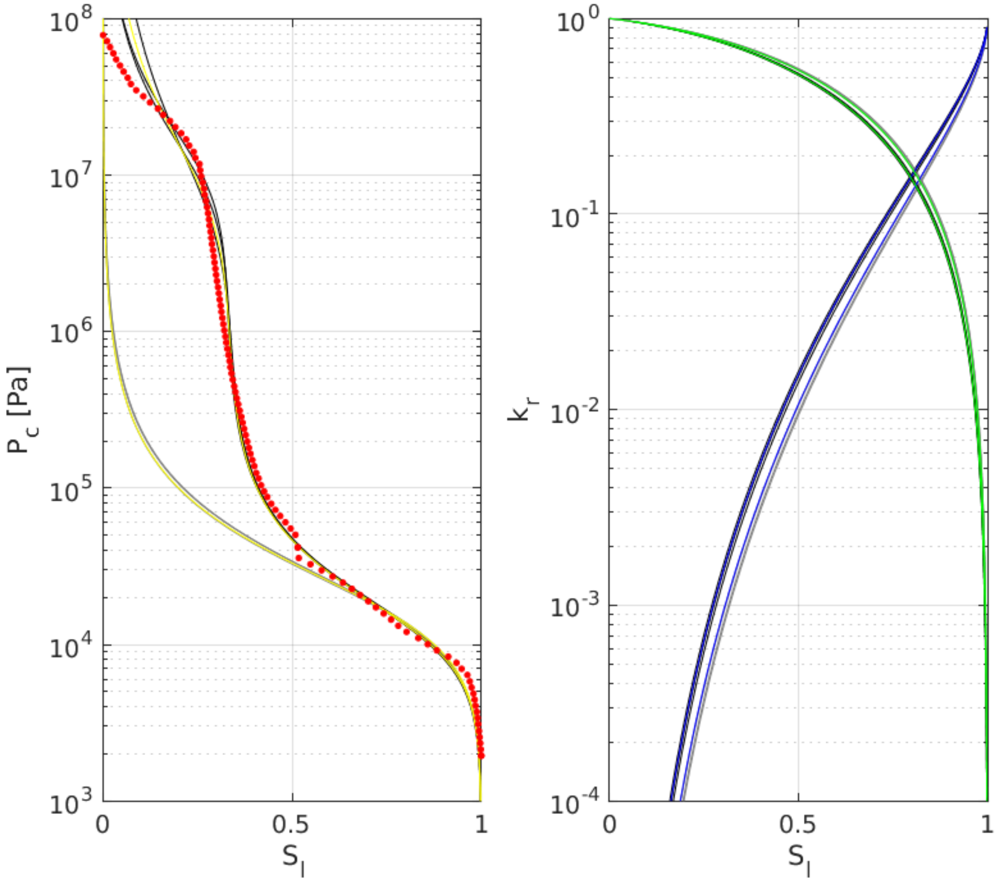

Figure 61. Sample GI-3-2B (VNT-2) converted mercury intrusion capillary pressure (MICP) measurements, fits, and estimated relative permeability. (Left) MICP data converted to air-water system (red dots) with uni- and bi-modal fits (grey and black, respectively). (Right) Predicted water and air relative permeability based on the fitting parameters of the MICP data. Water and air relative permeability reaches 1 and 0, respectively, on the right side of the plot. Grey and black are for predictions based on uni- and bi-modal parameters, respectively. Blue and green lines indicate the mean of the predictions, respectively, for the water and air curves.

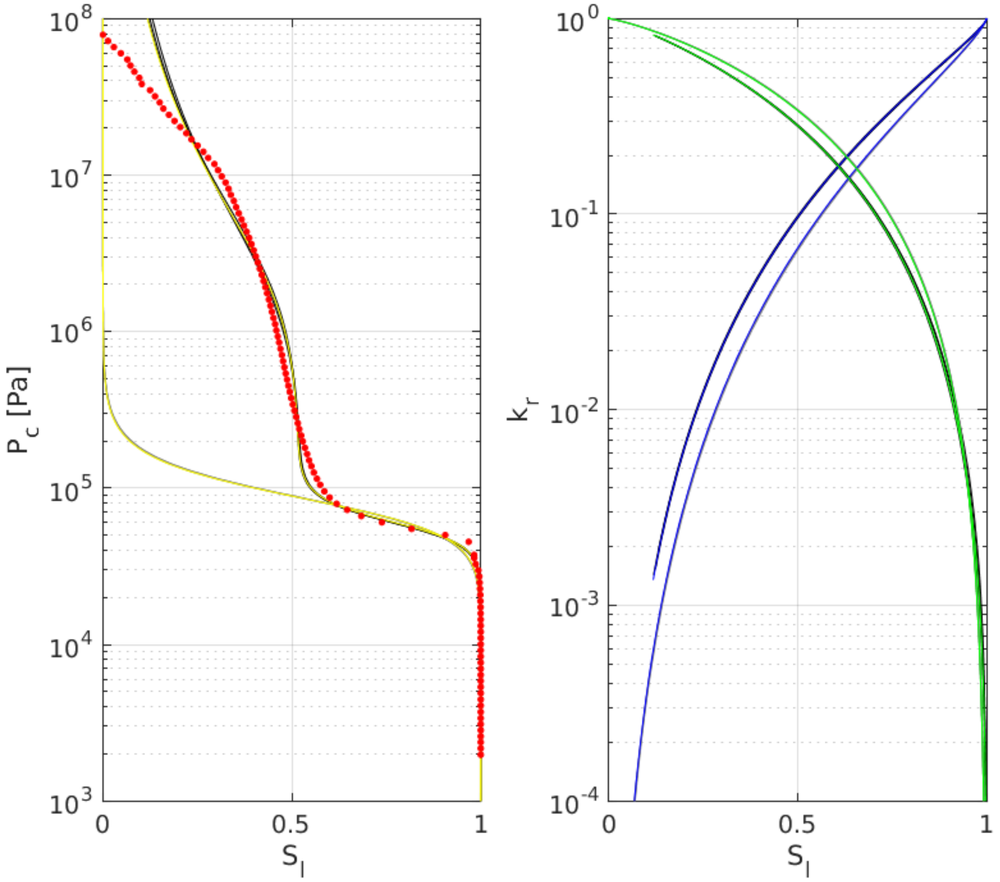

Figure 62. Sample GI-3-21A (VNT-3) converted mercury intrusion capillary pressure (MICP) measurements, fits, and estimated relative permeability. (Left) MICP data converted to air-water system (red dots) with uni- and bi-modal fits (grey and black, respectively). (Right) Predicted water and air relative permeability based on the fitting parameters of the MICP data. Water and air relative permeability reaches 1 and 0, respectively, on the right side of the plot. Grey and black are for predictions based on uni- and bi-modal parameters, respectively. Blue and green lines indicate the mean of the predictions, respectively, for the water and air curves.

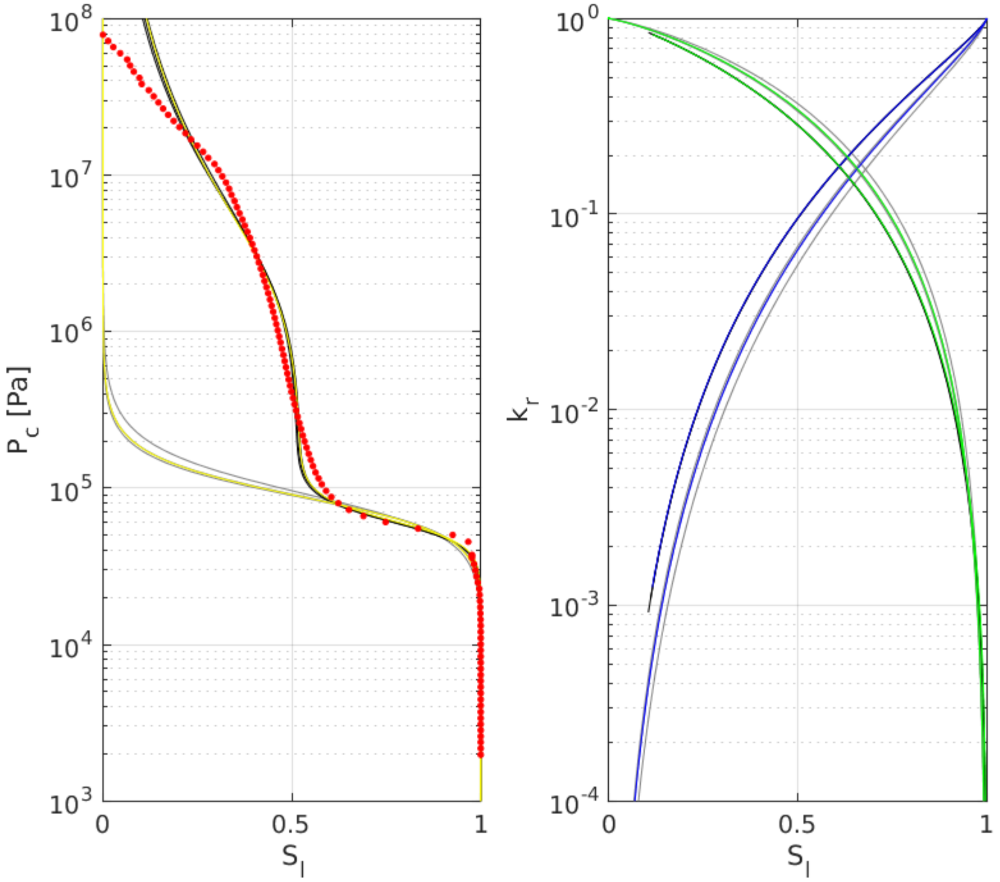

Figure 63. Sample GI-3-21B (VNT-3) converted mercury intrusion capillary pressure (MICP) measurements, fits, and estimated relative permeability. (Left) MICP data converted to air-water system (red dots) with uni- and bi-modal fits (grey and black, respectively). (Right) Predicted water and air relative permeability based on the fitting parameters of the MICP data. Water and air relative permeability reaches 1 and 0, respectively, on the right side of the plot. Grey and black are for predictions based on uni- and bi-modal parameters, respectively. Blue and green lines indicate the mean of the predictions, respectively, for the water and air curves.

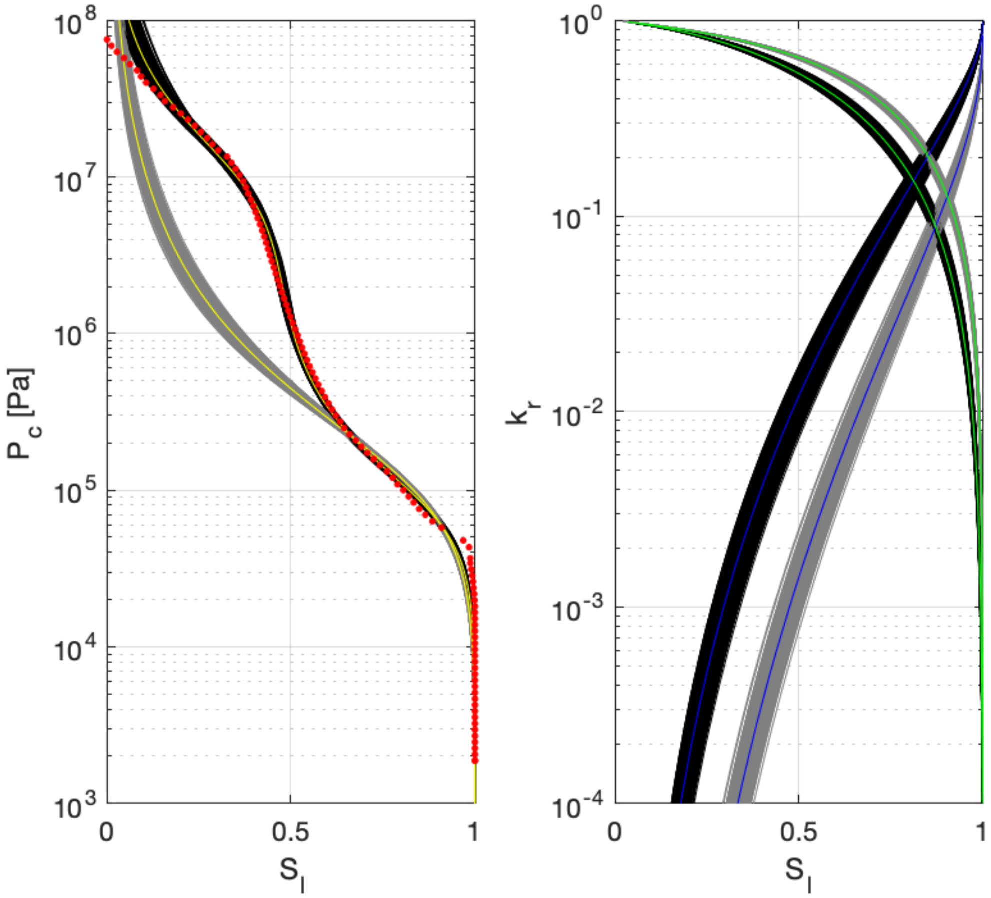

Figure 64. Sample GI-4-18 (VNT-3) converted mercury intrusion capillary pressure (MICP) measurements, fits, and estimated relative permeability. (Left) MICP data converted to air-water system (red dots) with uni- and bi-modal fits (grey and black, respectively). (Right) Predicted water and air relative permeability based on the fitting parameters of the MICP data. Water and air relative permeability reaches 1 and 0, respectively, on the right side of the plot. Grey and black are for predictions based on uni- and bi-modal parameters, respectively. Blue and green lines indicate the mean of the predictions, respectively, for the water and air curves.

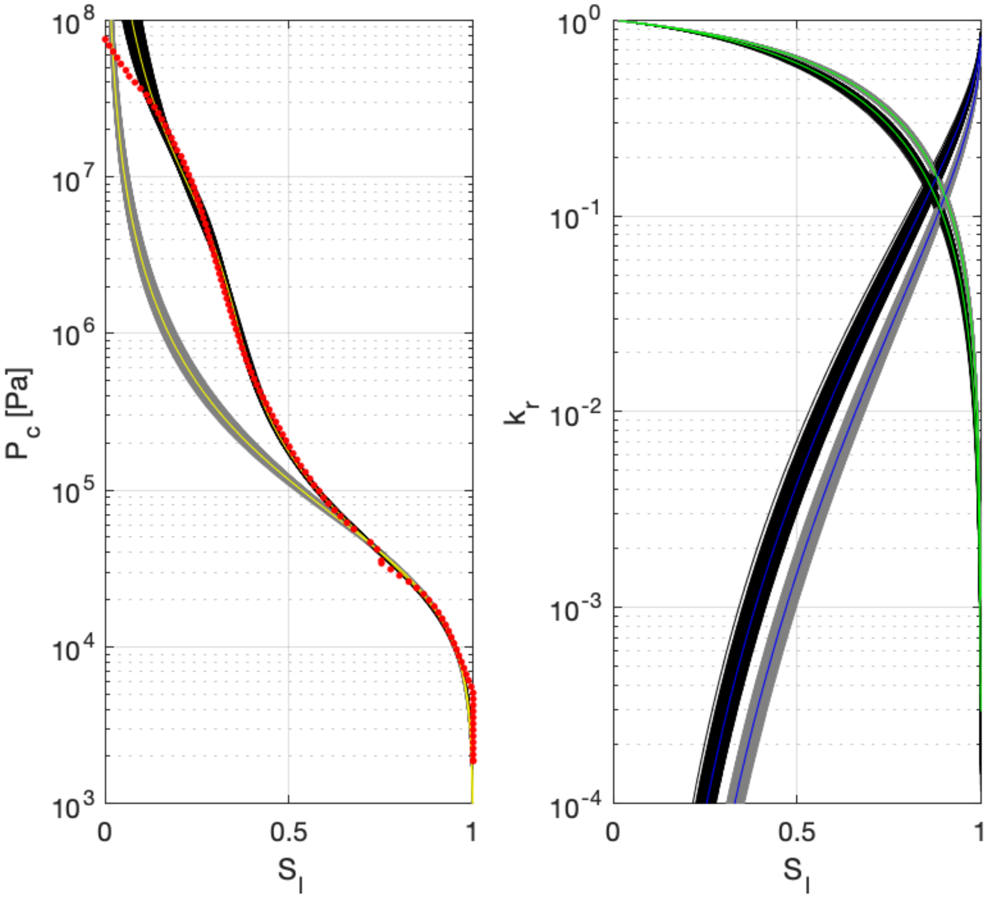

Figure 65. Sample GI-4-35 (VNT-3) converted mercury intrusion capillary pressure (MICP) measurements, fits, and estimated relative permeability. (Left) MICP data converted to air-water system (red dots) with uni- and bi-modal fits (grey and black, respectively). (Right) Predicted water and air relative permeability based on the fitting parameters of the MICP data. Water and air relative permeability reaches 1 and 0, respectively, on the right side of the plot. Grey and black are for predictions based on uni- and bi-modal parameters, respectively. Blue and green lines indicate the mean of the predictions, respectively, for the water and air curves.

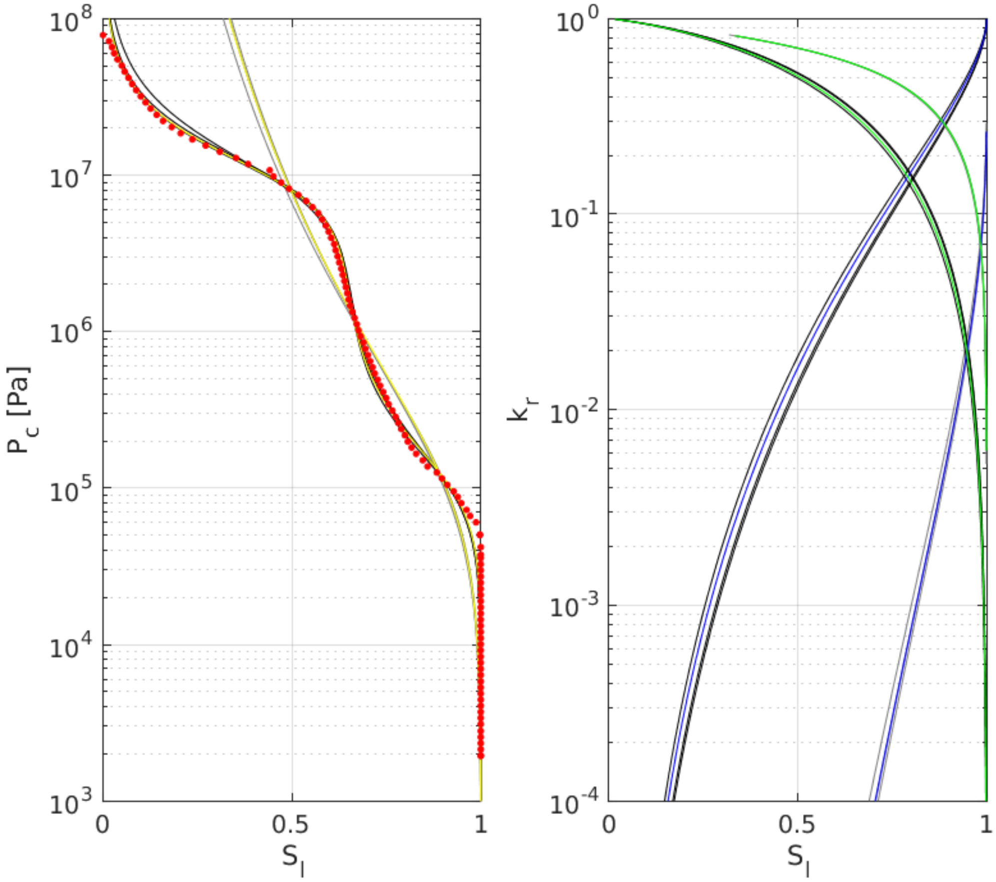

Figure 66. Sample GI-4-43A (VNT-4) converted mercury intrusion capillary pressure (MICP) measurements, fits, and estimated relative permeability. (Left) MICP data converted to air-water system (red dots) with uni- and bi-modal fits (grey and black, respectively). (Right) Predicted water and air relative permeability based on the fitting parameters of the MICP data. Water and air relative permeability reaches 1 and 0, respectively, on the right side of the plot. Grey and black are for predictions based on uni- and bi-modal parameters, respectively. Blue and green lines indicate the mean of the predictions, respectively, for the water and air curves.

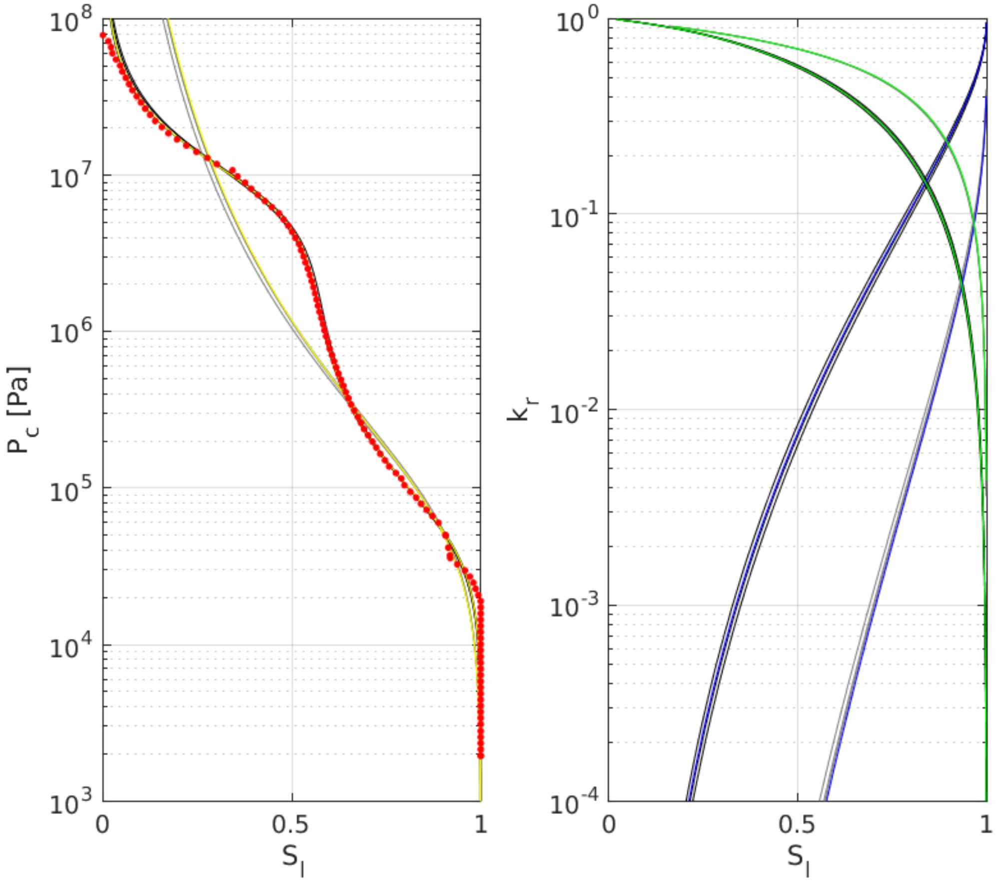

Figure 67. Sample GI-4-43B (VNT-4) converted mercury intrusion capillary pressure (MICP) measurements, fits, and estimated relative permeability. (Left) MICP data converted to air-water system (red dots) with uni- and bi-modal fits (grey and black, respectively). (Right) Predicted water and air relative permeability based on the fitting parameters of the MICP data. Water and air relative permeability reaches 1 and 0, respectively, on the right side of the plot. Grey and black are for predictions based on uni- and bi-modal parameters, respectively. Blue and green lines indicate the mean of the predictions, respectively, for the water and air curves.

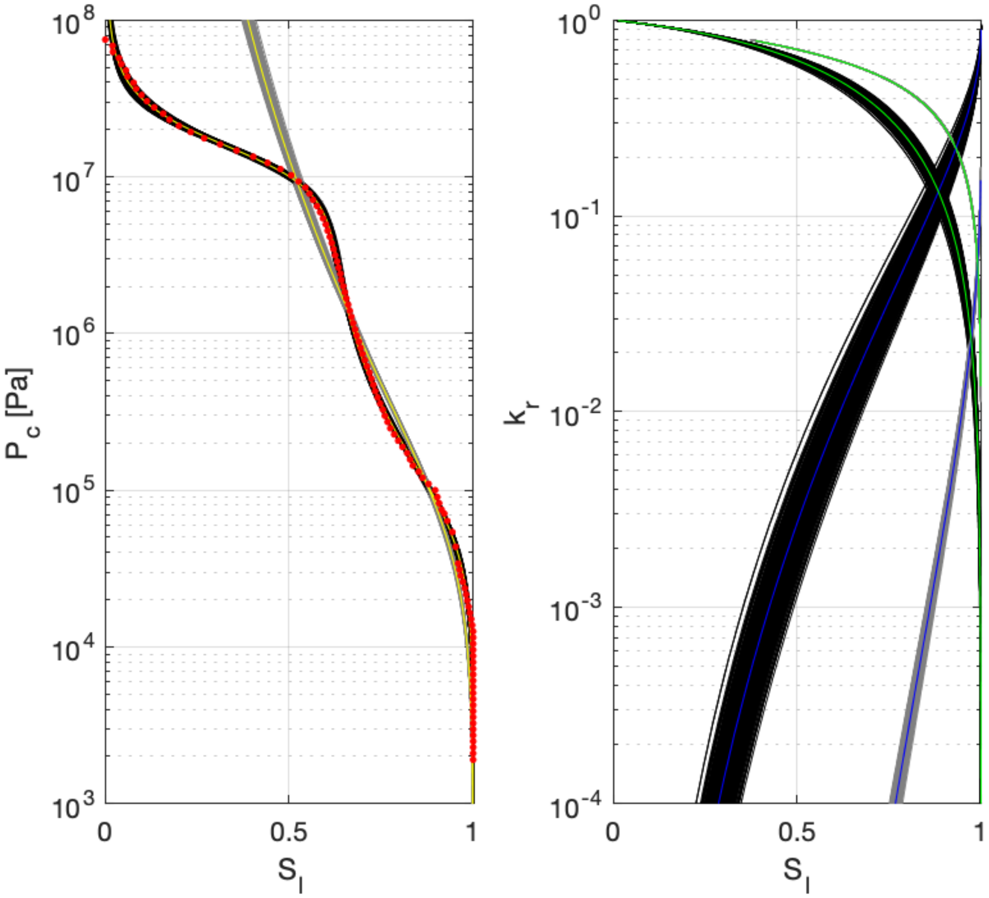

Figure 68. Sample GI-4-44 (VNT-4) converted mercury intrusion capillary pressure (MICP) measurements, fits, and estimated relative permeability. (Left) MICP data converted to air-water system (red dots) with uni- and bi-modal fits (grey and black, respectively). (Right) Predicted water and air relative permeability based on the fitting parameters of the MICP data. Water and air relative permeability reaches 1 and 0, respectively, on the right side of the plot. Grey and black are for predictions based on uni- and bi-modal parameters, respectively. Blue and green lines indicate the mean of the predictions, respectively, for the water and air curves.

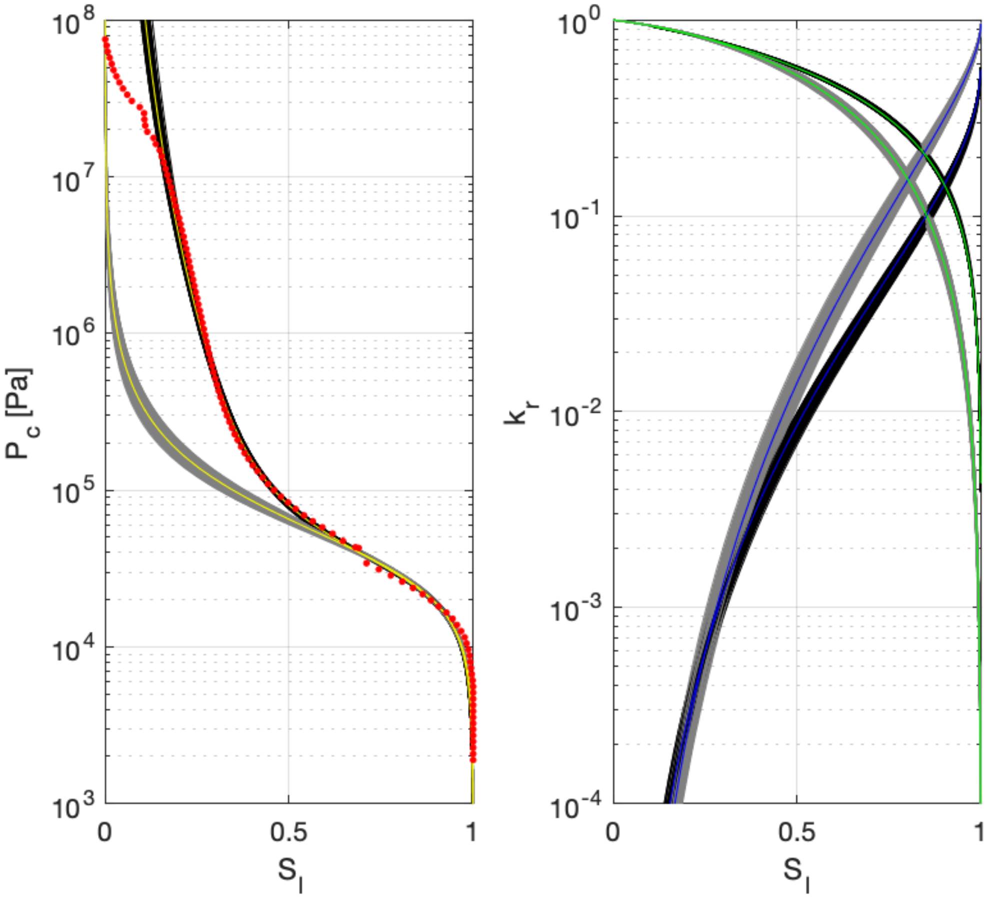

Figure 69. Sample GI-4-54 (VNT-4; rerun) converted mercury intrusion capillary pressure (MICP) measurements, fits, and estimated relative permeability. (Left) MICP data converted to air-water system (red dots) with uni- and bi-modal fits (grey and black, respectively). (Right) Predicted water and air relative permeability based on the fitting parameters of the MICP data. Water and air relative permeability reaches 1 and 0, respectively, on the right side of the plot. Grey and black are for predictions based on uni- and bi-modal parameters, respectively. Blue and green lines indicate the mean of the predictions, respectively, for the water and air curves.

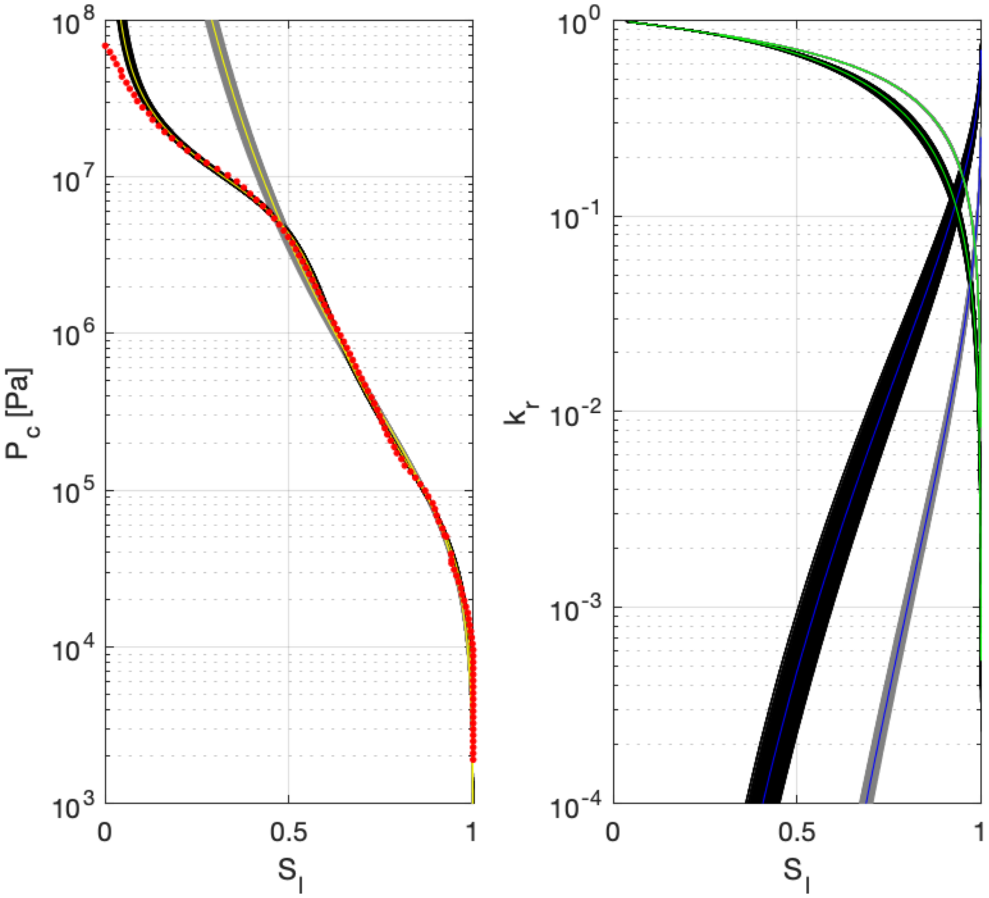

Figure 70. Sample GI-4-72 (VNT-5) converted mercury intrusion capillary pressure (MICP) measurements, fits, and estimated relative permeability. (Left) MICP data converted to air-water system (red dots) with uni- and bi-modal fits (grey and black, respectively). (Right) Predicted water and air relative permeability based on the fitting parameters of the MICP data. Water and air relative permeability reaches 1 and 0, respectively, on the right side of the plot. Grey and black are for predictions based on uni- and bi-modal parameters, respectively. Blue and green lines indicate the mean of the predictions, respectively, for the water and air curves.

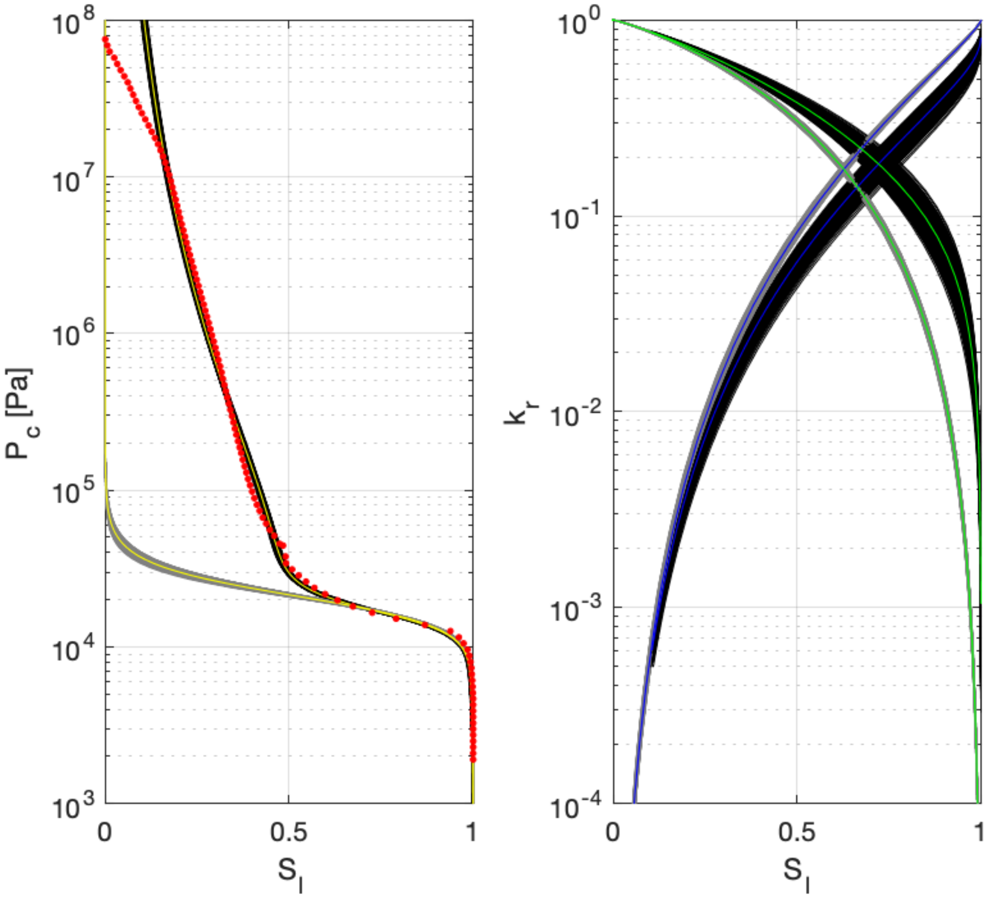

Figure 71. Sample DA-1-17 (VNT-6) converted mercury intrusion capillary pressure (MICP) measurements, fits, and estimated relative permeability. (Left) MICP data converted to air-water system (red dots) with uni- and bi-modal fits (grey and black, respectively). (Right) Predicted water and air relative permeability based on the fitting parameters of the MICP data. Water and air relative permeability reaches 1 and 0, respectively, on the right side of the plot. Grey and black are for predictions based on uni- and bi-modal parameters, respectively. Blue and green lines indicate the mean of the predictions, respectively, for the water and air curves.

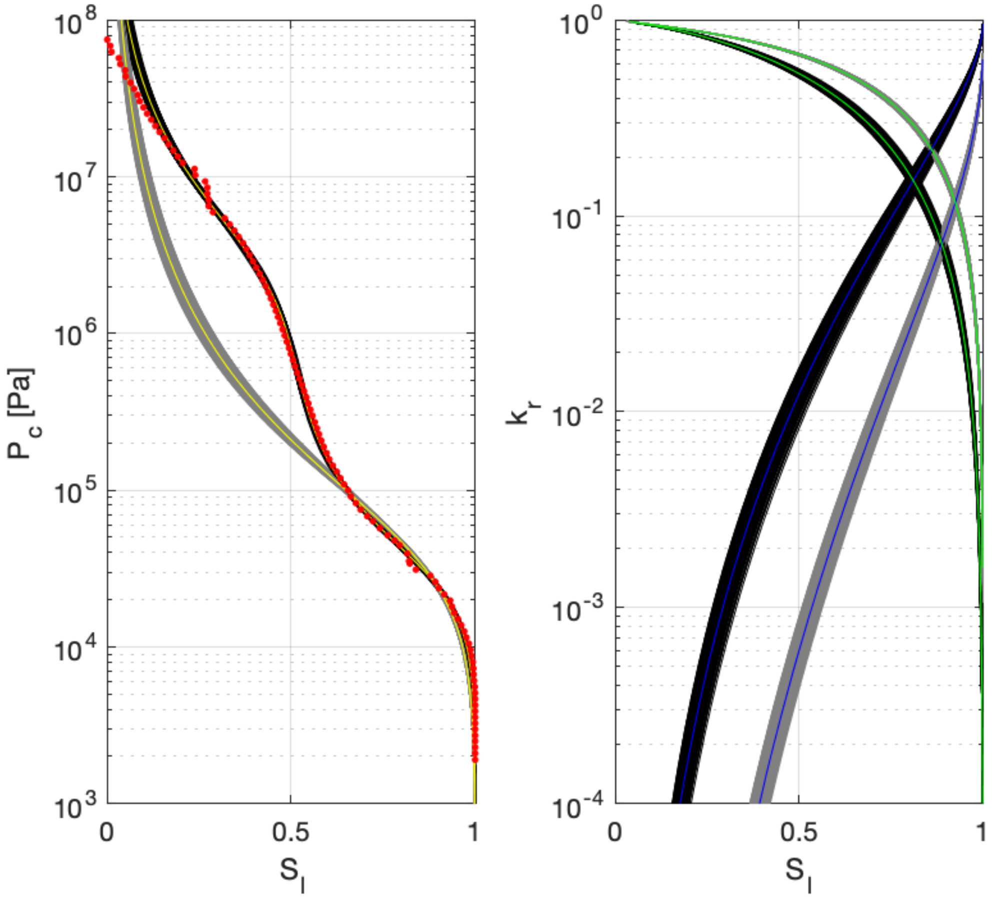

Figure 72. Sample DA-1-36 (VNT-10) converted mercury intrusion capillary pressure (MICP) measurements, fits, and estimated relative permeability. (Left) MICP data converted to air-water system (red dots) with uni- and bi-modal fits (grey and black, respectively) for sample. (Right) Predicted water and air relative permeability based on the fitting parameters of the MICP data. Water and air relative permeability reaches 1 and 0, respectively, on the right side of the plot. Grey and black are for predictions based on uni- and bi-modal parameters, respectively. Blue and green lines indicate the mean of the predictions, respectively, for the water and air curves.

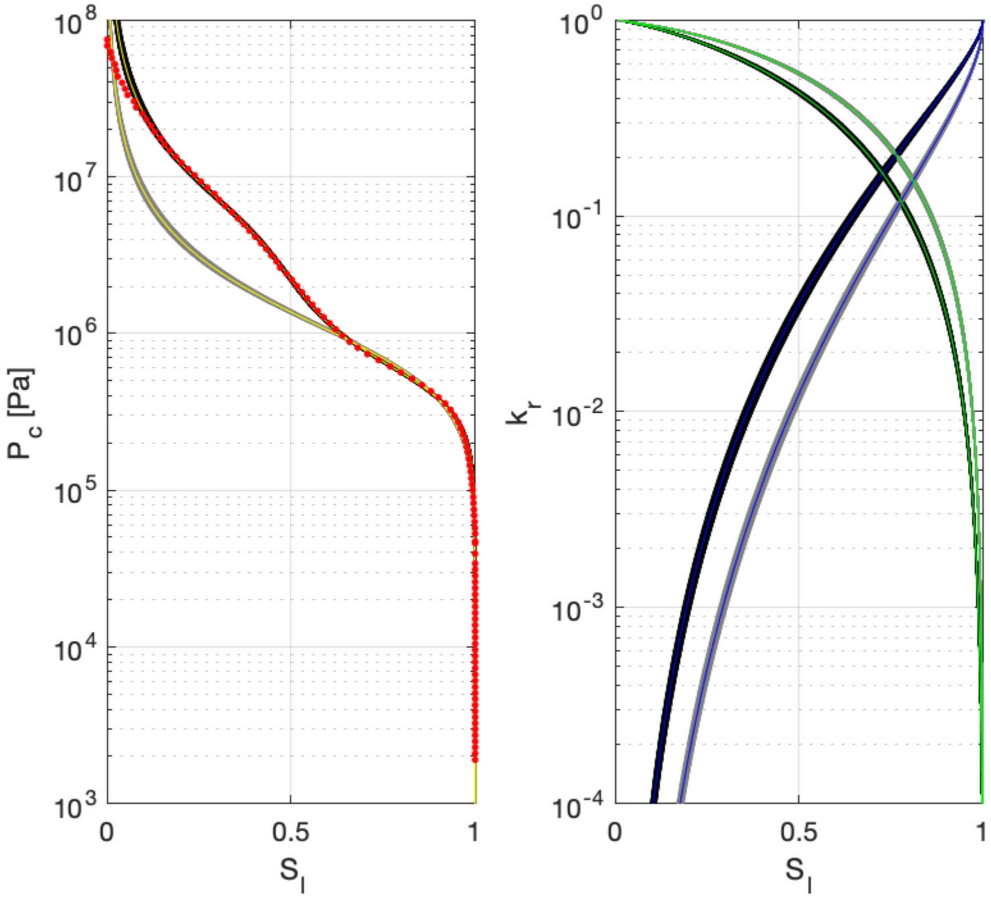

Figure 73. Sample AC-1-111 (UZNT) converted mercury intrusion capillary pressure (MICP) measurements, fits, and estimated relative permeability. (Left) MICP data converted to air-water system (red dots) with uni- and bi-modal fits (grey and black, respectively). (Right) Predicted water and air relative permeability based on the fitting parameters of the MICP data. Water and air relative permeability reaches 1 and 0, respectively, on the right side of the plot. Grey and black are for predictions based on uni- and bi-modal parameters, respectively. Blue and green lines indicate the mean of the predictions, respectively, for the water and air curves.

3.3.2. Thermogravimetric Analysis

Thermogravimetric analyses (TGA) were conducted under a nitrogen environment using the SDT650 thermal analyzer by TA Instruments. Seventeen powdered samples have been analyzed—these powdered samples are from the same powdered material used in XRD (see Section 3.2.2). In addition, one non-powdered chip for sample DA-1-19 at ~5 mm in diameter was analyzed to compare with the powder TGA (Figure 58 and Figure 59). About 20 to 50 mg of the powdered samples were loaded in alumina pans of 6.55 mm outer diameter × 4 mm height. Heating-ramp and holding sequences are as follows:

- ramp 1 °C/min to 27°C and hold for 240 mins;
- ramp 5 °C/min to 100°C and keep isothermal for 240 mins;
- ramp 5 °C/min to 200°C and keep isothermal for 240 mins; and
- ramp either 5 or 10 °C/min from 200°C to 900°C.

For natural clinoptilolite-bearing tuff samples from the NNSS, Knowlton et al. (1981) used TGA to distinguish three types of water that can be associated with zeolite clinoptilolite: external water, loosely bound, and tightly bound water with transitions at temperatures of 75 ± 10°C, 171 ± 2°C and 271 ± 4°C, respectively. These temperatures were determined by TGA under vacuum conditions, and those authors noted that the temperature transitions are ~50°C higher under heating in a nitrogen atmosphere. However, Bish (1993) in reviewing thermal behavior of zeolites states "distinct 'types' of water (e.g., loosely bound or tightly bound zeolitic water) do not exist" and instead speaks of water bound to extra-framework cations with a continuum of energies, and that the amount of water in structural cavities of zeolite affects the zeolites' molar volume. Currently, we generally consider that the weight loss at 100°C or less is corresponding to external water, weight loss at 100–200°C is mostly loosely bound water, whereas the weight loss at > 200°C is tightly bound water. While most of the water loss is related to heating and thus is relatively stable, the weight loss at 27 °C, ~1/3 of the total water, is the least stable or rather most mobile water and can be variable based on the sample handling and exposure to moisture. The TGA samples have variable amount of water loss, ranging from 6% to 12.3% (Table 9). From 200 to 900°C the water loss is 1.6-3%, which may be consistent clinoptilolite tuff for "tight bounded water" reported by Knowlton et al. (1981). Further careful interpretation is needed for these complex multi-mineral/mineraloid samples as they can contain other water-sensitive phases such as swelling clay (e.g., smectite) and opal ($SiO_2 \cdot nH_2O$).

There are subtle differences between the TGA curves for chip and powder (Figure 58 and Figure 59). For example, the powdered sample lost the most water, namely ~3%, within 50 minutes whereas the chip does not reach stable mass even at the end of 240 minutes, suggesting the importance of pore structure and tortuosity on water vapor transport. The chip consistently lost 0.5-0.7% more water than the powdered sample. This suggests that some water, though a very small portion, is lost during powder preparation.

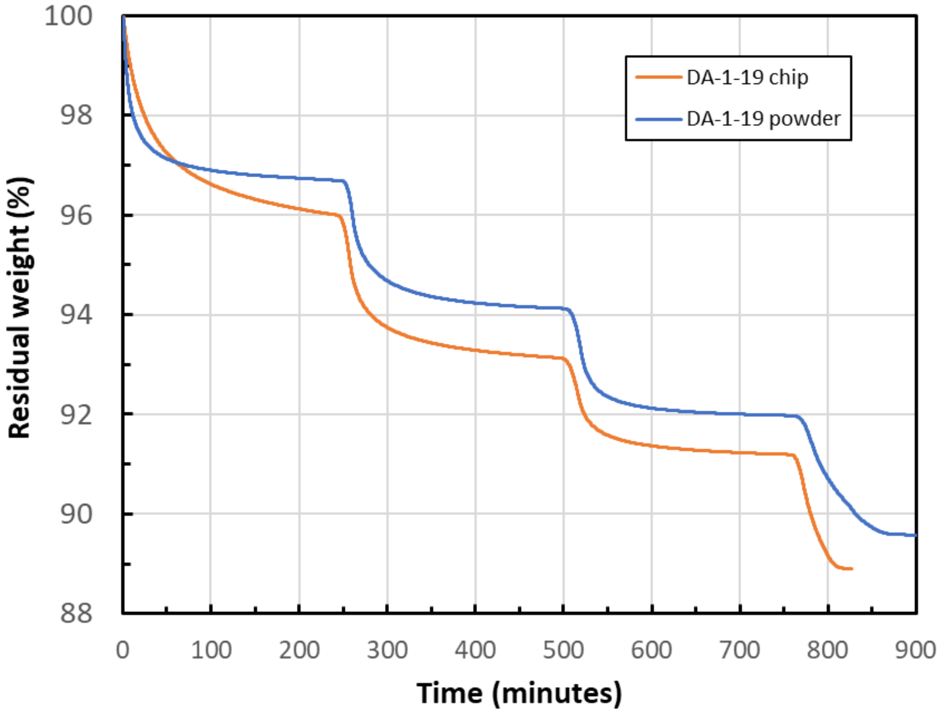

Figure 74. Residual weight versus time during TGA for sample DA-1-19 (VNT-7) in chip (70.6 mg) and powder (25 mg) forms.

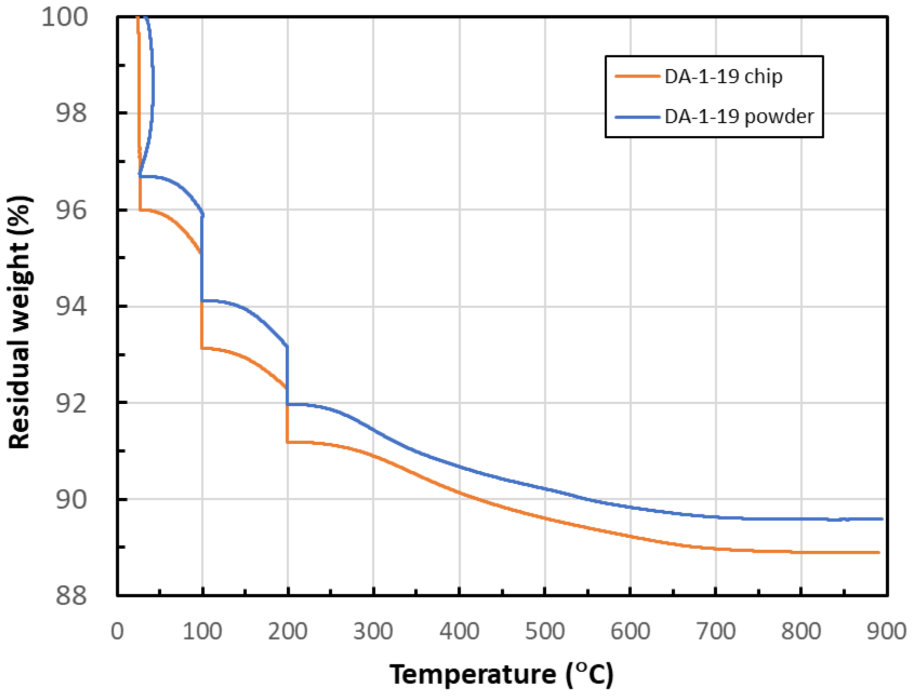

Figure 75. Residual weight (%) versus temperature during TGA for sample DA-1-19 (VNT-7) in chip (70.6 mg) and powder (25 mg) forms.

Table 9. Residual wight percent considered as water loss at different temperatures during TGA.

Sample ID	Lith. Unit	27°C	100°C	*27–100°C*	200°C	*100–200°C*	900°C	*200–900°C*
GI-2-6	VNT-1	2.2%	4.3%	2.1%	6.5%	2.3%	8.9%	2.4%
GI-3-2	VNT-2	3.4%	5.2%	1.8%	6.7%	1.5%	9.1%	2.4%
GI-4-8	VNT-2	2.9%	5.9%	3.0%	8.0%	2.1%	10.7%	2.7%
GI-4-18	VNT-3	2.4%	4.7%	2.3%	6.9%	2.3%	9.2%	2.3%
GI-4-35	VNT-3	3.1%	4.1%	1.0%	6.4%	2.3%	8.5%	2.1%
GI-3-52	VNT-4	3.8%	6.6%	2.8%	9.0%	2.4%	11.8%	2.8%
GI-4-49	VNT-4	3.1%	5.6%	2.5%	7.5%	1.9%	9.7%	2.2%
GI-4-54	VNT-4	3.6%	6.0%	2.4%	7.9%	1.9%	10.7%	2.8%
GI-2-65	VNT-5	3.5%	6.8%	3.3%	9.3%	2.5%	12.3%	3.0%
DA-1-17	VNT-6	1.9%	3.3%	1.4%	5.1%	1.8%	7.3%	2.2%
DA-1-19	VNT-7	3.3%	5.9%	2.7%	8.0%	2.1%	10.5%	2.5%
DA-1-19 chip	VNT-7	4.0%	6.8%	2.8%	8.8%	2.0%	11.0%	2.2%
DA-1-25	VNT-8	3.0%	3.3%	0.3%	7.3%	4.0%	9.4%	2.2%
DA-1-35	VNT-9	1.8%	3.2%	1.4%	4.2%	1.0%	5.9%	1.7%
DA-1-36	VNT-10	3.8%	5.1%	1.3%	5.8%	0.7%	8.0%	2.2%
AC-1-65	UZNT	2.6%	4.5%	1.9%	6.1%	1.6%	7.8%	1.7%
AC-1-71	UZNT	2.1%	3.4%	1.3%	4.5%	1.1%	6.1%	1.6%
AC-1-111	UZNT	2.6%	5.2%	2.6%	6.8%	1.6%	8.5%	1.8%

Note: Lith. = Lithologic; cumulative change is presented in this table except for temperature ranges at 100, 200 and 900°C

As TGA is suited for small, powdered samples, note that the current approaches will not inform water content or water saturation in terms of the volume of water per the volume of voids of samples of a "representative elementary volume" for multiphase hydrologic modeling at the PE1 testbed for the following reasons:

- the powdered samples have disturbed pore space water content after being crushed, pulverized, and sieved, and thus in this case TGA examines water below residual saturation that is interacting with the surface of minerals or their internal structure and/or extra-framework cations;
- even if the thermogravimetric measurements can produce a measure of water content in terms of mass wetness *w* (i.e., the ratio of mass of water in a sample to the mass of solids in a

sample), small non-pulverized samples with intact pores structure probably will be below the "representative elementary volume" for these rocks and thus not large enough to be statistically relevant for continuum-scale fluid flow modeling; and

- TGA does not directly yield parameters for volumetric water content and volumetric air content and those to convert to saturations—the mass measurements alone are not sufficient for the characterization of air and water volumetric content that is important to flow and transport modeling, e.g., dry bulk density ϱ_b and the density of water ϱ_w are needed to convert mass wetness w to volumetric water content θ, *via* $\theta = w(\varrho_b/\varrho_w)$, and porosity n (ratio of the volume of voids to the total sample volume) is needed to obtain water saturation s (ratio of the volume of water to the volume of voids) and air saturation a (ratio of the volume of air to the volume of voids) via $s = \theta n$ and $a = 1 - s$.

Thermogravimetric analysis measures water-solid interactions for surface and internal structures but is not suited for the larger connected pore space filled with water and air that governs the macroscopic transport of the water and gas phases. TGA, however, would measure the state of the water in terms of the strength of interaction that may reflect processes that impact water and gas species (e.g., Xenon) sorption and/or other chemical reactions at fluid-mineral interfaces or within internal structures (i.e., clay interlayers or internal structure of clinoptilolite). The water-fluid interaction and sorption processes affecting noble gas or other tracer transport are important, and their affects could be incorporated into modeling, and thus collection of TGA is important.

3.3.3. In Situ Water Content

Water content as based on approximately fist-sized or "hand" samples preserved in the field during mining operations (see Section 2) was measured, and sub-cores of these samples were used to determine dry bulk density, grain density, porosity, and permeability (Table 1). Preserved samples may also be referred to as in situ water content samples.

Gravimetric or mass-based water content obtains the ratio of the mass of the water in the preserved sample over the mass of the dry solids in the sample, which is also called mass wetness w, where $w = M_w/M_s$ (subscripts w = water and s = solids, and M = mass). Methods from ASTM D2216–19 could be applied, but they may need to be modified to account for the water-sensitive solid phases (e.g., clinoptilolite, smectite, and opal). Methods used for this study included drying at 60°C in a convection oven with a drying a time period of over 72 hours (Table 10; Figure 60; note that future review of the TGA data of Section 3.3.2 may allow for a refined or more justified choice of drying temperature for these samples). Hand samples used in measurement of mass wetness (Table 10) were sub-cored and used to obtain dry bulk density, and mean particle or grain density via helium pyconmetry.

Volume measurements of the irregularly shaped hand samples were attempted with a water-displacement method that was evaluated and shown to be inaccurate. A Creality 3D Scanner Kit with 0.05 mm accuracy was used to obtain the volume of the irregular hand samples to allow conversion of mass wetness to volumetric water content. For validation, one sample was X-ray CT-ed with the Zeiss Xradia 620 Versa instrument (see Section 3.2.4), and the image data masked to the outer margin of the sample by marker-based watershed methods using Avizo™ 3D 2021.2 software by Thermo Fisher Scientific (Figure 61), and the label analysis module of Avizo™ was used on the binarized sample to determine the sample's volume, which for sample 12p06-1190-U-DLS-H-025-Practice-1 is 163.7 cm^3; thus, the volumetric water content of this originally preserved sample is 0.18. As a check, we use the formula $\theta = w(\varrho_b/\varrho_w)$, and assuming a water density of 1 g/cm^3, we estimate a dry bulk density of 1.7 g/cm^3, which is similar to typical values calculated by MICP (see Table 8). Confidence intervals for saturation in Table 10 were based on best estimates of measured values. Note that some samples had a non-monotonic change in weight during heating in the convection oven—change in ambient relative humidity during possible storms may explain the non-monotonic changes. The authors are considering switching to use of a heated vacuum oven for future measurements.

Table 10. Water content information of various types.

Sample ID	Lith. Unit	Wet mass (g)	Dry mass (g)	Drying time (d)	Dry Volume (cm^3)	Mass wetness w	Volume wetness θ	Saturation, mean**	Sat. 95% lower CI*	Sat. 95% upper CI*
12p06-1280-U-DLS-H-013	VNT-3	304.84	278.08	56.0	192.22	0.10	0.14	0.40	0.35	0.45
12p06-1190-U-LBP-H-004	VNT-3	237.10	215.96	9.04	144.42	0.10	0.15	0.42	0.37	0.47
12p06-1190-U-LBP-H-013	VNT-3	268.13	241.88	9.04	162.66	0.11	0.16	0.48	0.42	0.55
12p06-1280-U-DLS-H-025-Practice-1	VNT-4	301.72	272.93	8.08	163.7	0.11	0.18	Nd	nd	nd
12p06-1490-U-DLS-H-025	VNT-4	309.47	277.79	9.90	188.31	0.11	0.17	0.51	0.45	0.57
12p06-1280-U-DLS-H-022	VNT-4	211.46	183.84	9.90	119.44	0.15	0.23	0.91	0.77	1.06
12p06-1280-U-DLS-H-031	VNT-4	262.64	237.20	9.90	138.22	0.11	0.18	0.92	0.74	1.13
12p06-1280-U-DLS-H-034	VNT-5	152.61	129.76	20.2	85.85	0.18	0.27	0.89	0.77	1.03
12p06-1190-U-LBP-H-016	VNT-5	272.27	228.30	20.2	169.74	0.19	0.26	0.61	0.56	0.68
12p06-1190-U-LBP-H-025	VNT-5	411.10	334.14	20.2	249.30	0.23	0.31	0.77	0.70	0.85
U12p06-AC-1-92.5-92.9	UZNT	749.50	618.20	10.0	401.34	0.21	0.33	1.01	0.89	1.15
U12p06-AC-1-120.3-120.8	UZNT	763.82	622.60	10.0	404.96	0.23	0.35	1.22	1.06	1.41
U12p06-AC-1-151.5-152.0	UZNT	947.79	757.30	10.0	517.45	0.25	0.37	1.05	0.94	1.18

Note: Lith. = Lithologic; *CI stands for confidence interval. **Saturation uses porosity from helium pycnometry ($s = \theta/n$). nd = no data; conversion of mass of water to volume of water assumes 1.00 g/cm^3.

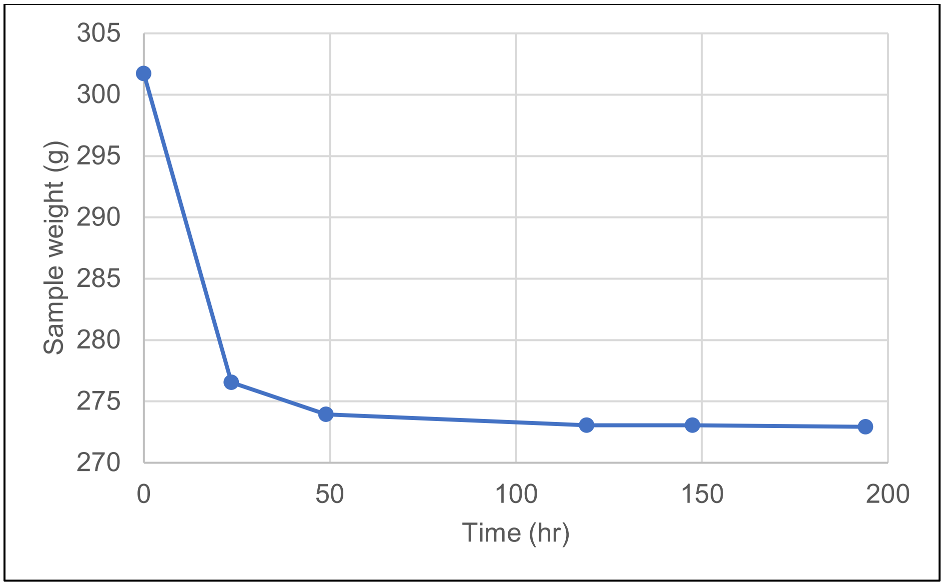

Figure 76. Sample weight versus time for drying of sample 12p06-1280-U-DLS-H-025-Practice-1 in a convection oven at 60°C.

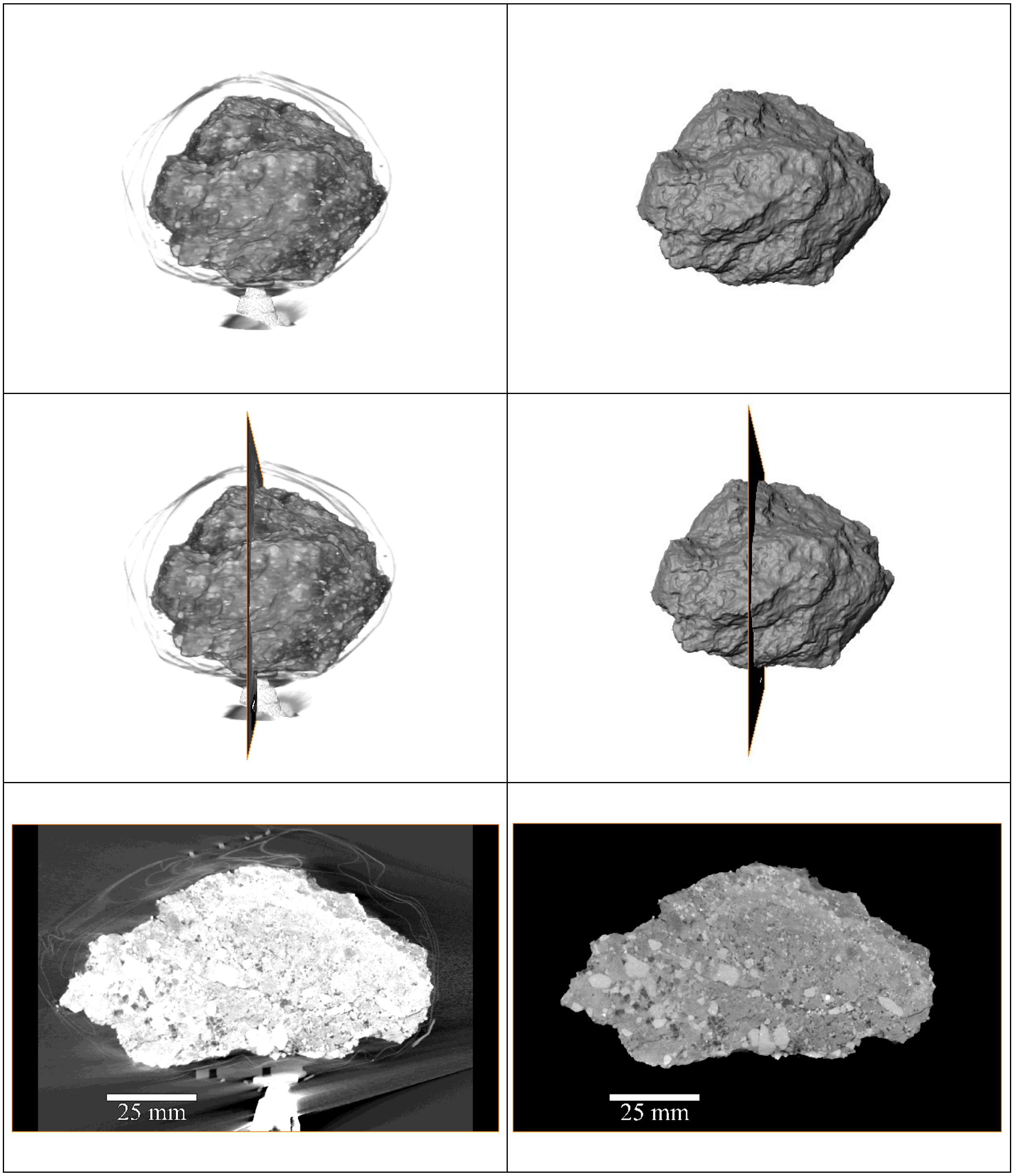

Figure 77. 3D rendering and 2D images of the "hand" sample 12p06-1280-U-DLS-H-025-Practice-1 based on X-ray CT scanning. Greyscale for the left column was adjusted to emphasize the rock sample, the plastic bag tied around the sample, and lower mount. The right column shows the same sample but after marker-based water-shed masking to only show interior of the sample, which was used to calculate the sample's total volume of 163.7 cm^3.

3.3.4. Porosity and Permeability

Porosity measurements using a helium porosimeter and methods following Jones and Associates (1985) were made on right cylindrical rock samples that were subsequently used in the permeability measurements with dimensions given in Table 11, except for one irregular friable sample that could not sub-cored for a right-circular cylinder. Nitrogen gas permeability measurements were made on the same samples as for porosity with an ultra-violet cured urethane jacket to prevent the permeant from flowing along the sample perimeter. The samples were confined under 80 psi (shop air) pressure to keep the jacket from delaminating from the sample surface. Metal porous frits were placed on each end of the sample and combined with endcaps with a center port for air flow, provided a way for gas to flow evenly across the ends of the sample. A fixed upstream gas pressure was applied, and the downstream pressure was atmospheric. The flowrate was measured along the sample downstream line and regulator with a standard flow meter calibrated for Nitrogen gas. Darcy's law was used to estimate permeability.

Table 11. Dimensions, porosity, grain density, and permeability of cylindrical plugs from water content samples.

Sample ID	Lith. Unit	Length (cm)	Diameter (cm)	Porosity (%)	Grain Density (g/cc)	Permeability
12p06-1280-U-DLS-H-013	VNT-3	4.443	2.525	35.15	2.296	7.98E-14
12p06-1190-U-LBP-H-004	VNT-3	nd	nd	35.19	2.280	nd
12p06-1190-U-LBP-H-013	VNT-3	3.000	2.532	33.47	2.294	2.71E-12
12p06-1490-U-DLS-H-025	VNT-4	4.272	2.532	33.23	2.208	7.42E-13
12p06-1280-U-DLS-H-022	VNT-4	4.643	2.532	25.49	2.201	1.15E-13
12p06-1280-U-DLS-H-031	VNT-4	4.100	2.535	20.08	2.202	2.70E-13
12p06-1280-U-DLS-H-034	VNT-5	3.719	2.520	29.79	2.236	1.98E-13
12p06-1190-U-LBP-H-016	VNT-5	2.888	2.532	42.18	2.383	1.27E-10
12p06-1190-U-LBP-H-025	VNT-5	3.3048	2.530	40.01	2.326	6.02E-11
U12p06-AC-1-92.5-92.9	UZNT	4.8545	2.538	32.33	2.342	1.99E-13
U12p06-AC-1-120.3-120.8	UZNT	4.858	2.538	28.52	2.180	3.30E-13
U12p06-AC-1-151.5-152.0	UZNT	5.0246	2.538	35.00	2.275	1.96E-13

Note: Lith. = Lithologic. For sample 12p06-1280-U-LBP-H-004: no data (nd) were collected for length, diameter, and permeability due to friability of material, and the irregular sample was used to measure mass (19.70 g), porosity via helium pycnometry, and volume via 3D scanning (13.332 cm^3); grain density was calculated using mass and volume measurements on the irregular sample; and permeability was not measured.

This page left blank

REFERENCES

Bish, D.L. 1993. Thermal behavior of natural zeolites. LA-UR93-2881, Proceedings of Zeolite '93 Conference, Los Alamos National Laboratory, 24 p.

Bodmer, M., Townsend, M., Roberts, B., Wilson, J., Reppart, J., Smith, D., Downs, N., Feldman, J., Choens, R.C., Heath, J., Holland, A., Barrow, P., Bartlett, T., Boukhalfa, H., Broome, S., Dietel, M., Downs, C., Ezzedine, S., Freimuth, C., Griego, J., Ingraham, M., Jaramillo, J., Jones, K., Kibikas, W., Kuhlman, K., Larotonda, J., Miller, A., Otto, S., Powell, M., Rodriguez, M., Tafoya, J., Valdez, N., Xu, G., 2024. LYNM PE1 Pre-Experiment A Site Characterization Report, SAND2024-07522.

Chipera, S.J., Goff, F., Goff, C.J., and Fittipaldo, M. 2006. Zeolitization of intracaldera sediments and rhyolitic rocks of Valles caldera, New Mexico, USA. In Zeolite '06—7th International Conference on the Occurrence, Properties, and Utilization of Natural Zeolites, Bowman, R.S. and Delap, S.E. (eds.), Socorro, New Mexico, USA, 16-21 July 2006.

Fawcett, T.G., J.R. Blanton, S.N. Kabekkodu, and T.N. Blanton, 2018. Mineral identification by elemental composition: a new tool within PDF-4 databases. Powder Diffraction 33(2), 156-161.

Giencke, J., 2007. Introduction to EVA. Bruker Coop. Billerica 31.

Heath, J.E., Dewers, T.A., McPherson, B.J.O.L., Nemer, M.B., Kotula, P.G. 2012. Pore-lining phases and capillary breakthrough pressure of mudstone caprocks: Sealing efficiency of geologic CO_2 storage sites. International Journal of Greenhouse Gas Control 11, 204–220.

Heath, J.E., Kuhlman, K.L., Broome, S.T., Wilson, J.E., and Malama, B. 2021. Heterogeneous multiphase flow properties of volcanic rocks and implications for noble gas transport from underground nuclear explosions. Vadose Zone Journal 20(3), e20123, https://doi.org/10.1002/vzj2.20123.

Jones, F and Associates, Inc. 1985. "Porosimeter Theory" Theory of operation of Coberly-Stevens porosimeter.

Kibikas, W.M., Wilson, J.E., Jaramillo, J.L., Broome, S.T., Bodmer, M.A., Choens, R.C., Feldman, J. Geomechanical Properties of Vitric and Zeolitic Nonwelded Tuffs from the PE1 Testbed, Journal of Volcanology and Geothermal Research (submitted).

Kotula, P.G., Keenan, M.R., 2006. Application of multivariate statistical analysis to STEM X-ray spectral images: interfacial analysis in microelectronics. Microscopy and Microanalysis 12, 538–544.

Kuhlman, K.L., F.T. Good, T. LaForce & J.E. Heath, 2022. FY22 Progress on Imbibition Testing in Containment Science, SAND2022-13014, Albuquerque, NM: Sandia National Laboratories.

Knowlton, G.D., White, T.R., and McKague, H.L. Thermal Study of Types of Water Associated with Clinoptilolite. Clays Clay Miner. 29, 403–411 (1981). https://doi.org/10.1346/CCMN.1981.0290510.

Moore, D.M, Reynolds, R.C. Jr. 1997. X-ray Diffraction and the Identification and Analysis of Clay Minerals, Second Edition. Oxford University Press, New York, 400 p.

Myers, et al., 2024. A Multi-Physics Experiment for Low-Yield Nuclear Explosion Monitoring, LLNL-TR-864107, 17p. DOI:https://doi.org/10.2172/2345984.

Rodriguez, M.A., Kotula, P.G., Griego, J.M., Heath, J.E., Bauer, S.J., and Wesolowski, D.E. 2012. Multivariate statistical analysis of micro-X-ray fluorescence spectral images. Powder Diffraction 27(2), 108–113, doi: 10.1017/S0885715612000243.

Schindelin, J., Arganda-Carreras, I., Frise, E., Kaynig, V., Longair, M., Pietzsch, T., Preibisch, S., Rueden, C., Saalfeld, S., Schmid, B., Tinevez, J., White, D.J., Hartenstein, V., Eliceiri, K., Tomancak, P., and Cardona, A. 2012. Fiji: an open-source platform for biological image analysis. Nature Methods 9(7), 676–682, doi:10.1038/nmeth.2019.

Swanson, B.F. 1981. A simple correlation between permeabilities and mercury capillary pressures. Journal of Petroleum Technology 33, 2498–2504.

Wilson, J.E., Bodmer, M.A., Townsend, M., Choens, R.C., Bartlett, T., Dietel, M., Downs, N., Reppart, J., Smith, D., Larotonda, J., Jaramillo, J. Barrow, P., Kibikas, W., Sam, R., Broome, S., Davenport, K., 2024. LYNM-PE1 Seismic Parameters from Borehole Log, Laboratory, and Tabletop Measurements, SAND2024-07529.

Yuan, H. and D.L. Bish, 2010. NEWMOD+, A New Version of the NEWMOD Program for Interpreting X-Ray Powder Diffraction Patterns from Interstratified Clay Minerals. Clays and Clay Minerals 58(3), 318-326.

DISTRIBUTION

Email—Internal

Name	Org.	Sandia Email Address
Technical Library	1911	sanddocs@sandia.gov

This page left blank

Sandia National Laboratories